Computational and Systems Biology
Physics of Living Systems

Overflow metabolism originates from growth optimization and cellheterogeneity

Reviewed Preprint
v2 • December 19, 2024
Revised by authors

Reviewed Preprint
v1 • February 7, 2024

Xin Wang

School of Physics, Sun Yat-sen University, Guangzhou, China

eLife Assessment

This **valuable** study tackles the well-established overflow metabolism issue by applying a coarse-grained metabolic flux model to predict how individual cells execute various energy strategies, such as respiration versus fermentation. The model's population average is **convincing** enough to align with experimental observations on overflow metabolism. However, the theoretical framework's reliance on single-cell growth rate variability must be questioned because of insufficient correlation with fluxes and the absence of regulatory mechanisms, highlighting the need for single-cell experimental validation to substantiate the proposed model.

https://doi.org/10.7554/eLife.94586.2.sa3

Abstract

A classic problem in metabolism is that fast-proliferating cells use seemingly wasteful fermentation for energy biogenesis in the presence of sufficient oxygen. This counterintuitive phenomenon, known as overflow metabolism or the Warburg effect, is universal across various organisms. Despite extensive research, its origin and function remain unclear. Here, we show that overflow metabolism can be understood through growth optimization combined with cell heterogeneity. A model of optimal protein allocation, coupled with heterogeneity in enzyme catalytic rates among cells, quantitatively explains why and how cells choose between respiration and fermentation under different nutrient conditions. Our model quantitatively illustrates the growth rate dependence of fermentation flux and enzyme allocation under various perturbations and is fully validated by experimental results in *Escherichia coli*. Our work provides a quantitative explanation for the Crabtree effect in yeast and the Warburg effect in cancer cells and can be broadly used to address heterogeneity-related challenges in metabolism.

Introduction

A prominent feature of cancer metabolism is that tumor cells excrete large quantities of fermentation products in the presence of sufficient oxygen (Hanahan and Weinberg, 2011; Liberti and Locasale, 2016; Vander Heiden et al., 2009). This process, discovered by Otto Warburg in the 1920s (Warburg et al., 1924) and known as the Warburg effect, aerobic glycolysis, or overflow metabolism (Basan et al., 2015; Hanahan and Weinberg, 2011; Liberti and Locasale, 2016; Vander Heiden et al., 2009), is ubiquitous among fast-proliferating cells across a broad spectrum of organisms (Vander Heiden et al., 2009), ranging from bacteria (Basan et al., 2015; Holms, 1996; Meyer et al., 1984; Nanchen et al., 2006; Neidhardt et al., 1990) and fungi (De Deken, 1966) to mammalian cells (Hanahan and Weinberg, 2011; Liberti and Locasale, 2016; Vander Heiden et al., 2009). For microbes, cells use standard respiration when nutrients are scarce, while they use the counterintuitive aerobic glycolysis when nutrients are adequate, just analogous to normal tissues and cancer cells, respectively (Vander Heiden et al., 2009).

Over the past century, and particularly through extensive studies in the last two decades (Liberti and Locasale, 2016), various rationales for overflow metabolism have been proposed (Basan et al., 2015; Chen and Nielsen, 2019; Majewski and Domach, 1990; Molenaar et al., 2009; Niebel et al., 2019; Peebo et al., 2015; Pfeiffer et al., 2001; Shlomi et al., 2011; Vander Heiden et al., 2009; Varma and Palsson, 1994; Vazquez et al., 2010; Vazquez and Oltvai, 2016; Zhuang et al., 2011). Notably, Basan *et al.* (Basan et al., 2015) provided a systematic characterization of this process, including various types of experimental perturbations. Currently, prevalent explanations (Basan et al., 2015; Chen and Nielsen, 2019) hold that overflow metabolism arises from the proteome efficiency in fermentation being consistently higher than that in respiration. However, recent studies have shown that the measured proteome efficiency in respiration is actually higher than in fermentation for many yeast and cancer cells (Shen et al., 2024), even though these cells generate fermentation products through aerobic glycolysis. This finding (Shen et al., 2024) apparently contradicts the prevalent explanations (Basan et al., 2015; Chen and Nielsen, 2019). Furthermore, most explanations (Basan et al., 2015; Chen and Nielsen, 2019; Majewski and Domach, 1990; Niebel et al., 2019; Shlomi et al., 2011; Varma and Palsson, 1994; Vazquez et al., 2010; Vazquez and Oltvai, 2016; Zhuang et al., 2011) heavily rely on the assumption that cells optimize their growth rate for a given rate of carbon influx (i.e., nutrient uptake rate) under each nutrient condition (or its equivalents). However, this assumption is questionable, as the given factors in a nutrient condition are the identities and concentrations of the carbon sources (Molenaar et al., 2009; Scott et al., 2010; Wang et al., 2019), rather than the carbon influx. Therefore, the origin and function of overflow metabolism still remain unclear (DeBerardinis and Chandel, 2020; Hanahan and Weinberg, 2011; Liberti and Locasale, 2016; Vander Heiden et al., 2009).

Why have microbes and cancer cells evolved to possess the seemingly wasteful strategy of aerobic glycolysis? For unicellular organisms, there is evolutionary pressure (Vander Heiden et al., 2009) to optimize cellular resources for rapid growth (Dekel and Alon, 2005; Edwards et al., 2001; Hui et al., 2015; Li et al., 2018; Scott et al., 2010; Towbin et al., 2017; Wang et al., 2019; You et al., 2013). In particular, it has been shown that cells allocate protein resources for optimal growth (Hui et al., 2015; Scott et al., 2010; Wang et al., 2019; You et al., 2013), and the most efficient protein allocation corresponds to elementary flux mode (Müller et al., 2014; Wortel et al., 2014). For cancer cells, disrupting the growth control system and evading immune destruction from the host are prominent hallmarks of their survival (Hanahan and Weinberg, 2011), which in certain ways mimic the evolutionary pressure on microbes to optimize cell growth rate. In this study, we apply the optimal growth principle of microbes, which also roughly holds for cancer cells, to a heterogeneous framework to address the puzzle of aerobic glycolysis.

We use *Escherichia coli* as a typical example to show that overflow metabolism can be understood from optimal protein allocation combined with heterogeneity in enzyme catalytic rates. The optimal growth strategy varies between respiration and fermentation depending on the concentration and type of the nutrient, and the combination with cell heterogeneity results in the standard picture (Basan et al., 2015; Holms, 1996; Meyer et al., 1984; Nanchen et al., 2006; van Hoek et al., 1998) of overflow metabolism. Our model quantitatively illustrates the growth rate dependence of fermentation/respiration flux and enzyme allocation under various types of perturbations in *E. coli*. Furthermore, it provides a quantitative explanation for the data on the Crabtree effect in yeast and the Warburg effect in cancer cells (Bartman et al., 2023; Shen et al., 2024).

Results

Coarse-grained model

Based on the topology of the metabolic network (Neidhardt et al., 1990; Nelson et al., 2008) (see **Fig. 1A**), we classify the carbon sources that enter from the upper part of glycolysis into Group A (Wang et al., 2019) and the precursors of biomass components (such as amino acids) into five pools. Specifically, each pool is designated according to its entry point (see **Fig. 1A** and **Appendix 1.2** for details): a1 (entry point: G6P/F6P), a2 (entry point: GA3P/3PG/PEP), b (entry point: pyruvate/acetyl-CoA), c (entry point: a-ketoglutarate), and d (entry point: oxaloacetate). Pools al and a2 are also combined as Pool a due to the joint synthesis of precursors. Then, the metabolic network for Group A carbon source utilization (see **Fig. 1A**) can be coarse-grained into a model shown in **Fig. 1B** (see **Appendix 2.1** for details), where node A represents an arbitrary carbon source of Group A. Evidently, **Fig. 1B** is topologically identical to **Fig. 1A**. Each coarse-grained arrow in **Fig. 1B** represents a stoichiometric flux J_i, which delivers carbon flux and may be accompanied by energy consumption or biogenesis (e.g., J_1, J_{a1}, see **Figs. 1A-B** and **Appendix-fig. 1A**).

In fact, the stoichiometric flux J_i scales with the cell population. For comparison with experiments, we define the normalized flux $J_i^{(N)} = J_i \cdot m_0 / M_{carbon}$, which can be regarded as the flux per unit of biomass (the superscript "(N)" stands for normalized; see **Appendix 1.3**–**1.4** for details). Here, M_{carbon} represents the carbon mass of the cell population, and m_0 is the weighted average carbon mass of metabolite molecules at the entry of precursor pools (see Eq. **S17**). Then, the cell growth rate λ can be represented by the total outflow of the normalized fluxes: $\lambda = \sum_i^{a1,a2,b,c,d} J_i^{(\mathrm{N})}$ (see **Appendix 1.4**). The normalized fluxes of respiration and fermentation are $J_r^{(N)} = J_4^{(N)}$ and $J_f^{(N)} = J_6^{(N)}$, respectively (see **Fig. 1A-B**). In practice, each $J_i^{(N)}$ is characterized by two quantities: the proteomic mass fraction φ_i of the enzyme dedicated to carrying the flux and the substrate quality κ_i, such that $J_i^{(N)} = \phi_i \cdot \kappa_i$. We take the Michaelis-Menten form for the enzyme kinetics (Nelson et al., 2008), and then $\kappa_i \equiv k_i \cdot \frac{[S_i]}{[S_i]+K_i}$ (see Eq. S12 and Appendix 1.4 for details), where $[S_i]$ is the concentration of substrate S_i, and K_i is the Michaelis constant. For each intermediate node and reaction along the pathway (e.g., node M_1 in J_{a1}), the substrate quality κ_i can be approximated as a constant (see Appendix 1.5): $\kappa_i \equiv k_i \cdot \frac{[S_i]}{[S_i]+K_i} \approx k_i$, where $[S_i] \geq K_i$ generally holds true in bacteria (Bennett et al., 2009; Park et al., 2016). However, the nutrient quality κ_A is a variable that depends on the nutrient type and concentration of a Group A carbon source (see Eq. S27).

Generally, there are three independent fates for a Group A carbon source in the metabolic network (Chen and Nielsen, 2019): fermentation, respiration, and biomass generation (see **Appendix-fig. 1C-E**). Each draws a distinct proteome fraction of φ_f, φ_r and φ_{BM}, with no overlap between them (see **Appendix 2.1**). The net effect of the first two fates is energy biogenesis, while

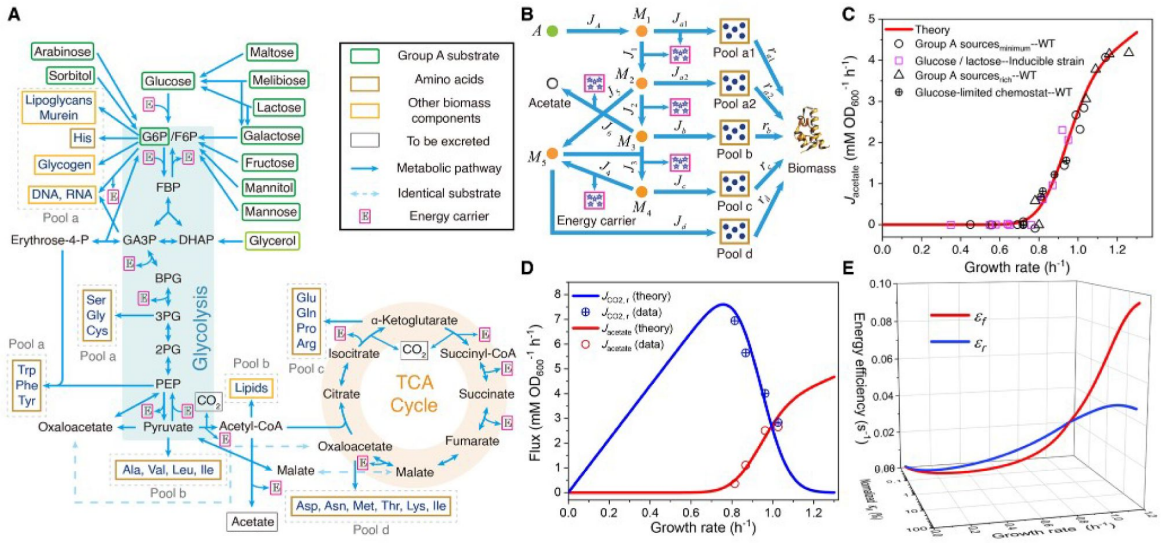

Fig. 1

Model and results of overflow metabolism in *E. coli*.

(A) The central metabolic network of carbon source utilization. The Group A carbon sources (Wang et al., 2019) are labeled with green squares. (**B**) Coarse-grained model for Group A carbon source utilization. (**C**) Model predictions (see Eqs. S47 and S160) and experimental results (Basan et al., 2015; Holms, 1996) of overflow metabolism, covering the data for all the Group A carbon sources shown in (**A**). (**D**) Growth rate dependence of respiration and fermentation fluxes (see Eqs. S47 and S160). (**E**) The proteome efficiencies for energy biogenesis in the respiration and fermentation pathways vary with growth rate as functions of the substrate quality of a Group A carbon source (see Eqs. S31 and S36). See Appendices 8 and 10 for model parameter settings and experimental data sources (Basan et al., 2015; Holms, 1996; Hui et al., 2015) for **Figs. 1**–**4** of *E. coli*.

the last one generates precursors for biomass, accompanied by energy biogenesis. By applying the proteomic constraint (Scott et al., 2010) that there is a maximum fraction $\varphi_{\max}$ for proteome allocation ($\varphi_{\max} \approx 0.48$ (Scott et al., 2010)), we have:

$$\phi_f + \phi_r + \phi_{\mathrm{BM}} = \phi_{\max}\,. \tag{1}$$

In fact, Eq. 1 is equivalent to $\phi_{\mathrm{R}} + \phi_A + \sum_{j=1}^{6}\phi_j + \sum_{l}^{a1,a2,b,c,d}\phi_l = \phi_{\max}$ (see Appendix 2.1 for derivation details), where φ_{R} and φ_A represent the proteomic mass fractions of the active ribosome-affiliated proteins and the cargo proteins responsible for the uptake of the Group A carbon source, respectively. During cell proliferation, ribosomes serve as the factories for protein synthesis and are primarily composed of proteins (Neidhardt et al., 1990; Nelson et al., 2008), while other biomass components, such as RNA, are optimally produced (Kostinski and Reuveni, 2020) in accordance with the growth rate determined by protein synthesis. Thus, the cell growth rate is proportional to φ_{R}: $\lambda = \varphi_R \circ \kappa_t$, where κ_t is a parameter set by the translation rate (Scott et al., 2010) (see Appendix 1.1 for details), which can be approximated as a constant within the growth rate range of interest (Dai et al., 2016).

For balanced cell growth in bacteria, the energy demand J_{E}, expressed as the stoichiometric energy flux in ATP, is generally proportional to the biomass production rate (Ebenhoh et al., 2024), since the proportion of maintenance energy is roughly negligible (Locasale and Cantley, 2010) (see Appendix 9 for the cases of yeast and tumor cells). Thus, the normalized flux of energy demand in ATP, denoted as $J_{\mathrm{E}}^{(\mathrm{N})}$, representing the energy demand per unit of biomass, is proportional to the growth rate λ (see Appendix 2.1 for details):

$$J_{\mathrm{E}}^{(\mathrm{N})} = \eta_{\mathrm{E}} \cdot \lambda\,, \tag{2}$$

where η_{E} is an energy coefficient (see Eqs. S25–S26 for details). By converting all energy currencies (such as NADH, FADH2, etc.) into ATP, the normalized energy fluxes for respiration and fermentation are given by $J_r^{(\mathrm{E})} = \beta_r^{(A)} \cdot J_r^{(\mathrm{N})}/2$ and $J_f^{(\mathrm{E})} = \beta_f^{(A)} \cdot J_f^{(\mathrm{N})}/2$, where $\beta_r^{(A)}$ and $\beta_f^{(A)}$ are the stoichiometric coefficients of ATP production per glucose in each pathway (see **Appendixfig. 1C-E** and **Appendix 2.1** for details). The denominator coefficient of "2" is derived from the stoichiometry of the coarse-grained reaction $M_1 \to 2M_2$ (see **Fig. 1A-B**). Applying the criteria of flux balance (i.e., mass conservation; see **Appendix 1.3**) at each intermediate node (M_i, i = 1, ..., 5) and precursor pool (Pool i, i = a1, a2, b, c, d), along with the constraints of proteome allocation (see Eq. **1**) and energy demand (see Eq. **2**), we obtain the relations between normalized energy fluxes and growth rate for a given nutrient condition with a fixed κ_A (see **Appendix 2.1** for details):

$$\begin{cases} J_r^{(\mathrm{E})} + J_f^{(\mathrm{E})} = \varphi \cdot \lambda, \\ \dfrac{J_r^{(\mathrm{E})}}{\varepsilon_r} + \dfrac{J_f^{(\mathrm{E})}}{\varepsilon_f} = \phi_{\max} - \psi \cdot \lambda, \end{cases} \tag{3}$$

where ϕ is a constant coefficient primarily determined by η_{E} (see Eq. **S33**), and $\phi \cdot \lambda$ represents the normalized flux of energy demand, excluding the energy biogenesis from the biomass synthesis pathway. The coefficients ψ, ψ_r and ψ_f are functions of $\kappa_A \cdot \psi^{-1}$ denotes the proteome efficiency for biomass generation in the biomass synthesis pathway (see Eq. **S32**), defined as ψ^{-1}

= $\lambda/\varphi_{\mathrm{BM}}$ (see **Appendix 2.1**). ψ_r and ψ_f represent the proteome efficiencies for energy biogenesis in the respiration and fermentation pathways, respectively, defined as the normalized energy fluxes expressed in ATP generated per proteomic mass fraction, with $\varepsilon_r = J_r^{(\mathrm{E})}/\phi_r$ and $\varepsilon_f = J_f^{(\mathrm{E})}/\phi_f$. Hence,

$$\begin{cases} \varepsilon_r = \dfrac{\beta_r^{(A)}}{1/\kappa_A + 1/\kappa_r^{(A)}}, \\ \varepsilon_f = \dfrac{\beta_f^{(A)}}{1/\kappa_A + 1/\kappa_f^{(A)}}, \end{cases} \tag{4}$$

where both $\kappa_r^{(A)}$ and $\kappa_f^{(A)}$ are composite parameters that can be approximated as constants, with $1/\kappa_r^{(A)}$ = $1/\kappa_1 + 2/\kappa_2 + 2/\kappa_3 + 2/\kappa_4$ and $1/\kappa_f^{(A)}$ = $1/\kappa_1 + 2/\kappa_2 + 2/\kappa_6$ (see **Appendices 1.5** and **2.1** for details).

Origin of overflow metabolism

The standard picture of overflow metabolism (Basan et al., 2015; Holms, 1996; Meyer et al., 1984; Nanchen et al., 2006; van Hoek et al., 1998) is exemplified by the experimental data (Basan et al., 2015) presented in **Fig. 1C**, where the fermentation flux exhibits a threshold-analog dependence on the growth rate λ. It is well established that respiration is significantly more efficient than fermentation in terms of energy biogenesis per unit of carbon (i.e., $\beta_r^{(A)} > \beta_f^{(A)}$) (Nelson et al., 2008; Vander Heiden et al., 2009). Then, why do cells bother to use the seemingly wasteful fermentation pathway? We proceed to address this issue by applying optimal protein allocation (Scott et al., 2010; Wang et al., 2019) within the framework of optimal growth.

For cell proliferation in a given nutrient condition (i.e., with a fixed κ_A), the values of ε_r, ε_f and ψ are determined (Eqs. 4 and S32). However, the growth rate λ can be influenced by protein allocation between respiration and fermentation, specifically λ_r and λ_f, according to the governing equation (Eq. 3). If $\varepsilon_r > \varepsilon_f$, that is, if the proteome efficiency in respiration is higher than that in fermentation, then $\lambda = \frac{\phi_{\max} - J_f^{(\mathrm{E})}\left(1/\varepsilon_f - 1/\varepsilon_r\right)}{\psi + \varphi/\varepsilon_r} \le \frac{\phi_{\max}}{\psi + \varphi/\varepsilon_r}$. The optimal growth strategy is $\phi_f = J_f^{(\mathrm{E})} = 0$, meaning that the cell exclusively uses respiration. Conversely, if $\varepsilon_f > \varepsilon_r$, then $\phi_r = J_r^{(\mathrm{E})} = 0$ is optimal, and the cell solely uses fermentation. In either case, the choice between respiration and fermentation for optimal growth is determined by weighing the proteome efficiencies.

In practice, both proteome efficiencies ε_r and ε_f are functions of nutrient quality κ_A, which can be influenced by the nutrient type and concentration of the carbon source (see Eqs. 4 and S27). Therefore, the choice for optimal growth may vary depending on the nutrient conditions. In nutrient-poor conditions where $\kappa_A \ll \kappa_r^{(A)}$ and $\kappa_A \ll \kappa_f^{(A)}$, the proteome efficiencies can be approximated by $\varepsilon_r \approx \beta_r^{(A)} \cdot \kappa_A$ and $\varepsilon_f \approx \beta_f^{(A)} \cdot \kappa_A$ (see Eq. 4), and hence $\varepsilon_r(\kappa_A) > \varepsilon_f(\kappa_A)$ (since $\beta_r^{(A)} > \beta_f^{(A)}$), meaning that the proteome efficiency of respiration is higher than that of fermentation under nutrient-poor conditions. In rich media, however, using the parameters of κ_i derived from in vivo/in vitro experimental data of *E. coli* (see **Appendix-tables 1**–**2** and **Appendix 6.1**–**6.2**), we obtain $\varepsilon_r(\kappa_{\mathrm{glucose}}^{(\mathrm{ST})}) < \varepsilon_f(\kappa_{\mathrm{glucose}}^{(\mathrm{ST})})$ with Eq. **4** (see also Eqs. **S39**–**S40**), where $\kappa_{\mathrm{glucose}}^{(\mathrm{ST})}$ represents the substrate quality of glucose at saturated concentration (abbreviated as "ST" in the superscript).

This means that the proteome efficiency in fermentation is higher than that in respiration for bacteria in rich media. Indeed, recent studies have validated that the measured proteome efficiency in fermentation is higher than in respiration for *E. coli* in lactose at saturated concentration (Basan et al., 2015), i.e., $\varepsilon_r(\kappa_{\mathrm{lactose}}^{(\mathrm{ST})}) < \varepsilon_f(\kappa_{\mathrm{lactose}}^{(\mathrm{ST})})$. In **Fig. 1E**, we present the growth rate dependence of proteome efficiencies ε_r and ε_f in a three-dimensional (3D) form using the collected data shown in **Appendix-table 1**, where ε_r, ε_f and the growth rate λ all vary as functions of nutrient quality κ_A. Furthermore, the ratio Δ (defined as $\Delta(\kappa_A) \equiv \varepsilon_f(\kappa_A)/\varepsilon_r(\kappa_A)$) is a monotonically increasing function of κ_A, and there exists a critical value of κ_A (denoted as $\kappa_A^{(C)}$; see **Appendix 2.2**

for details) satisfying $\Delta(\kappa_A^{(C)})=1$. Below $\kappa_A^{(C)}$, the cell grows slowly, and the choice for optimal growth is respiration (with $\varepsilon_f < \varepsilon_r$, $\lambda = \varphi_{\max} \cdot (\psi + \phi/\varepsilon_r)^{-1}$), while above $\kappa_A^{(C)}$, the cell grows faster, and the optimal growth strategy is fermentation (with $\varepsilon_f < \varepsilon_r$, $\lambda = \varphi_{\max} \cdot (\psi + \phi/\varepsilon_f)^{-1}$)). The above analysis qualitatively explains the phenomenon of aerobic glycolysis.

For a quantitative understanding of overflow metabolism, let us first consider the homogeneous case, where all cells share identical biochemical parameters. For optimal protein allocation, the relation between fermentation flux and growth rate is given by $J_f^{(E)}=\varphi\cdot\lambda\cdot\theta(\lambda-\lambda_C)$, where "$Q$" represents the Heaviside step function, and λ_C is the critical growth rate for a nutrient condition with $\kappa_A^{(C)}$ (i.e., $\lambda_C \equiv \lambda(\kappa_A^{(C)})$). Similarly, the growth rate dependence of respiration flux is $J_r^{(E)}=\varphi\cdot\lambda\cdot[1-\theta(\lambda-\lambda_C)]$. These digital response outcomes are consistent with the numerical simulation findings of Molenaar *et al.* (Molenaar et al., 2009). However, they are clearly incompatible with the threshold-analog response observed in the standard picture of overflow metabolism (Basan et al., 2015; Holms, 1996; Meyer et al., 1984; Nanchen et al., 2006; van Hoek et al., 1998).

To address this issue, we take into account cell heterogeneity, which is ubiquitous in both microbes (Ackermann, 2015; Bagamery et al., 2020; Balaban et al., 2004; Nikolic et al., 2013; Solopova et al., 2014; Wallden et al., 2016; Yaginuma et al., 2014; Zhang et al., 2018) and tumor cells (Duraj et al., 2021; Hanahan and Weinberg, 2011; Hensley et al., 2016). In the context of the Warburg effect or overflow metabolism, experimental studies have reported significant metabolic heterogeneity in the choice between respiration and fermentation within a cell population (Bagamery et al., 2020; Duraj et al., 2021; Hensley et al., 2016; Nikolic et al., 2013). Motivated by the observation that the turnover number (k_{cat} value) of a catalytic enzyme varies considerably between in vitro and in vivo measurements (Davidi et al., 2016; Garcia-Contreras et al., 2012), we note that the concentrations of potassium and phosphate, which vary from cell to cell, have a significant impact on the k_{cat} values of metabolic enzymes (Garcia-Contreras et al., 2012). Therefore, within a cell population, there is a distribution of k_{cat} values for a catalytic enzyme, commonly referred to as extrinsic noise (Elowitz et al., 2002). For simplicity, we assume that the k_{cat} values for each enzyme follow a Gaussian distribution. This leads to varied distributions of single-cell growth rate in different carbon sources (see Eqs. S155–S157, S163–S165), which has been fully verified by recent experiments using isogenic *E. coli* at single-cell resolution (Wallden et al., 2016) (**Appendix-fig. 2B**). Consequently, the critical growth rate λ_C should follow a Gaussian distribution $\mathcal{N}(\mu_{\lambda_C},\sigma_{\lambda_C}^2)$ within a cell population (see **Appendix 7** for details), where $\mu_{\lambda C}$ is approximated by the deterministic result of λ_C (Eq. **S43**). We assume that the coefficient of variation (CV) is $\sigma_{\lambda C}/\mu_{\lambda C}$ = 12%, or equivalently, the CV for the catalytic rate of each metabolic enzyme is 25%. Thus, we obtain the growth rate dependence of fermentation and respiration fluxes (see **Appendix 2.3** for details):

$$\begin{cases} J_f^{(\mathrm{N})}(\lambda)=\dfrac{\varphi\cdot\lambda}{\beta_f^{(A)}}\cdot\left[\operatorname{erf}\left(\dfrac{\lambda-\mu_{\lambda_C}}{\sqrt{2}\sigma_{\lambda_C}}\right)+1\right], \\ J_r^{(\mathrm{N})}(\lambda)=\dfrac{\varphi\cdot\lambda}{\beta_r^{(A)}}\cdot\left[1-\operatorname{erf}\left(\dfrac{\lambda-\mu_{\lambda_C}}{\sqrt{2}\sigma_{\lambda_C}}\right)\right], \end{cases} \tag{5}$$

where "erf" represents the error function. The fermentation flux exhibits a threshold-analog relation with the growth rate (the red curves in **Figs. 1C-D**, **2B-C**, and **3B, D, F**), while the respiration flux (the blue curve in **Fig. 1D**) decreases with an increase in fermentation flux. In **Fig. 1C-D**, we observe that the model results (see Eq. **5** and **Appendix 8**; parameters are set based on the experimental data shown in **Appendix-table S1**) quantitatively agree with the experimental data from *E. coli* (Basan et al., 2015; Holms, 1996). The fermentation flux was

determined by the acetate secretion rate $J_{acetate}^{(M)} = 2J_f^{(N)}$, and the respiration flux was deduced from the carbon dioxide flux $J_{CO_2,r}^{(M)} = 6J_r^{(N)}$ (the superscript "(M)" represents the measurable flux in the unit of mM/OD600/h; see Appendix 8.1 for details). Therefore, by incorporating cell heterogeneity, our model of optimal protein allocation quantitatively explains overflow metabolism.

Testing the model through perturbations

To further test our model, we systematically investigate its predictions under various types of perturbations and compare them with experimental data from existing studies (Basan et al., 2015; Holms, 1996) (see Appendices 3 and 4.1 for details).

First, we consider the proteomic perturbation caused by overexpression of useless proteins encoded by the *lacZ* gene (i.e., φ_Z perturbation) in *E. coli*. The net effect of the φ_Z perturbation is that the maximum fraction of the proteome available for resource allocation changes from φ_{max} to $\varphi_{max} - \varphi_Z$ (Basan et al., 2015), where φ_Z is the proteomic mass fraction of useless proteins. In a cell population, the critical growth rate λ_C (φ_Z) still follows a Gaussian distribution N ($\mu_{\lambda C}$ (φ_Z), $\sigma_{\lambda C}$ (φ_Z)^2), where the CV of λ_C (φ_Z) remains unchanged. Consequently, the growth rate dependence of fermentation flux changes to $J_f^{(N)} = \frac{\varphi \cdot \lambda}{\beta_f^{(A)}} \cdot \left[\mathrm{erf}\left(\frac{\lambda - \mu_{\lambda_C}(\phi_Z)}{\sqrt{2}\sigma_{\lambda_C}(\phi_Z)} \right) + 1 \right]$ (see Appendix 3 for model perturbation results regarding respiration flux), where both the growth rate $\lambda(\kappa_A, \varphi_Z)$ and the normalized fermentation flux $J_f^{(N)}(\kappa_A, \phi_Z)$ are bivariate functions of κ_A and φ_Z (see Eqs. S49 and S56–S57). For each degree of LacZ expression (with fixed φ_Z), similar to wild-type strains, the fermentation flux exhibits a threshold-analog response to growth rate as κ_A varies (see **Fig. 2C**), which agrees quantitatively with experimental results (Basan et al., 2015). The shifts in the critical growth rate $\lambda_C(\varphi_Z)$ are fully captured by $\mu_{\lambda C}$ (φ_Z) = $\mu_{\lambda C}$ (0) (1 − φ_Z/φ_{max}). In contrast, for nutrient conditions with each fixed κ_A, since the growth rate changes with φ_Z just like λ_C (φ_Z): $\lambda(\kappa_A, \varphi_Z) = \lambda$ (κ_A, 0)(1 − φ_Z/φ_{max}), the fermentation flux is then proportional to the growth rate for the varying levels of LacZ expression: $J_f^{(N)} = \frac{\varphi}{\beta_f^{(A)}} \cdot \left[\mathrm{erf}\left(\frac{\lambda(\kappa_A, 0) - \mu_{\lambda_C}(0)}{\sqrt{2}\sigma_{\lambda_C}(0)} \right) + 1 \right] \cdot \lambda$, where the slope is a monotonically increasing function of the substrate quality κ_A. These scaling relations are well validated by the experimental data (Basan et al., 2015) shown in **Fig. 2B**. Finally, in the case where both κ_A and φ_Z are free to vary, the growth rate dependence of fermentation flux presents a threshold-analog response surface in a 3D plot, where φ_Z appears explicitly as the *y*-axis (see **Fig. 2A**). Experimental data points (Basan et al., 2015) lie right on this surface, which is highly consistent with the model predictions.

Next, we study the influence of energy dissipation, which introduces an energy dissipation coefficient w to Eq. 2: $J_E^{(N)} = \eta_E \cdot \lambda + w$. Similarly, the critical growth rate in this case, $\lambda_C(w)$, follows a Gaussian distribution $N(\mu_{\lambda C}(w), \sigma_{\lambda C}(w)^2)$ in a cell population. The relation between the growth rate and fermentation flux can be characterized by (see Appendix 3.2 for details): $J_f^{(N)} = \frac{\varphi \cdot \lambda + w}{\beta_f^{(A)}} \cdot \left[\mathrm{erf}\left(\frac{\lambda - \mu_{\lambda_C}(w)}{\sqrt{2}\sigma_{\lambda_C}(w)^2} \right) + 1 \right]$. In **Fig. 3A-B**, we present a comparison between the model results and experimental data (Basan et al., 2015) in 3D and 2D plots, which demonstrate good agreement. A notable characteristic of energy dissipation, as distinguished from φ_Z perturbation, is that the fermentation flux increases despite a decrease in the growth rate when κ_A is fixed.

We proceed to analyze the impact of translation inhibition with different sub-lethal doses of chloramphenicol on *E. coli*. This type of perturbation introduces an inhibition coefficient ι to the translation rate, thus turning κ_t into $\kappa_t/(\iota + 1)$. Still, the critical growth rate $\lambda_C(\iota)$ follows a Gaussian distribution N ($\mu_{\lambda C}(\iota)$, $\sigma_{\lambda C}(\iota)^2$), and then, the growth rate dependence of fermentation flux is is given by: $J_f^{(N)} = \frac{\varphi \cdot \lambda}{\beta_f^{(A)}} \cdot \left[\mathrm{erf}\left(\frac{\lambda - \mu_{\lambda_C}(\iota)}{\sqrt{2}\sigma_{\lambda_C}(\iota)} \right) + 1 \right]$ (see Appendix 3.3 for details). In **Appendix-fig. 2D-E**, we observe that the model predictions are generally consistent with the experimental data (Basan et

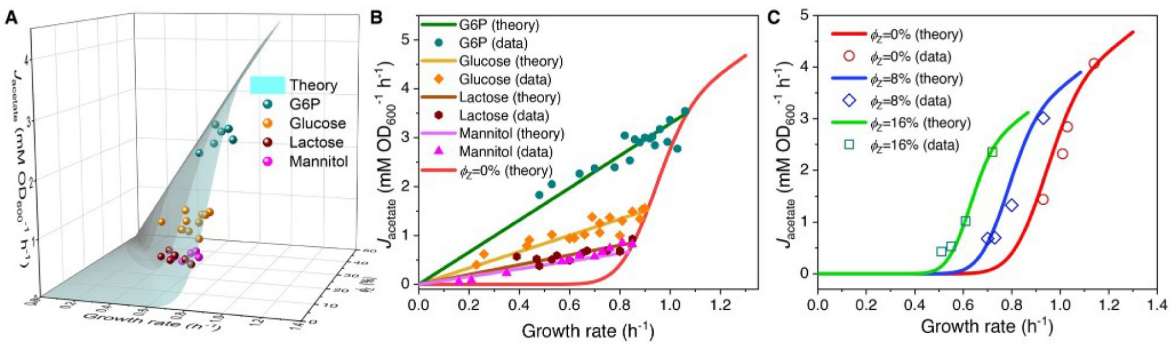

Fig. 2

Influence of protein overexpression on overflow metabolism in *E. coli*.

(A) A 3D plot of the relations among fermentation flux, growth rate, and the expression level of useless proteins. In this plot, both the acetate excretion rate and growth rate vary as bivariate functions of the nutrient quality of a Group A carbon source (denoted as κ_A) and the useless protein expression encoded by *lacZ* gene (denoted as ϕ_Z perturbation; see Eqs. S57 and S160). (**B**) Growth rate dependence of the acetate excretion rate upon ϕ_Z perturbation for each fixed nutrient condition (see Eqs. S58 and S160). (**C**) Growth rate dependence of the acetate excretion rate as κ_A varies (see Eqs. S57 and S160), with each fixed expression level of LacZ.

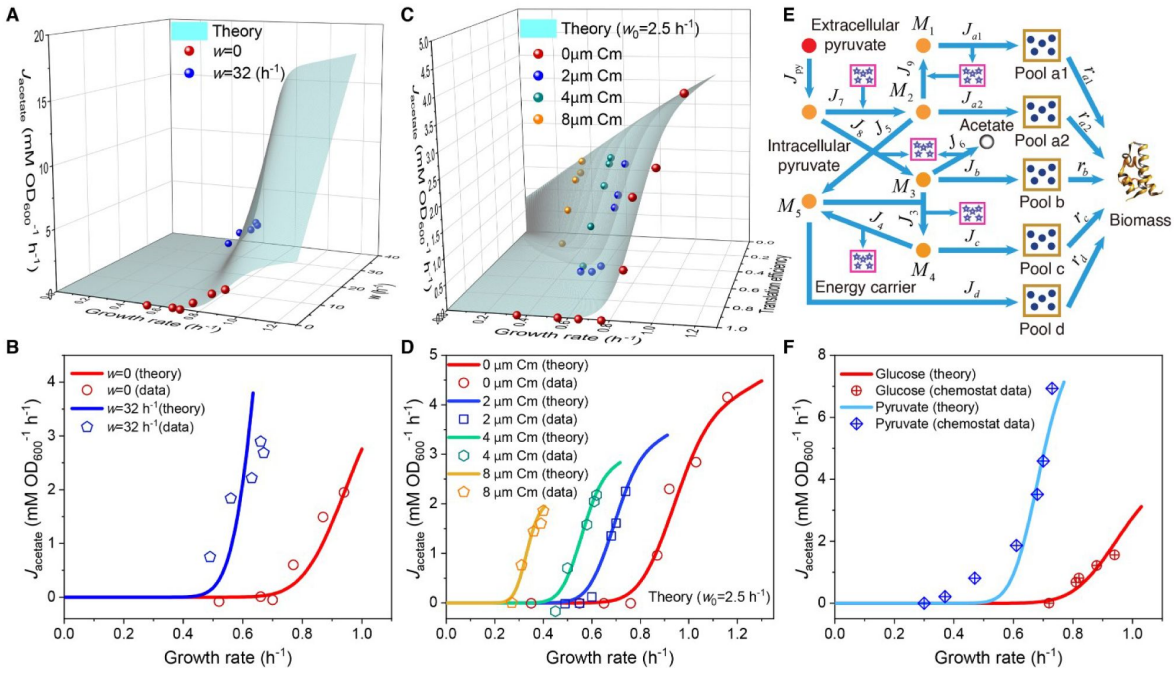

Fig. 3

Influence of energy dissipation, translation inhibition, and carbon source category alteration on overflow metabolism in *E. coli*.

(A) A 3D plot of the relations among fermentation flux, growth rate, and the energy dissipation coefficient (see Eqs. S70 and S160). (**B**) Growth rate dependence of the acetate excretion rate as the nutrient quality κ_A varies, with each fixed energy dissipation coefficient determined by or fitted from experimental data. (**C**) A 3D plot of the relations among fermentation flux, growth rate, and the translation efficiency (see Eqs. 85 and S160). Here, the translation efficiency is adjusted by the dose of chloramphenicol (Cm). (**D**) Growth rate dependence of the acetate excretion rate as κ_A varies, with each fixed dose of Cm. (**E**) Coarse-grained model for pyruvate utilization. (**F**) The growth rate dependence of fermentation flux in pyruvate (see Eqs. 105 and S160) significantly differs from that of the Group A carbon sources (see Eqs. 47 and S160).

al., 2015). However, a noticeable systematic discrepancy arises when the translation rate is low. Therefore, we consider maintenance energy, which is typically tiny and generally negligible for bacteria over the growth rate range of interest (Basan et al., 2015; Locasale and Cantley, 2010; Neidhardt, 1996). Encouragingly, by assigning a very small value to the maintenance energy coefficient w_0 (w_0 = 2.5 (h^{-1})), the model results for the growth rate-fermentation flux relation $J_f^{(N)} = \frac{\varphi \cdot \lambda + w_0}{\beta_f^{(A)}} \cdot \left[\mathrm{erf}\left(\frac{\lambda - \mu_{\lambda_C}(t)}{\sqrt{2}\sigma_{\lambda_C}(t)} \right) + 1 \right]$ quantitatively agree with experiments (Basan et al., 2015) (see **Fig. 3C-D** and **Appendix 3.3** for details).

Finally, we consider the alteration of nutrient categories by switching to a non-Group A carbon source: pyruvate, which enters the metabolic network from the endpoint of glycolysis (Neidhardt et al., 1990; Nelson et al., 2008). The coarse-grained model for pyruvate utilization is shown in **Fig. 3E** (see also **Fig. 1A**), which shares identical precursor pools with those for Group A carbon sources, yet has several differences in the coarse-grained reactions. The growth rate dependencies of both the proteome efficiencies (see **Appendix-fig. 2H**) and energy fluxes (see **Fig. 3F**) are qualitatively similar to those of Group A carbon source utilization, while there are quantitative differences in the coarse-grained parameters (see **Appendices 4.1** and **8** for details). Most notably, the critical growth rate $\lambda_C^{(py)}$ and the ATP production per glucose in the fermentation pathway $\beta_f^{(py)}$ for pyruvate utilization are noticeably smaller than those for Group A sources (i.e., λ_C and $\beta_f^{(A)}$, respectively). Consequently, the growth rate dependence of fermentation flux in pyruvate should present a distinctly different curve from that of Group A carbon sources (see Eqs. **5** and **S105**), which is fully validated by experimental results (Holms, 1996) (see **Fig. 3F**).

Enzyme allocation under perturbations

As mentioned above, our coarse-grained model is topologically identical to the central metabolic network (**Fig. 1A**) and can thus predict enzyme allocation for each gene in glycolysis and the TCA cycle (see **Appendix-fig. 1B** and **Appendix-table 1**) under various types of perturbations. In **Fig. 1B**, the intermediate nodes M_1, M_2, M_3, M_4, and M_5 represent G6P, PEP, acetyl-CoA, α-ketoglutarate, and oxaloacetate, respectively. Therefore, φ_1 and φ_2 correspond to enzymes involved in glycolysis (or at the junction of glycolysis and the TCA cycle), while φ_3 and φ_4 correspond to enzymes in the TCA cycle (see **Fig. 1A-B** and **Appendix 2.1**).

We first consider enzyme allocation under carbon limitation by varying the nutrient type and concentration of a Group A carbon source (i.e., κ_A perturbation). This has been extensively studied in more simplified models (Hui et al., 2015; You et al., 2013), where the growth rate dependence of enzyme allocation under κ_A perturbation is generally described by a C-line response (Hui et al., 2015; You et al., 2013). Specifically, the genes responsible for digesting carbon compounds exhibit a linear increase in gene expression as the growth rate decreases (Hui et al., 2015; You et al., 2013). However, when it comes to enzymes catalyzing reactions between intermediate nodes, we gathered experimental data from existing studies (Hui et al., 2015) and found that the enzymes in glycolysis exhibit a completely different response pattern compared to those in the TCA cycle (**Appendix-fig. 3A-B**). This discrepancy cannot be explained by the C-line response. To address this issue, we apply the coarse-grained model described above (see **Fig. 1B**) to calculate the growth rate dependence of enzyme allocation for each φ_i(i = 1, 2, 3, 4) using model settings for wild-type strains, with no fitting parameters influencing the shape (see Eqs. **S118**–**S119** and **Appendix 8**). In **Fig. 4A-B** and **Appendix-fig. 3C-D**, we see that the model predictions overall match with the experimental data (Hui et al., 2015) for representative genes from either glycolysis or the TCA cycle, and maintenance energy (with w_0 = 2.5 (h^{-1})) has a negligible effect on this process. Still, there are minor discrepancies that arise from the basal expression of metabolic genes, which may be attributed to the fact that our model deals with relatively stable growth conditions while microbes need to be prepared for fluctuating environments (Basan et al., 2020; Kussell and Leibler, 2005; Mori et al., 2017).

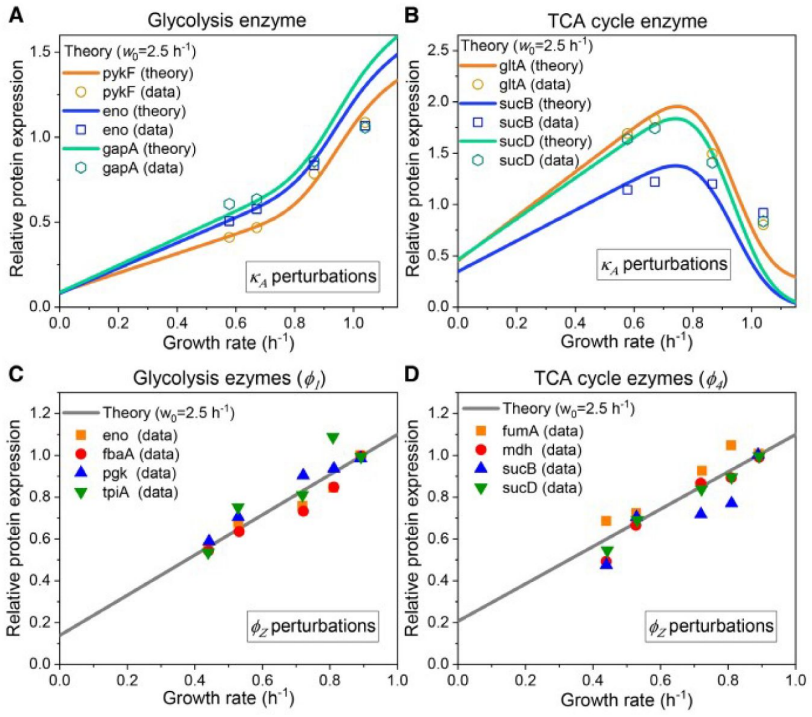

Fig. 4

Relative protein expression of central metabolic enzymes in *E. coli* under nutrient limitation and proteomic perturbation.

(A, C) Relative protein expression of representative genes from glycolysis. (**B, D**) Relative protein expression of representative genes from the TCA cycle. (**A, B**) Results of the perturbation through changes in nutrient quality κ_A (see Eq. S119). (**C, D**) Results of proteomic perturbation via varied levels of expression of the useless protein LacZ (i.e., ϕ_Z perturbation; see Eq. S121).

We proceed to analyze the influence of φ_Z perturbation and energy dissipation. In both cases, our model predicts a linear response to growth rate reduction for all genes in either glycolysis or the TCA cycle (see Appendix 5.2–5.3 for details). For φ_Z perturbation, all predicted slopes are positive, and there are no fitting parameters involved (Eqs. S120–S121). In **Fig. 4C-D** and **Appendix-fig. 3E-J**, we show that our model quantitatively illustrates the experimental data (Basan et al., 2015) for representative genes in the central metabolic network, and there is better agreement with experiments (Basan et al., 2015) by incorporating the maintenance energy (with $w_0 = 2.5$ (h^{-1}) as aforementioned). For energy dissipation, however, the predicted slopes of the enzymes corresponding to φ_4 are negative, and there is a constraint that the slope signs of the enzymes corresponding to the same $\varphi_i (i = 1, 2, 3)$ should be the same. In **Appendix-fig. 3K-N**, we see that the model results (Eqs. **S127** and **S123**) are consistent with experiments (Basan et al., 2015).

Explanation of the Crabtree effect in yeast and the Warburg effect in cancer cells

We proceed to apply our model to explain the Crabtree effect in yeast (Bagamery et al., 2020; De Deken, 1966; Shen et al., 2024) and the Warburg effect in tumors (Bartman et al., 2023; Duraj et al., 2021; Hanahan and Weinberg, 2011; Liberti and Locasale, 2016; Shen et al., 2024; Vander Heiden et al., 2009) with slight modifications using the optimal growth principle combined with cell heterogeneity (see Appendix 9 and **Appendix-fig. 5**). For yeast and tumors, similar to the case of *E. coli*, the proteome efficiencies ε_r and ε_f are both increasing functions of the nutrient quality κ_A (see Eq. **S170**). Specifically, under poor nutrient conditions (i.e., ε_A is small), the proteome efficiency in respiration is higher than that in fermentation: $\varepsilon_r > \varepsilon_f$ (see Eqs. **S174**–**S175**), making respiration the best choice for optimal growth (see Eq. **S171**). Conversely, when the nutrient is abundant and $\varepsilon_f > \varepsilon_r$, aerobic glycolysis (i.e., fermentation) becomes the optimal growth strategy (see Eq. **S172**). Further combination with cell heterogeneity results in the standard picture of overflow metabolism, which has indeed been observed in yeast (van Hoek et al., 1998). However, it remains challenging to tune the growth rate of cancer cells in vivo.

Recently, Shen et al. (Shen et al., 2024) discovered that the proteome efficiency measured at the cell population level in respiration (i.e., $\langle\varepsilon_r\rangle$; where "$\langle\ \rangle$" denotes the population average) is higher than that in fermentation (i.e., $\langle\varepsilon_f\rangle$) for many yeast and cancer cells, despite the presence of fermentation fluxes through aerobic glycolysis. Evidently, this finding (Shen et al., 2024) contradicts prevalent explanations (Basan et al., 2015; Chen and Nielsen, 2019), which hold that overflow metabolism arises because the proteome efficiency in fermentation is consistently higher than in respiration. Nevertheless, our model may resolve this puzzle due to the incorporation of two important features. First, our model predicts that the proteome efficiency in respiration is larger than that in fermentation when nutrient quality is low (see Eqs. S174–S175). Second, and crucially, by accounting for cell heterogeneity, our model allows a proportion of cells to have a higher proteome efficiency in fermentation than in respiration, even when the overall proteome efficiency in respiration at the cell population level is greater than that in fermentation (i.e., $\langle\varepsilon_r\rangle > \langle\varepsilon_f\rangle$).

To compare our model results quantitatively with experimental data on yeast and tumors (Shen et al., 2024), we define $\mathrm{Pr}_f = \frac{J_f^{(\mathrm{E})}}{J_f^{(\mathrm{E})} + J_r^{(\mathrm{E})}}$ as the fraction of ATP produced through fermentation. To account for cell heterogeneity, we apply Gaussian distributions to enzyme turnover numbers, as mentioned above. This yields the relationship between Pr_f (i.e., $\frac{J_f^{(\mathrm{E})}}{J_f^{(\mathrm{E})} + J_r^{(\mathrm{E})}}$) and $\langle \varepsilon_r \rangle$ and $\langle \varepsilon_f \rangle$ through derivations (see Eqs. S180–S190 and Appendix 9 for details):

$$\frac{J_f^{(\mathrm{E})}}{J_f^{(\mathrm{E})} + J_r^{(\mathrm{E})}} = \frac{1}{2}\left[\mathrm{erf}\left(\frac{1 - \langle \varepsilon_r \rangle / \langle \varepsilon_f \rangle}{\sqrt{2} \cdot \sqrt{\chi_{\varepsilon_r}^2 + \chi_{\varepsilon_f}^2 \cdot \left(\langle \varepsilon_r \rangle / \langle \varepsilon_f \rangle\right)^2}}\right) + 1\right], \tag{6}$$

where $\chi_{\varepsilon r}$ and $\chi_{\varepsilon f}$ represent the CVs of proteome efficiencies ε_r and ε_f, respectively. Due to the higher levels of cell heterogeneity in yeast (Bagamery et al., 2020) and cancer cells (Duraj et al., 2021; Hanahan and Weinberg, 2011; Hensley et al., 2016), the CVs of ε_r and ε_f (i.e., $\chi_{\varepsilon r}$ and $\chi_{\varepsilon f}$) in these cells are expected to be significantly higher than those in *E. coli*, although their precise values are unknown. The values for the variables shown in Eq. 6 can be obtained from experiments. Therefore, we plot the theoretical results from Eq. 6 using $\chi_{\varepsilon r}$ and $\chi_{\varepsilon f}$ values of 0.25, 0.40, and 0.58 to compare with experimental data from yeast and in vivo mouse tumors (Bartman et al., 2023; Shen et al., 2024). As shown in **Fig. 5A-B**, the theoretical results with $\chi_{\varepsilon r} = \chi_{\varepsilon f} = 0.58$ align quantitatively with the experimental data (Bartman et al., 2023; Shen et al., 2024) on both logarithmic and linear scales, demonstrating that our model has the potential to quantitatively explain the Crabtree effect in yeast and the Warburg effect in cancer cells.

Discussion

The phenomenon of overflow metabolism, or the Warburg effect, has been a long-standing puzzle in cell metabolism. Although many rationales have been proposed over the past century (Basan et al., 2015; Chen and Nielsen, 2019; Majewski and Domach, 1990; Molenaar et al., 2009; Niebel et al., 2019; Peebo et al., 2015; Pfeiffer et al., 2001; Shlomi et al., 2011; Vander Heiden et al., 2009; Varma and Palsson, 1994; Vazquez et al., 2010; Vazquez and Oltvai, 2016; Zhuang et al., 2011), contradictions persist (Shen et al., 2024), leaving the origin and function of this phenomenon unclear (DeBerardinis and Chandel, 2020; Hanahan and Weinberg, 2011; Liberti and Locasale, 2016; Vander Heiden et al., 2009). In this study, we use *E. coli* as a typical example and demonstrate that overflow metabolism can be understood through optimal protein allocation combined with cell heterogeneity. Under nutrient-poor conditions, the proteome efficiency of respiration is higher than that of fermentation (see **Fig. 1E**), and thus the cell uses respiration to optimize growth. In rich media, however, the proteome efficiency of fermentation increases more rapidly and surpasses that of respiration (see **Fig. 1E**), leading the cell to adopt fermentation as the optimal growth strategy. In further combination with cell heterogeneity in enzyme catalytic rates (Davidi et al., 2016; Garcia-Contreras et al., 2012), our model quantitatively illustrates the threshold-analog response (Basan et al., 2015; Holms, 1996) in overflow metabolism (see **Fig. 1C**). Furthermore, it quantitatively explains the data on the Crabtree effect in yeast and the Warburg effect in cancer cells (Bartman et al., 2023; Shen et al., 2024).

In existing rationales (Basan et al., 2015; Chen and Nielsen, 2019; Majewski and Domach, 1990; Shlomi et al., 2011; Varma and Palsson, 1994; Vazquez and Oltvai, 2016), the standard picture of overflow metabolism (Basan et al., 2015; Holms, 1996; Meyer et al., 1984; Nanchen et al., 2006; van Hoek et al., 1998) has primarily been illustrated by a threshold-linear response, which heavily depends on the assumption that cells optimize their

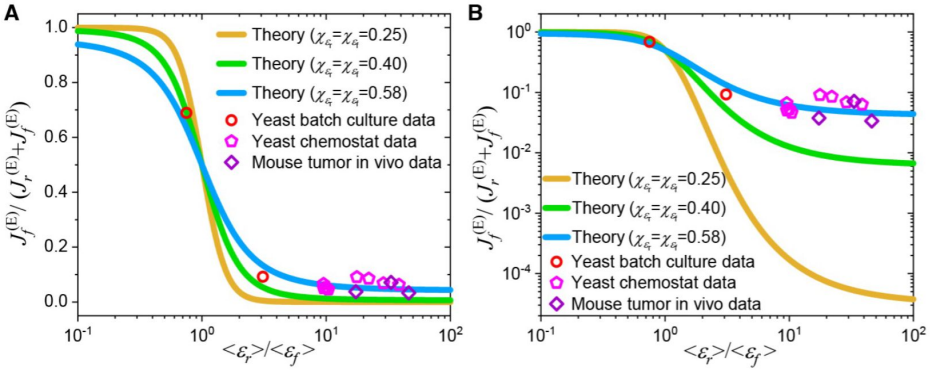

Fig. 5

Model comparison with data on the Crabtree effect in yeast and the Warburg effect in tumors.

(A) A linear scale representation on the y-axis. (**B**) A log scale representation on the y-axis. In (**A-B**), $\langle\varepsilon_r\rangle$ and $\langle\varepsilon_f\rangle$ represent the population averages of ε_r and ε_f, while $\chi_{\varepsilon r}$ and $\chi_{\varepsilon f}$ are the coefficients of variation (CVs) of ε_r and ε_f. $\langle\varepsilon_r\rangle/\langle\varepsilon_f\rangle$ represents the ratio of proteome efficiency between respiration and fermentation at the population-averaged level, while $J_f^{(E)}/(J_f^{(E)}+J_r^{(E)})$ stands for the fraction of energy flux generated by the fermentation pathway (see Eq. 6). The data for yeast in batch culture and chemostat were calculated from experimental data of *S. cerevisiae* and *I. orientalis* (Shen et al., 2024). The data for mouse tumors were calculated from in vivo experimental data of pancreatic ductal adenocarcinoma (PDAC) and leukemic spleen of mice (Bartman et al., 2023; Shen et al., 2024). See Appendix 10 for detailed information on the experimental data sources (Bartman et al., 2023; Shen et al., 2024).

growth rate based on a given rate of carbon influx under each nutrient condition (or similar equivalents, see Appendix 6.3). However, in practice, for microbes or tumor cells grown in vitro or in vivo, the given factors are the identity and concentration of the nutrient (Molenaar et al., 2009; Scott et al., 2010; Wang et al., 2019), rather than the rate of carbon influx. Additionally, prevalent explanations (Basan et al., 2015; Chen and Nielsen, 2019) suggest that overflow metabolism originates from the proteome efficiency in fermentation always being higher than that in respiration (see Appendix 6.3 for details). While it has been observed in *E. coli* that proteome efficiency in fermentation is higher than that in respiration for cells cultured in lactose at saturated concentration (Basan et al., 2015), Shen et al. (Shen et al., 2024) reported that for many yeast and cancer cells, the proteome efficiency in fermentation is noticeably lower than that in respiration, despite the presence of aerobic glycolytic fermentation flux. This observation (Shen et al., 2024) evidently contradicts the prevalent explanations (Basan et al., 2015; Chen and Nielsen, 2019). Our model resolves this puzzle by significantly differing from existing rationales in its optimization principle, where we purely optimize cell growth rate without imposing a special constraint on carbon influx (see Appendix 6.3 for details). More importantly, our model incorporates cell heterogeneity, which is crucial for both explaining the threshold-analog response in overflow metabolism and for resolving this puzzle raised by Shen et al. (Shen et al., 2024).

In the homogeneous case, the optimal growth strategy for growth rate dependent fermentation flux results in a digital response (see Eq. S44), corresponding to an elementary flux mode (Müller et al., 2014; Wortel et al., 2014), which aligns with the numerical study by Molenaar *et al.* (Molenaar et al., 2009), yet is incompatible with the standard picture of overflow metabolism (Basan et al., 2015; Holms, 1996; Meyer et al., 1984; Nanchen et al., 2006; van Hoek et al., 1998). Furthermore, cells would not generate fermentation flux if the proteome efficiency in fermentation were higher than that in respiration under the optimal growth framework. By incorporating heterogeneity in enzyme catalytic rates (Davidi et al., 2016; Garcia-Contreras et al., 2012), the critical growth rate (i.e., threshold) shifts from a single value to a Gaussian distribution (see Eq. S45 and Appendix 7 for details; see also **Appendix-fig. 4**) across a cell population, thereby turning a digital response into the threshold-analog response observed in overflow metabolism (see **Fig. 1C**). Moreover, cell heterogeneity allows a fraction of cells to possess a larger proteome efficiency in fermentation than in respiration despite the overall proteome efficiency in respiration at the cell population level is higher than in fermentation. This mechanism facilitates the fermentation flux in yeast and cancer cells observed by Shen et al. (Shen et al., 2024) (see **Fig. 5A-B**).

Our model results, based on cell heterogeneity, are further supported by observed distributions of single-cell growth rates in *E. coli* (Wallden et al., 2016) (see **Appendix-fig. 2B**), and by experiments involving various types of perturbations (Basan et al., 2015; Holms, 1996; Hui et al., 2015), both in terms of acetate secretion patterns and gene expression in the central metabolic network (see **Fig. 2**–**4**, **Appendix-figs. 2D-E** and **3**). Furthermore, the heterogeneity patterns predicted by our model for fermentation and respiration modes within a cell population are validated by experiments on intra-tumor heterogeneity in glioblastoma using optical microscopy (Duraj et al., 2021) and align with the non-genetic heterogeneity observed in experiments with *S. cerevisiae* (Bagamery et al., 2020) and *E. coli* (Nikolic et al., 2013). Finally, our model can be broadly applied to address heterogeneity-related challenges in metabolism on a quantitative basis, including diverse metabolic strategies of cells in various environments (Bagamery et al., 2020; Duraj et al., 2021; Escalante-Chong et al., 2015; Hensley et al., 2016; Liu et al., 2015; Solopova et al., 2014; Wang et al., 2019).

Additional information

Author contributions

X.W. conceived and designed the project, developed the model, carried out the analytical and numerical calculations, and wrote the paper.

Competing Interest Statement

The author declares no competing interests.

Data, Materials, and Software Availability

All study data are included in the article and/or appendices.

Acknowledgements

The author thanks Chao Tang, Qi Ouyang, Yang-Yu Liu and Kang Xia for helpful discussions. This work was supported by National Natural Science Foundation of China (Grant Nos.12004443 and 12474207), Guangzhou Municipal Innovation Fund (Grant No.202102020284) and the Hundred Talents Program of Sun Yat-sen University.

Appendix 1 Model framework

Appendix 1.1 Proteome partition

Here we adopt the proteome partition framework similar to that introduced by Scott *et al.* (Scott et al., 2010). All proteins in a cell are classified into three classes: the fixed portion Q-class, the active ribosome-affiliated R-class, and the remaining catabolic/anabolic enzymes C-class. Each proteome class has a mass $M_i^{(\mathrm{P})}\ (i=\mathrm{Q,R,C})$ and mass fraction Q_i, where Q_Q is a constant, and we define $\varphi_{\max} = 1 - \varphi_Q$. In the exponential growth phase, the ribosome allocation for protein synthesis of each class is f_i, with $f_\mathrm{Q} + f_\mathrm{R} + f_\mathrm{C} = 1$.

To analyze cell growth optimization, we first consider the homogeneous case where all cells share identical biochemical parameters, simplifying the mass accumulation of the cell population into a "big cell". This simplification does not affect the value of growth rate λ. For bacteria, the protein turnover is negligible, so the mass accumulation of each class follows:

$$dM_i^{(\mathrm{P})}/dt = f_i \cdot k_\mathrm{T} \cdot N_\mathrm{R} \cdot m_\mathrm{AA}\ (i=\mathrm{Q,\ R,\ C}), \tag{S1}$$

where m_AA stands for the average molecular weight of amino acids, k_T is the translation rate, $N_\mathrm{R} = M_{\mathrm{rp}}^{(\mathrm{P})}/m_\mathrm{R}$ is the number of ribosomes, m_R is the protein mass of a single ribosome, and $M_{\mathrm{rp}}^{(\mathrm{P})}$ is the total protein mass of ribosomes, with $M_\mathrm{R}^{(\mathrm{P})}/M_{\mathrm{rp}}^{(\mathrm{P})} = \varsigma \approx 1.67$ (Neidhardt, 1996; Scott et al., 2010). For a specific stable nutrient environment, f_R and k_T are temporal invariants. Thus,

$$M_i^{(\mathrm{P})}(t) = M_i^{(\mathrm{P})}(0) + f_i/f_\mathrm{R} \cdot M_\mathrm{R}^{(\mathrm{P})}(0) \cdot \left[\exp(\lambda \cdot t) - 1\right]\ (i=\mathrm{Q,\ R,\ C}), \tag{S2}$$

where $\lambda = f_R \circ k_T \circ m_{AA}/(\varsigma \circ m_R)$, and the total protein mass of the cell population $M_{protein} = \sum_i^{Q,R,C} M_i^{(P)}$ follows:

$$M_{\text{protein}}(t) = M_{\text{protein}}(0) + M_R(0) \cdot \left[\exp(\lambda \cdot t) - 1\right] / f_R \,. \tag{S3}$$

Over a long period in the exponential growth phase (i.e., $t \to +\infty$), we have $\varphi_i = f_i$ (i = Q, R, C), and

$$\lambda = \phi_R \cdot \kappa_t \,, \tag{S4}$$

where $K_t = k_T \circ m_{AA}/(\varsigma \circ m_R)$.

Appendix 1.2 Precursor pools

Based on the entry points of the metabolic network, we classify the precursors of biomass components into five pools (**Fig. 1A-B**): a1 (entry point: G6P/F6P), a2 (entry point: GA3P/3PG/PEP), b (entry point: pyruvate/acetyl-CoA), c (entry point: a-ketoglutarate), and d (entry point: oxaloacetate). These five pools draw approximately $r_{a1} = 24\%$, $r_{a2} = 24\%$, $r_b = 28\%$, $r_c = 12\%$ and $r_d = 12\%$ of the carbon flux (Nelson et al., 2008; Wang et al., 2019). There are overlapping components between Pools a1 and a2 due to the joint synthesis of some precursors. Therefore, we use Pool a to represent both Pools a1 and a2 in the descriptions.

Appendix 1.3 Stoichiometric flux

We consider the following biochemical reaction between substrate S_i and enzyme E_i:

$$E_i + S_i \underset{d_i}{\overset{a_i}{\rightleftarrows}} E_i \cdot S_i \xrightarrow{k_i^{\text{cat}}} E_i + b_i \cdot S_{i+1} + c_i \cdot \text{CO}_2 \,, \tag{S5}$$

where a_i, d_i and k_i^{cat} are the reaction parameters, S_{i+1} is the product, b_i and c_i are the stoichiometric coefficients. For most of the reactions in the central metabolism, $b_i = 1$ and $c_i = 0$. The reaction rate follows Michaelis-Menten kinetics (Nelson et al., 2008):

$$v_i = k_i^{\text{cat}} \cdot [E_i] \cdot \frac{[S_i]}{[S_i] + K_i} \,, \tag{S6}$$

where $K_i = (d_i + k_i^{cat})/a_i$, $[E_i]$ and $[S_i]$ are the Michaelis constant, and the concentrations of enzyme E_i and substrate S_i, respectively. For this reaction (Eq. S5), $d[S_{i+1}]/dt = b_i \circ v_i$ and $d[S_i]/dt = -v_i$. In the cell population (the "big cell"), suppose that the cell volume is V_{cell}, then the stoichiometric flux of the reaction is:

$$J_i \equiv V_{\text{cell}} \cdot v_i \,. \tag{S7}$$

The copy number of enzyme E_i is $N_{E_i} = V_{cell} \circ [E_i]$ with a total weight of $M_{E_i} = N_{E_i} \circ m_{E_i}$, where m_{E_i} is the molecular weight of E_i. By defining the enzyme cost of an E_i molecule as $n_{E_i} = m_{E_i}/m_0$, where m_0 is a unit mass, then the cost of all E_i molecules is $\Phi_i = N_{E_i} \circ n_{E_i}$ (Wang et al., 2019). By further defining $\xi_i \equiv \frac{k_i^{\text{cat}}}{n_{E_i}} \cdot \frac{[S_i]}{[S_i] + K_i}$, then:

$$J_i = \Phi_i \cdot \xi_i \,. \tag{S8}$$

The mass fraction of enzyme E_i in the proteome is $\varphi_i = M_{E_i}/M_{\text{protein}}$, and thus:

$$\phi_i = \Phi_i \cdot \frac{m_0}{M_{\text{protein}}}. \tag{S9}$$

Appendix 1.4 Carbon flux and cell growth rate

To clarify the relation between the stoichiometric flux J_i and growth rate λ, we consider the carbon flux in the biomass production. The carbon mass of the cell population (the "big cell") is given by $M_{\text{carbon}} = M_{\text{protein}} \circ r_{\text{carbon}}/r_{\text{Proein}}$, where r_{carbon} and r_{protem} represent the mass fraction of carbon and protein within a cell. In the exponential growth phase, the carbon flux of the biomass production is given by:

$$J_{\text{BM}} = \frac{1}{m_{\text{carbon}}} \cdot \frac{dM_{\text{carbon}}}{dt} = \lambda \cdot \frac{M_{\text{carbon}}}{m_{\text{carbon}}}, \tag{S10}$$

where m_{carbon} is the mass of a carbon atom. In fact, the carbon mass flux per stoichiometry varies depending on the entry point of the precursor pool. Taking Pool b as an example, there are three carbon atoms in a molecule of the entry point metabolite (i.e., pyruvate). Assuming that carbon atoms are conserved from pyruvate to Pool b, then the carbon flux of Pool b is given by $J_b^{\text{carbon}} = J_b \cdot N_{\text{py}}^{\text{carbon}}$, where J_b is the stoichiometric flux from pyruvate to Pool b (**Fig. 1A-B**) and $N_{\text{py}}^{\text{carbon}}$ stands for the carbon number of a pyruvate molecule. Combining with Eq. **S10** and noting that $J_b^{\text{carbon}} = r_b \cdot J_{\text{BM}}$, we get $J_b \circ N_{\text{py}}^{\text{carbon}} \circ m_{\text{carbon}} = r_b \circ \lambda \circ M_{\text{carbon}}$. Similarly, for each precursor pool, we have:

$$J_i \cdot N_{\text{EP}_i}^{\text{carbon}} \cdot m_{\text{carbon}} = r_i \cdot \lambda \cdot M_{\text{carbon}} \left(i = a1,\ a2,\ b,\ c,\ d\right), \tag{S11}$$

where the subscript "EP_i" represents the entry point of Pool i, and $N_{\text{EP}_i}^{\text{carbon}}$ is the number of carbon atoms in a molecule of the entry-point metabolite.

For each substrate in intermediate steps of the metabolic network, we define K_i as the substrate quality:

$$\kappa_i \equiv \xi_i \cdot \frac{r_{\text{protein}}}{r_{\text{carbon}}} = \frac{r_{\text{protein}}}{r_{\text{carbon}}} \cdot \frac{k_i^{\text{cat}}}{n_{E_i}} \cdot \frac{[S_i]}{[S_i] + K_i}, \tag{S12}$$

and for each precursor pool, we define:

$$\eta_i \equiv r_i \cdot m_0 \Big/ \left(N_{\text{EP}_i}^{\text{carbon}} \cdot m_{\text{carbon}}\right) \left(i = a1,\ a2,\ b,\ c,\ d\right). \tag{S13}$$

Combining Eqs. **S8**, **S9** and **S11**, we have

$$\phi_i \cdot \kappa_i = \eta_i \cdot \lambda \left(i = a1,\ a2,\ b,\ c,\ d\right). \tag{S14}$$

Then, we define the normalized flux, which can be regarded as the flux per unit of biomass:

$$J_i^{(\text{N})} \equiv \phi_i \cdot \kappa_i, \tag{S15}$$

where the superscript "(N)" stands for normalized. Combined with Eqs. **S8**, **S9** and **S12**, we have:

$$J_i^{(\mathrm{N})} \equiv J_i \cdot \frac{m_0}{M_{\mathrm{carbon}}}. \tag{S16}$$

Since $\sum_i^{a1,a2,b,c,d} r_i = 1$, by setting

$$m_0 = \left[\sum_i r_i \Big/ N_{\mathrm{EP}_i}^{\mathrm{carbon}}\right]^{-1} \cdot m_{\mathrm{carbon}}, \tag{S17}$$

we then obtain:

$$\eta_i = \frac{r_i}{N_{\mathrm{EP}_i}^{\mathrm{carbon}}} \cdot \left[\sum_j^{a1,a2,b,c,d} \frac{r_j}{N_{\mathrm{EP}_j}^{\mathrm{carbon}}}\right]^{-1} \left(i = a1,\ a2,\ b,\ c,\ d\right), \tag{S18}$$

and we have $\sum_i^{a1,a2,b,c,d} \eta_i = 1$, and

$$\sum_i^{a1,a2,b,c,d} \phi_i \cdot \kappa_i = \lambda. \tag{S19}$$

Appendix 1.5 Intermediate nodes

In a metabolic network, the metabolites between the carbon source and precursor pools are referred to as intermediate nodes. As specified by Wang *et al.* (Wang et al., 2019), to optimize cell growth rate, the substrate of each intermediate node is nearly saturated, and thus:

$$\kappa_i \approx \frac{r_{\mathrm{protein}}}{r_{\mathrm{carbon}}} \cdot \frac{k_i^{\mathrm{cat}}}{n_{E_i}}. \tag{S20}$$

Real cases could be more complicated due to other forms of metabolic regulations. Recent quantitative studies (Bennett et al., 2009; Park et al., 2016) have shown that, at least in *E. coli*, for most of the substrate-enzyme pairs, K_i is lower than the substrate concentration (i.e., $[S_i] > K_i$), which implies $\kappa_i \approx \frac{r_{\mathrm{protein}}}{r_{\mathrm{carbon}}} \cdot \frac{k_i^{\mathrm{cat}}}{n_{E_i}}$.

Appendix 2 Model and analysis

Appendix 2.1 Coarse-grained model

In the coarse-grained model shown in **Fig. 1B**, node *A* represents an arbitrary carbon source of Group A (Wang et al., 2019), which joins at the upper part of glycolysis. Nodes M1, M2, M3, M4, and M5 stand for G6P, PEP, acetyl-CoA, a-ketoglutarate, and oxaloacetate, respectively. In the analysis of carbon supply into precursor pools, we lump sum G6P/F6P as M1, GA3P/3PG/PEP as M2, and pyruvate/acetyl-CoA as M3 for approximation. For the biochemical reactions, each follows Eq. S5 with $b_i = 1$ except for M1 → 2M2 and M3+M5 → M4. Basically, there are three independent possible fates for a Group A carbon source (e.g., glucose, see **Appendix-fig. 1C-E**) (Chen and Nielsen, 2019): energy biogenesis through fermentation; energy biogenesis via respiration

(**Appendix-fig.1C-D**), or conversion into biomass components accompanied by energy biogenesis in the biomass pathway. Each fate involves a distinct fraction of the proteome, with no overlap between them (**Appendix-fig. 1**).

By applying flux balance to the stoichiometric fluxes and combining with Eq. **S8**, we have:

$$\begin{cases} \Phi_A \cdot \xi_A = \Phi_1 \cdot \xi_1 + \Phi_{a1} \cdot \xi_{a1}, \\ 2\Phi_1 \cdot \xi_1 = \Phi_2 \cdot \xi_2 + \Phi_5 \cdot \xi_5 + \Phi_{a2} \cdot \xi_{a2}, \\ \Phi_2 \cdot \xi_2 = \Phi_3 \cdot \xi_3 + \Phi_6 \cdot \xi_6 + \Phi_b \cdot \xi_b, \\ \Phi_5 \cdot \xi_5 + \Phi_4 \cdot \xi_4 = \Phi_3 \cdot \xi_3 + \Phi_d \cdot \xi_d, \\ \Phi_3 \cdot \xi_3 = \Phi_4 \cdot \xi_4 + \Phi_c \cdot \xi_c. \end{cases} \tag{S21}$$

Obviously, the stoichiometric fluxes of respiration J_r and fermentation J_f (**Appendix-fig. 1C-D**) are:

$$\begin{cases} J_r \equiv J_4 = \Phi_4 \cdot \xi_4, \\ J_f \equiv J_6 = \Phi_6 \cdot \xi_6. \end{cases} \tag{S22}$$

We further assume that the carbon atoms are conserved from each entry point metabolite to the precursor pool, and then,

$$\Phi_i \cdot \xi_i \cdot N_{\mathrm{EP}_i}^{\mathrm{carbon}} = r_i \cdot J_{\mathrm{BM}} \left(i = a1,\ a2,\ b,\ c,\ d \right). \tag{S23}$$

In terms of energy biogenesis for the relevant reactions, for convenience, we convert all the energy currencies into ATPs, namely, NADH→2ATP (Neidhardt et al., 1990), NADPH→2ATP (Neidhardt et al., 1990; Sauer et al., 2004), $FADH_2$→1ATP (Neidhardt et al., 1990). Then, we have

$$\beta_1 \cdot \Phi_1 \cdot \xi_1 + \beta_2 \cdot \Phi_2 \cdot \xi_2 + \beta_3 \cdot \Phi_3 \cdot \xi_3 + \beta_4 \cdot \Phi_4 \cdot \xi_4 + \beta_6 \cdot \Phi_6 \cdot \xi_6 + \beta_{a1} \cdot \Phi_{a1} \cdot \xi_{a1} = J_{\mathrm{E}}, \tag{S24}$$

where J_{E} represents the energy demand for cell proliferation, expressed as the stoichiometric energy flux in ATP. β_i is the stoichiometric coefficient with β_1 = 4, β_2 = 3, β_3 = 2 , β_4 = 6, β_6 = 1, and β_{a1} = 4 for *E. coli* (Neidhardt et al., 1990; Sauer et al., 2004). For bacteria, the energy demand is generally proportional to the carbon flux infused into biomass production, as the proportion of maintenance energy is roughly negligible (Locasale and Cantley, 2010). Thus,

$$J_{\mathrm{E}} = r_{\mathrm{E}} \cdot J_{\mathrm{BM}}, \tag{S25}$$

where r_{E} is the ratio and also a constant.

By applying the substitutions specified in Eqs. S9, S12, S14–S18, combined with Eqs. S4, S10, S21–S25, and the constraint of proteome resource allocation $\varphi_R + \varphi_C = \varphi_{\max}$, we have:

$$\begin{cases} \phi_A \cdot \kappa_A = \phi_1 \cdot \kappa_1 + \phi_{a1} \cdot \kappa_{a1}, \\ 2\phi_1 \cdot \kappa_1 = \phi_2 \cdot \kappa_2 + \phi_5 \cdot \kappa_5 + \phi_{a2} \cdot \kappa_{a2}, \\ \phi_2 \cdot \kappa_2 = \phi_3 \cdot \kappa_3 + \phi_6 \cdot \kappa_6 + \phi_b \cdot \kappa_b, \\ \phi_5 \cdot \kappa_5 + \phi_4 \cdot \kappa_4 = \phi_3 \cdot \kappa_3 + \phi_d \cdot \kappa_d, \\ \phi_3 \cdot \kappa_3 = \phi_4 \cdot \kappa_4 + \phi_c \cdot \kappa_c, \\ \phi_{a1} \cdot \kappa_{a1} = \eta_{a1} \cdot \lambda, \phi_{a2} \cdot \kappa_{a2} = \eta_{a2} \cdot \lambda, \phi_b \cdot \kappa_b = \eta_b \cdot \lambda, \phi_c \cdot \kappa_c = \eta_c \cdot \lambda, \phi_d \cdot \kappa_d = \eta_d \cdot \lambda, \\ \beta_1 \cdot \phi_1 \cdot \kappa_1 + \beta_2 \cdot \phi_2 \cdot \kappa_2 + \beta_3 \cdot \phi_3 \cdot \kappa_3 + \beta_4 \cdot \phi_4 \cdot \kappa_4 + \beta_6 \cdot \phi_6 \cdot \kappa_6 + \beta_{a1} \cdot \phi_{a1} \cdot \kappa_{a1} = J_{\mathrm{E}}^{(\mathrm{N})}, \\ J_{\mathrm{E}}^{(\mathrm{N})} = \eta_{\mathrm{E}} \cdot \lambda, \lambda = \phi_R \cdot \kappa_t, J_r^{(\mathrm{N})} = \phi_4 \cdot \kappa_4, J_f^{(\mathrm{N})} = \phi_6 \cdot \kappa_6, \\ \phi_{\mathrm{R}} + \phi_A + \phi_1 + \phi_2 + \phi_3 + \phi_4 + \phi_5 + \phi_6 + \phi_{a1} + \phi_{a2} + \phi_b + \phi_c + \phi_d = \phi_{\max}, \end{cases} \tag{S26}$$

where $J_{\mathrm{E}}^{(\mathrm{N})}$ and η_{E} are defined as $J_{\mathrm{E}}^{(\mathrm{N})} \equiv J_E \cdot \frac{m_0}{M_{\mathrm{carbon}}}$ and $\eta_{\mathrm{E}} \equiv r_{\mathrm{E}} \cdot \left[\sum_i r_i / N_{\mathrm{EP}_i}^{\mathrm{carbon}} \right]^{-1}$, respectively.

Here, for each intermediate node, K_i follows Eq. S20, which can be approximated as a constant. The substrate quality of the Group A carbon source k_A varies with the identity and concentration of the Group A carbon source:

$$\kappa_A \equiv \frac{r_{\mathrm{protein}}}{r_{\mathrm{carbon}}} \cdot \frac{k_A^{\mathrm{cat}}}{m_{E_A}} \cdot \frac{[A]}{[A] + K_A} \cdot m_0, \tag{S27}$$

which is determined externally by the culture condition. From Eq. S26, all φ_i and φ_{R} can be expressed in terms of $J_r^{(\mathrm{N})}$, $J_f^{(\mathrm{N})}$ and λ:

$$\begin{cases} \phi_A = \left[J_r^{(\mathrm{N})} + J_f^{(\mathrm{N})} + \left(2\eta_{a1} + \eta_{a2} + \eta_b + 2\eta_c + \eta_d \right) \lambda \right] \Big/ \left(2 \cdot \kappa_A \right), \\ \phi_1 = \left[J_r^{(\mathrm{N})} + J_f^{(\mathrm{N})} + \left(\eta_{a2} + \eta_b + 2\eta_c + \eta_d \right) \lambda \right] \Big/ \left(2 \cdot \kappa_1 \right), \\ \phi_2 = \left[J_r^{(\mathrm{N})} + J_f^{(\mathrm{N})} + \left(\eta_b + \eta_c \right) \lambda \right] \Big/ \kappa_2, \\ \phi_3 = \left(J_r^{(\mathrm{N})} + \eta_c \cdot \lambda \right) \Big/ \kappa_3, \phi_4 = J_r^{(\mathrm{N})} \Big/ \kappa_4, \\ \phi_5 = \left(\eta_c + \eta_d \right) \lambda \Big/ \kappa_5, \phi_6 = J_f^{(\mathrm{N})} \Big/ \kappa_6, \phi_R = \lambda / \kappa_t, \\ \phi_i = \eta_i \cdot \lambda / \kappa_i \quad \left(i = a1,\ a2,\ b,\ c,\ d \right). \end{cases} \tag{S28}$$

In Eq. S28, for each φ_i or φ_R, the $J_r^{(\mathrm{N})}$- and $J_f^{(\mathrm{N})}$-related proteome fraction terms belong to the fractions of the proteome dedicated to respiration (denoted as *far*) and fermentation (denoted as *faf*), respectively. The *2* -related proteome fraction terms belong to those involved in the biomass

synthesis pathway (denoted as φ_{BM}). Thus, $\phi_r = J_r^{(\mathrm{N})} \cdot \left[1/(2\cdot\kappa_A)+1/(2\cdot\kappa_1)+1/\kappa_2+1/\kappa_3+1/\kappa_4\right]$, $\phi_f = J_f^{(\mathrm{N})} \cdot \left[1/(2\cdot\kappa_A)+1/(2\cdot\kappa_1)+1/\kappa_2+1/\kappa_6\right]$, and $\phi_{\mathrm{BM}} = \lambda \cdot \left(\frac{1}{\kappa_t}+\frac{1+\eta_{a1}+\eta_c}{2\kappa_A}+\frac{1-\eta_{a1}+\eta_c}{2\kappa_1}+\frac{\eta_b+\eta_c}{\kappa_2}+\frac{\eta_c}{\kappa_3}+\frac{\eta_c+\eta_d}{\kappa_5}+\sum_i^{a1,a2,b,c,d}\frac{\eta_i}{\kappa_i}\right)$. By substituting Eq. S28 into Eq. S26, we have:

$$\begin{cases} J_r^{(\mathrm{E})} + J_f^{(\mathrm{E})} = \varphi \cdot \lambda, \\ \dfrac{J_r^{(\mathrm{E})}}{\varepsilon_r} + \dfrac{J_f^{(\mathrm{E})}}{\varepsilon_f} = \phi_{\max} - \psi \cdot \lambda. \end{cases} \tag{S29}$$

Here, $J_r^{(\mathrm{E})}$ and $J_f^{(\mathrm{E})}$ stand for the normalized energy fluxes of respiration and fermentation, with

$$\begin{cases} J_r^{(\mathrm{E})} = \beta_r^{(A)} \cdot J_r^{(\mathrm{N})} / 2, \\ J_f^{(\mathrm{E})} = \beta_f^{(A)} \cdot J_f^{(\mathrm{N})} / 2, \end{cases} \tag{S30}$$

where $\beta_r^{(A)} = \beta_1 + 2(\beta_2 + \beta_3 + \beta_4)$ and $\beta_f^{(A)} = \beta_1 + 2(\beta_2 + \beta_6)$, with $\beta_r^{(A)} = 26$ and $\beta_f^{(A)} = 12$ for *E. coli*. ε_r and ε_f represent the proteome efficiencies for energy biogenesis in the respiration and fermentation pathways (**Appendix-fig. 1C-D**), defined as $\varepsilon_r = J_r^{(\mathrm{E})}/\phi_r$ and $\varepsilon_f \equiv J_f^{(\mathrm{E})} / \phi_f$; that is, the normalized energy fluxes expressed in ATP generated per proteomic mass fraction dedicated to respiration and fermentation, respectively. Hence,

$$\begin{cases} \varepsilon_r = \dfrac{\beta_r^{(A)}}{1/\kappa_A + 1/\kappa_1 + 2/\kappa_2 + 2/\kappa_3 + 2/\kappa_4}, \\ \varepsilon_f = \dfrac{\beta_f^{(A)}}{1/\kappa_A + 1/\kappa_1 + 2/\kappa_2 + 2/\kappa_6}. \end{cases} \tag{S31}$$

ψ^{-1} is the proteome efficiency for biomass generation in the biomass synthesis pathway (**Appendix-fig. 1E**), defined as $\psi^{-1} \equiv \lambda/\phi_{\mathrm{BM}} = \sum_i^{a1,a2,b,c,d} J_i^{(\mathrm{N})} / \phi_{\mathrm{BM}}$ (see Eqs. **S15** and **S19**); that is, the normalized flux (which differs from the normalized energy flux used to define ε_r and ε_f) generated per proteomic mass fraction dedicated to biomass synthesis. Hence

$$\psi = \frac{1}{\kappa_t} + \frac{1+\eta_{a1}+\eta_c}{2\kappa_A} + \frac{\eta_{a2}+\eta_b+2\eta_c+\eta_d}{2\kappa_1} + \frac{\eta_b+\eta_c}{\kappa_2} + \frac{\eta_c}{\kappa_3} + \frac{\eta_c+\eta_d}{\kappa_5} + \sum_i^{a1,a2,b,c,d}\frac{\eta_i}{\kappa_i}. \tag{S32}$$

ϕ is an energy demand coefficient (a constant), with

$$\varphi \equiv \eta_{\mathrm{E}} - \beta_1 \cdot \left(\eta_{a2} + \eta_b + 2\eta_c + \eta_d\right)/2 - \beta_2 \cdot \left(\eta_b + \eta_c\right) - \beta_3 \cdot \eta_c - \beta_{a1} \cdot \eta_{a1}, \tag{S33}$$

and ϕ ° 2 stands for the normalized flux of energy demand other than the accompanying energy biogenesis from the biomass synthesis pathway.

Appendix 2.2 The reason for overflow metabolism

Microbes optimize their growth rate to survive through the evolutionary process (Vander Heiden et al., 2009). The optimal growth principle also roughly holds for tumor cells, which proliferate while ignoring growth restriction signals and evading immune destruction by the host (Vander

Heiden et al., 2009). First, we consider the optimal growth strategy for a single cell. The coarsegrained model for bacteria is summarized in Eq. S26 and further simplified in Eq. S29. Here, ε_r, ε_f and ψ are functions of κ_A (see Eqs. S31, S32), so we also denote them as $\varepsilon_r(\kappa_A)$, $\varepsilon_f(\kappa_A)$, $\psi(\kappa_A)$. Evidently, the fluxes of both respiration and fermentation take non-negative values, i.e., $J_r^{(E)}$, $J_f^{(E)} \geq 0$, and all the coefficients are positive: $\varepsilon_r(\kappa_A)$, $\varepsilon_f(\kappa_A)$, $\psi(\kappa_A)$,$\phi > 0$.

Thus, if $\varepsilon_r > \varepsilon_f$, then $(\psi + \phi/\varepsilon_r)\cdot\lambda = \varphi_{\max} - J_f^{(E)}(1/\varepsilon_f - 1/\varepsilon_r) \leq \varphi_{\max}$. Obviously, the solution for optimal growth is:

$$\begin{cases} J_f^{(E)} = 0, \\ J_r^{(E)} = \varphi \cdot \lambda. \end{cases} \qquad \varepsilon_r > \varepsilon_f. \tag{S34}$$

Similarly, if $\varepsilon_f > \varepsilon_r$, then the optimal growth solution is:

$$\begin{cases} J_f^{(E)} = \varphi \cdot \lambda, \\ J_r^{(E)} = 0. \end{cases} \qquad \varepsilon_r < \varepsilon_f. \tag{S35}$$

In both cases, the growth rate λ takes the maximum value for a given nutrient condition (i.e., given κ_A):

$$\lambda = \begin{cases} \lambda_r \equiv \dfrac{\phi_{\max}}{\varphi/\varepsilon_r(\kappa_A) + \psi(\kappa_A)} & \varepsilon_r(\kappa_A) > \varepsilon_f(\kappa_A), \\ \lambda_f \equiv \dfrac{\phi_{\max}}{\varphi/\varepsilon_f(\kappa_A) + \psi(\kappa_A)} & \varepsilon_r(\kappa_A) < \varepsilon_f(\kappa_A). \end{cases} \tag{S36}$$

So, why do microbes use the seemingly wasteful fermentation pathway when the growth rate is large under aerobic conditions? Prevalent explanations (Basan et al., 2015; Chen and Nielsen, 2019) suggest that it originates from that the proteome efficiency in fermentation is consistently higher than in respiration (i.e., $\varepsilon_f > \varepsilon_r$). If this is the case, why do microbes still use the normal respiration pathway when the growth rate is small? The answer lies in the fact that both $\varepsilon_r(\kappa_A)$ and $\varepsilon_f(\kappa_A)$ are not constants, but are dependent on nutrient conditions. In Eq. S31, when κ_A is small, consider the extreme case of $\kappa_A \to 0$, and then

$$\begin{cases} \varepsilon_r(\kappa_A \to 0) \approx \beta_r^{(A)} \cdot \kappa_A, \\ \varepsilon_f(\kappa_A \to 0) \approx \beta_f^{(A)} \cdot \kappa_A. \end{cases} \tag{S37}$$

Since $\beta_r^{(A)} \gg \beta_f^{(A)}$, clearly,

$$\varepsilon_r(\kappa_A \to 0) > \varepsilon_f(\kappa_A \to 0). \tag{S38}$$

Combined with Eq. S36, thus cells would certainly use the respiration pathway when the growth rate is very small. Meanwhile, suppose that $\kappa_A^{\max}$ is the maximum value of κ_A available across different Group A carbon sources, and if there exists a κ_A (with $\kappa_A \le \kappa_A^{\max}$) satisfying $\varepsilon_r(\kappa_A) < \varepsilon_f(\kappa_A)$, specifically,

$$\frac{\beta_r^{(A)}-\beta_f^{(A)}}{\kappa_A} < \beta_f^{(A)}\left(\frac{1}{\kappa_1}+\frac{2}{\kappa_2}+\frac{2}{\kappa_3}+\frac{2}{\kappa_4}\right)-\beta_r^{(A)}\cdot\left(\frac{1}{\kappa_1}+\frac{2}{\kappa_2}+\frac{2}{\kappa_6}\right), \tag{S39}$$

then $\Delta(\kappa_A) \equiv \varepsilon_f(\kappa_A)/\varepsilon_r(\kappa_A)$ is a monotonically increasing function of κ_A. Thus,

$$\varepsilon_r\left(\kappa_A^{\max}\right) < \varepsilon_f\left(\kappa_A^{\max}\right), \tag{S40}$$

and cells would use the fermentation pathway when the growth rate is large.

In practice, experimental studies using *E. coli* (Basan et al., 2015) have demonstrated that proteome efficiency in fermentation is higher than in respiration when the Group A carbon source is lactose at a saturated concentration, i.e., $\varepsilon_r(\kappa_{\text{lactose}}^{(\text{ST})}) < \varepsilon_f(\kappa_{\text{lactose}}^{(\text{ST})})$. Here, $\kappa_{\text{lactose}}^{(\text{ST})}$ represents the substrate quality of lactose and the superscript "(ST)" signifies saturated concentration. In fact, *E. coli* grows much faster in G6p than lactose (Basan et al., 2015), thus, $\kappa_A^{\max} > \kappa_{\text{lactose}}^{(\text{ST})}$, and hence, Eq. S40 holds for *E. coli*. From a theoretical perspective, we can verify Eq. S39 and consequently Eq. S40 using Eq. S20, combined with the in vivo/in vitro biochemical parameters obtained from experimental data (see **Appendix-tables 1**–**2**). For example, it is straightforward to confirm that $\varepsilon_r(\kappa_{\text{glucose}}^{(\text{ST})}) < \varepsilon_f(\kappa_{\text{glucose}}^{(\text{ST})})$ using this method (see **Appendix 8.2**), further supporting the validity of Eqs. **S39**–**S40** (see also **Appendix 9**).

Now that Eqs. **S38**–**S40** are all valid, a critical value of κ_A, denoted as $\kappa_A^{(\text{C})}$, exists, satisfying $\Delta(\kappa_A^{(\text{C})}) = 1$. Thus,

$$\begin{cases} \varepsilon_f(\kappa_A) > \varepsilon_r(\kappa_A), & \kappa_A > \kappa_A^{(\text{C})}; \\ \varepsilon_f(\kappa_A) = \varepsilon_r(\kappa_A), & \kappa_A = \kappa_A^{(\text{C})}; \\ \varepsilon_f(\kappa_A) < \varepsilon_r(\kappa_A), & \kappa_A < \kappa_A^{(\text{C})}. \end{cases} \tag{S41}$$

Combined with Eq. **S31**, we have:

$$\kappa_A^{(\text{C})} = \frac{\beta_r^{(A)}-\beta_f^{(A)}}{\beta_f^{(A)}\left(1/\kappa_1+2/\kappa_2+2/\kappa_3+2/\kappa_4\right)-\beta_r^{(A)}\left(1/\kappa_1+2/\kappa_2+2/\kappa_6\right)}. \tag{S42}$$

By substituting Eq. **S42** into Eqs. **S31**, **S32** and **S36**, we obtain the expressions for ε_r ( ), ε_f ( ) and the critical growth rate at the transition point (i.e., $\lambda_C \equiv \lambda($ $)$):

$$\begin{cases} \varepsilon_r\left(\kappa_A^{(C)}\right) = \varepsilon_f\left(\kappa_A^{(C)}\right) = \dfrac{\beta_r^{(A)} - \beta_f^{(A)}}{2\left(1/\kappa_3 + 1/\kappa_4 - 1/\kappa_6\right)} = \dfrac{\beta_3 + \beta_4 - \beta_6}{1/\kappa_3 + 1/\kappa_4 - 1/\kappa_6}, \\ \lambda_C = \dfrac{\phi_{\max}}{\varphi / \varepsilon_{r/f}\left(\kappa_A^{(C)}\right) + \psi\left(\kappa_A^{(C)}\right)}, \end{cases} \tag{S43}$$

where $\varepsilon_{r|f}$ represents either ε_r or ε_f. In **Fig. 1E**, we show the dependencies of $\kappa_r(\kappa_A)$, $\varepsilon_f(\kappa_A)$ and $\lambda(\varepsilon_A)$ on ε_A in a 3-dimensional form, as ε_A changes.

Appendix 2.3 The relation between respiration/fermentation flux and growth rate

We proceed to study the relation between the respiration/fermentation flux and the cell growth rate. From Eqs. **S16** and **S30**, we see that the stoichiometric fluxes J_r, J_f, the normalized fluxes , and the normalized energy fluxes , are all interconvertible. For convenience, we first analyze the relations between , and λ under growth rate optimization. In fact, all these terms are merely functions of κ_A (see Eqs. **S34**–**S36**), which is determined by the nutrient condition (Eq. **S27**).

In the homogeneous case, where all microbes share identical biochemical parameters, as $\lambda(\kappa_A)$ increases with κ_A, appear abruptly and vanish simultaneously as κ_A exceeds (**Fig. 1E**, see also Eqs. **S34**–**S35**, **S41**). Combining Eqs. **S34**–**S36** and **S43**, we obtain:

$$\begin{cases} J_f^{(E)} = \varphi \cdot \lambda \cdot \theta\left(\lambda - \lambda_C\right), \\ J_r^{(E)} = \varphi \cdot \lambda \cdot \left[1 - \theta\left(\lambda - \lambda_C\right)\right], \end{cases} \tag{S44}$$

where "θ" stands for the Heaviside step function. Defining $\lambda_{\max} = \lambda($ $)$, and then, $[0, \lambda_{\max}]$ is the relevant range of the x axis. In fact, the digital responses in Eq. **S44** are consistent with the numerical simulation results of Molenaar *et al.* (Molenaar et al., 2009). However, these results are incompatible with the threshold-analog response in the standard picture of overflow metabolism (Basan et al., 2015; Holms, 1996).

In practice, the values of can be greatly influenced by the concentrations of potassium and phosphate (Garda-Contreras et al., 2012), which vary from cell to cell. Consequently, there is a distribution of values for among cell populations, commonly referred to as extrinsic noise (Elowitz et al., 2002). For convenience, we assume that each (and thus κ_i) follows a Gaussian distribution with a coefficient of variation (CV) of 25%. Therefore, the distribution of λ_C can be approximated by a Gaussian distribution (see Appendix 7.1):

$$\lambda_C \sim \mathcal{N}\left(\mu_{\lambda_C}, \sigma_{\lambda_C}^2\right), \tag{S45}$$

where $\mu_{\lambda C}$ and $\sigma_{\lambda C}$ represent the mean and standard deviation of λ_C, with the CV $\sigma_{\lambda C}/\mu_{\lambda C}$ calculated to be 12% (see Appendix 8.2 for details). Note that λ is κ_A dependent, while λ_C is independent of κ_A. Thus, given the growth rate of microbes in a culturing medium (e.g., in a chemostat), the normalized energy fluxes are:

$$\begin{cases} J_f^{(\mathrm{E})}(\lambda) = \dfrac{1}{2}\varphi\cdot\lambda\cdot\left[\mathrm{erf}\left(\dfrac{\lambda-\mu_{\lambda_C}}{\sqrt{2}\sigma_{\lambda_C}}\right)+1\right], \\ J_r^{(\mathrm{E})}(\lambda) = \dfrac{1}{2}\varphi\cdot\lambda\cdot\left[1-\mathrm{erf}\left(\dfrac{\lambda-\mu_{\lambda_C}}{\sqrt{2}\sigma_{\lambda_C}}\right)\right], \end{cases} \tag{S46}$$

where "erf" represents the error function. In practice, given a culturing medium, there is also a probability distribution for the growth rate (**Appendix-fig. 2B**, see also Eq. **S157**). For approximation, in plotting the growth rate-flux relations, we use the deterministic (noise-free) value of the growth rate as a proxy. To compare with experiments, we essentially compare the normalized fluxes $J_r^{(\mathrm{N})}$, $J_f^{(\mathrm{N})}$ (see **Appendix 8.1** for details). Combining Eqs. **S30** and **S46**, we obtain:

$$\begin{cases} J_f^{(\mathrm{N})}(\lambda) = \dfrac{\varphi}{\beta_f^{(A)}}\cdot\lambda\cdot\left[\mathrm{erf}\left(\dfrac{\lambda-\mu_{\lambda_C}}{\sqrt{2}\sigma_{\lambda_C}}\right)+1\right], \\ J_r^{(\mathrm{N})}(\lambda) = \dfrac{\varphi}{\beta_r^{(A)}}\cdot\lambda\cdot\left[1-\mathrm{erf}\left(\dfrac{\lambda-\mu_{\lambda_C}}{\sqrt{2}\sigma_{\lambda_C}}\right)\right]. \end{cases} \tag{S47}$$

In **Fig. 1C-D**, we see that Eq. **S47** quantitatively illustrates the experimental data (Basan et al., 2015), where the model parameters were obtained using biochemical data for the catalytic enzymes (see **Appendix-table 1** for details).

Appendix 3 Model perturbations

Appendix 3.1 Overexpression of useless proteins

Here, we consider the case of overexpression of the protein encoded by the *lacZ* gene (i.e., φ_Z perturbation) in *E. coli*. Effectively, this limits the proteome by altering $\varphi_{\max}$:

$$\phi_{\max} \xrightarrow{\text{LacZ overexpression}} \phi_{\max} - \phi_Z, \tag{S48}$$

where φ_Z stands for the proteomic mass fraction of useless proteins, which is controllable in experiments. Then, the growth rate changes into a bivariate function of κ_A and φ_Z:

$$\lambda\left(\kappa_A,\phi_Z\right)=\begin{cases}\dfrac{\phi_{\max}-\phi_Z}{\varphi/\varepsilon_r\left(\kappa_A\right)+\psi\left(\kappa_A\right)} & \varepsilon_r\left(\kappa_A\right)>\varepsilon_f\left(\kappa_A\right),\\ \dfrac{\phi_{\max}-\phi_Z}{\varphi/\varepsilon_f\left(\kappa_A\right)+\psi\left(\kappa_A\right)} & \varepsilon_r\left(\kappa_A\right)<\varepsilon_f\left(\kappa_A\right),\end{cases} \tag{S49}$$

and thus,

$$\lambda\left(\kappa_A,\phi_Z\right)=\lambda\left(\kappa_A,0\right)\left(1-\phi_Z/\phi_{\max}\right). \tag{S50}$$

Obviously, $\kappa_A^{(C)}$ remains a constant (following Eq. **S42**), while $\lambda_C(\varphi_Z) = \lambda(\kappa_A^{(C)}, \varphi_Z)$ and $\lambda_{max}(\varphi_Z) \equiv \lambda(\kappa_A^{max}, \varphi_Z)$ become functions of φ_Z:

$$\begin{cases}\lambda_{\mathrm{C}}\left(\phi_Z\right)=\lambda_{\mathrm{C}}\left(0\right)\left(1-\phi_Z/\phi_{\max}\right),\\ \lambda_{\max}\left(\phi_Z\right)=\lambda_{\max}\left(0\right)\left(1-\phi_Z/\phi_{\max}\right).\end{cases} \tag{S51}$$

In the homogeneous case, $J_f^{(E)}$ and $J_r^{(E)}$ follow:

$$\begin{cases}J_f^{(\mathrm{E})}\left(\kappa_A,\phi_Z\right)=\varphi\cdot\lambda\left(\kappa_A,\phi_Z\right)\cdot\theta\left(\lambda\left(\kappa_A,\phi_Z\right)-\lambda_{\mathrm{C}}\left(\phi_Z\right)\right),\\ J_r^{(\mathrm{E})}\left(\kappa_A,\phi_Z\right)=\varphi\cdot\lambda\left(\kappa_A,\phi_Z\right)\cdot\left[1-\theta\left(\lambda\left(\kappa_A,\phi_Z\right)-\lambda_{\mathrm{C}}\left(\phi_Z\right)\right)\right].\end{cases} \tag{S52}$$

Combined with Eqs. **S50**–**S51**, we have:

$$\begin{cases}J_f^{(\mathrm{E})}\left(\kappa_A,\phi_Z\right)=\varphi\cdot\lambda\left(\kappa_A,\phi_Z\right)\cdot\theta\left(\lambda\left(\kappa_A,0\right)-\lambda_{\mathrm{C}}\left(0\right)\right),\\ J_r^{(\mathrm{E})}\left(\kappa_A,\phi_Z\right)=\varphi\cdot\lambda\left(\kappa_A,\phi_Z\right)\cdot\left[1-\theta\left(\lambda\left(\kappa_A,0\right)-\lambda_{\mathrm{C}}\left(0\right)\right)\right].\end{cases} \tag{S53}$$

To compare with experiments, we assume that each κ_i^{ref} and κ_i follow the extrinsic noise with a CV of 25% specified in **Appendix 2.3**, and we neglect the noise on φ_Z and φ_{max}. Combining Eqs. **S45** and **S51**, $\lambda_C(\varphi_Z)$ approximately follows a Gaussian distribution:

$$\lambda_{\mathrm{C}}\left(\phi_Z\right)\sim\mathcal{N}\left(\mu_{\lambda_{\mathrm{C}}}\left(\phi_Z\right),\sigma_{\lambda_{\mathrm{C}}}\left(\phi_Z\right)^2\right), \tag{S54}$$

where $\mu_{\lambda C}(\varphi_Z)$ and $\sigma_{\lambda C}(\varphi_Z)$ represent the mean and standard deviation of $\lambda_C(\varphi_Z)$, with

$$\begin{cases}\mu_{\lambda_{\mathrm{C}}}\left(\phi_Z\right)=\mu_{\lambda_{\mathrm{C}}}\left(0\right)\left(1-\phi_Z/\phi_{\max}\right),\\ \sigma_{\lambda_{\mathrm{C}}}\left(\phi_Z\right)=\sigma_{\lambda_{\mathrm{C}}}\left(0\right)\left(1-\phi_Z/\phi_{\max}\right).\end{cases} \tag{S55}$$

Here, $\mu_{\lambda C}(0)$, $\sigma_{\lambda C}(0)$, $\lambda_C(0)$, $\lambda_{max}(0)$ and $\lambda(\kappa_A, 0)$ represent the parameters or variables free from φ_Z perturbation, just as those in **Appendix 2.3**. Since the noise on the multiplier term (i.e., $1 - \varphi_z/\varphi_{max}$) is negligible, the CV of $\lambda_C(\varphi_Z)$ (i.e., $\sigma_{\lambda C}(\varphi_Z)/\mu_{\lambda C}(\varphi_Z)$) is unaffected by φ_z. By combining Eqs. **S46** and **S48**, we obtain the relations between the normalized energy fluxes and growth rate:

$$\begin{cases} J_f^{(E)}\left(\lambda\left(\kappa_A,\phi_Z\right),\phi_Z\right)=\dfrac{1}{2}\varphi\cdot\lambda\left(\kappa_A,\phi_Z\right)\cdot\left[\operatorname{erf}\left(\dfrac{\lambda\left(\kappa_A,\phi_Z\right)-\mu_{\lambda_C}\left(\phi_Z\right)}{\sqrt{2}\sigma_{\lambda_C}\left(\phi_Z\right)}\right)+1\right], \\ J_r^{(E)}\left(\lambda\left(\kappa_A,\phi_Z\right),\phi_Z\right)=\dfrac{1}{2}\varphi\cdot\lambda\left(\kappa_A,\phi_Z\right)\cdot\left[1-\operatorname{erf}\left(\dfrac{\lambda\left(\kappa_A,\phi_Z\right)-\mu_{\lambda_C}\left(\phi_Z\right)}{\sqrt{2}\sigma_{\lambda_C}\left(\phi_Z\right)}\right)\right], \end{cases} \tag{S56}$$

where $\lambda(\kappa_A, \varphi_Z)$, $\mu_{\lambda C}(\varphi_Z)$ and $\sigma_{\lambda C}(\varphi_Z)$ follow Eqs. **S50** and **S55** accordingly. For a given value of φ_Z, i.e., φ_Z is fixed, then, $\lambda(\kappa_A, \varphi_Z)$ changes monotonically with φ_A. Combining Eqs. **S55** - **S56** and **S30**, we obtain the relation between the normalized fluxes $J_r^{(N)}$, $J_f^{(N)}$ and the growth rate (where φ_Z is a parameter):

$$\begin{cases} J_f^{(N)}\left(\lambda,\phi_Z\right)=\dfrac{\varphi}{\beta_f^{(A)}}\cdot\lambda\cdot\left[\operatorname{erf}\left(\dfrac{\lambda-\mu_{\lambda_C}\left(0\right)\left(1-\phi_Z/\phi_{max}\right)}{\sqrt{2}\sigma_{\lambda_C}\left(0\right)\left(1-\phi_Z/\phi_{max}\right)}\right)+1\right], \\ J_r^{(N)}\left(\lambda,\phi_Z\right)=\dfrac{\varphi}{\beta_r^{(A)}}\cdot\lambda\cdot\left[1-\operatorname{erf}\left(\dfrac{\lambda-\mu_{\lambda_C}\left(0\right)\left(1-\phi_Z/\phi_{max}\right)}{\sqrt{2}\sigma_{\lambda_C}\left(0\right)\left(1-\phi_Z/\phi_{max}\right)}\right)\right]. \end{cases} \tag{S57}$$

In **Fig. 2C**. we show that the model predictions (Eq. **S57**) quantitatively agree with the experiments (Basan et al., 2015).

Meanwhile, we can also perturb the growth rate by tuning φ_Z in a stable culturing environment with fixed concentration of a Group A carbon source (i.e., given [A]). In fact, for this case there is a distribution of φ_A values due to the extrinsic noise in k_A^{cat}, yet this distribution is fixed. For convenience of description, we still referred to it as fixed κ_A. Then, combining Eqs. S30, S50, S55 and S56, we get:

$$\begin{cases} J_f^{(N)}\left(\lambda,\phi_Z\right)=\dfrac{\varphi}{\beta_f^{(A)}}\cdot\left[\operatorname{erf}\left(\dfrac{\lambda\left(\kappa_A,0\right)-\mu_{\lambda_C}\left(0\right)}{\sqrt{2}\sigma_{\lambda_C}\left(0\right)}\right)+1\right]\cdot\lambda, \\ J_r^{(N)}\left(\lambda,\phi_Z\right)=\dfrac{\varphi}{\beta_r^{(A)}}\cdot\left[1-\operatorname{erf}\left(\dfrac{\lambda\left(\kappa_A,0\right)-\mu_{\lambda_C}\left(0\right)}{\sqrt{2}\sigma_{\lambda_C}\left(0\right)}\right)\right]\cdot\lambda. \end{cases} \tag{S58}$$

Here, $\lambda(\kappa_A, 0)$ remains unaltered as κ_A is fixed. Therefore, in this case, $J_f^{(N)}$ and $J_r^{(N)}$ are proportional to λ, where the slopes are both functions of κ_A. More specifically, the slope of $J_f^{(N)}$ is a monotonically increasing function of κ_A, while that of $J_r^{(N)}$ is a monotonically decreasing function of κ_A. In **Fig. 2B**, we see that the model predictions (Eq. **S58**) agree quantitatively with the experiments (Basan et al., 2015).

In fact, the growth rate can be altered by tuning φ_Z and κ_A simultaneously. Then, the relations among the energy fluxes, growth rate and φ_Z still follow Eq. S57 (where φ_Z is a variable). In a 3-D representation, these relations correspond to a surface. In **Fig. 2A**, we show that the model predictions (Eq. **S57**) match well with the experimental data (Basan et al., 2015).

Appendix 3.2 Energy dissipation

In practice, energy dissipation disrupts the proportional relationship between energy demand and biomass production. Thus, Eq. S25 becomes:

$$J_{\mathrm{E}} = r_{\mathrm{E}} \cdot J_{\mathrm{BM}} + w \cdot \frac{M_{\mathrm{carbon}}}{m_0}, \tag{S59}$$

where w represents the dissipation coefficient. In fact, maintenance energy contributes to energy dissipation, and we define the maintenance energy coefficient as w_0. In bacteria, the impact of maintenance energy is roughly negligible, yet in tumor cells, it plays a much more significant role (Locasale and Cantley, 2010).

The introduction of energy dissipation leads to a modification of Eq. S26: combining Eq. S59 and Eq. S16, we have:

$$J_{\mathrm{E}}^{(\mathrm{N})} = \eta_{\mathrm{E}} \cdot \lambda + w\,. \tag{S60}$$

Then, Eq. S29 changes to:

$$\begin{cases} J_r^{(\mathrm{E})} + J_f^{(\mathrm{E})} = \varphi \cdot \lambda + w, \\ \dfrac{J_r^{(\mathrm{E})}}{\varepsilon_r} + \dfrac{J_f^{(\mathrm{E})}}{\varepsilon_f} = \phi_{\max} - \psi \cdot \lambda. \end{cases} \tag{S61}$$

Consequently, if $\varepsilon_r > \varepsilon_f$, the optimal growth strategy for the cell is:

$$\begin{cases} J_f^{(\mathrm{E})} = 0, \\ J_r^{(\mathrm{E})} = \varphi \cdot \lambda + w, \end{cases} \qquad \varepsilon_r > \varepsilon_f, \tag{S62}$$

and if $\varepsilon_f > \varepsilon_r$, the optimal growth strategy is:

$$\begin{cases} J_f^{(\mathrm{E})} = \varphi \cdot \lambda + w, \\ J_r^{(\mathrm{E})} = 0. \end{cases} \qquad \varepsilon_r < \varepsilon_f. \tag{S63}$$

Then, the growth rate becomes a bivariate function of both κ_A and w:

$$\lambda(\kappa_A, w) = \begin{cases} \dfrac{\phi_{\max} - w/\varepsilon_r(\kappa_A)}{\varphi/\varepsilon_r(\kappa_A) + \psi(\kappa_A)} & \varepsilon_r(\kappa_A) > \varepsilon_f(\kappa_A), \\ \dfrac{\phi_{\max} - w/\varepsilon_f(\kappa_A)}{\varphi/\varepsilon_f(\kappa_A) + \psi(\kappa_A)} & \varepsilon_r(\kappa_A) < \varepsilon_f(\kappa_A). \end{cases} \tag{S64}$$

Clearly, $\kappa_A^{(C)}$ is still a constant, while $\lambda_C(w) = \lambda(\kappa_A^{(C)}, w)$ and $\lambda_{max}(w) = \lambda(\kappa_A^{max}, w)$ become functions of w:

$$\begin{cases} \lambda_C(w) = \lambda_C(0)\left\{1 - w\Big/\left[\varepsilon_{r/f}\left(\kappa_A^{(C)}\right)\phi_{max}\right]\right\}, \\ \lambda_{max}(w) = \lambda_{max}(0)\left\{1 - w\Big/\left[\varepsilon_f\left(\kappa_A^{max}\right)\phi_{max}\right]\right\}. \end{cases} \tag{S65}$$

For a cell population, in the homogeneous case, $J_f^{(E)}$ and $J_r^{(E)}$ follow:

$$\begin{cases} J_f^{(E)}(\kappa_A, w) = \left[\varphi \cdot \lambda(\kappa_A, w) + w\right] \cdot \theta\left(\lambda(\kappa_A, w) - \lambda_C(w)\right), \\ J_r^{(E)}(\kappa_A, w) = \left[\varphi \cdot \lambda(\kappa_A, w) + w\right] \cdot \left[1 - \theta\left(\lambda(\kappa_A, w) - \lambda_C(w)\right)\right]. \end{cases} \tag{S66}$$

To compare with experiments, we assume the same extent of extrinsic noise in κ_i^{ext} (and thus κ_i) as that specified in Appendix 2.3. Combining Eqs. S45 and S65, $\lambda_C(w)$ approximately follows a Gaussian distribution:

$$\lambda_C(w) \sim \mathcal{N}\left(\mu_{\lambda_C}(w), \sigma_{\lambda_C}(w)^2\right), \tag{S67}$$

where $\mu_{\lambda C}(w)$ and $\sigma_{\lambda C}(w)$ represent the mean and standard deviation of $\lambda_C(w)$, and

$$\begin{cases} \mu_{\lambda_C}(w) = \mu_{\lambda_C}(0)\left\{1 - w\Big/\left[\varepsilon_{r/f}\left(\kappa_A^{(C)}\right)\phi_{max}\right]\right\}, \\ \sigma_{\lambda_C}(w) \approx \sigma_{\lambda_C}(0)\left\{1 - w\Big/\left[\varepsilon_{r/f}\left(\kappa_A^{(C)}\right)\phi_{max}\right]\right\}. \end{cases} \tag{S68}$$

Here, $\mu_{\lambda C}(0)$, $\sigma_{\lambda C}(0)$, $\lambda_C(0)$, $\lambda_{max}(0)$ and $\lambda(\kappa_A, 0)$ represent parameters or variables unaffected by energy dissipation. In fact, there is a distribution of values for $\varepsilon_{r/f}(\kappa_A^{(C)})$. For approximation, we use the deterministic value of $\varepsilon_{r/f}(\kappa_A^{(C)})$ in Eq. S68, and then the CV of $\lambda_C(w)$ remains largely unperturbed by w. Combining Eqs. S46, S66 and S67, we have:

$$\begin{cases} J_f^{(E)}\left(\lambda(\kappa_A, w), w\right) = \dfrac{1}{2}\left(\varphi \cdot \lambda(\kappa_A, w) + w\right) \cdot \left[\operatorname{erf}\left(\dfrac{\lambda(\kappa_A, w) - \mu_{\lambda_C}(w)}{\sqrt{2}\sigma_{\lambda_C}(w)}\right) + 1\right], \\ J_r^{(E)}\left(\lambda(\kappa_A, w), w\right) = \dfrac{1}{2}\left(\varphi \cdot \lambda(\kappa_A, w) + w\right) \cdot \left[1 - \operatorname{erf}\left(\dfrac{\lambda(\kappa_A, w) - \mu_{\lambda_C}(w)}{\sqrt{2}\sigma_{\lambda_C}(w)}\right)\right]. \end{cases} \tag{S69}$$

Since the dissipation coefficient w is tunable in experiments, for a given value of w, $\lambda(\kappa_A, w)$ changes monotonically with κ_A. Combining Eqs. S68–S69 and S30, we have (here w is a parameter):

$$\begin{cases} J_f^{(\mathrm{N})}(\lambda, w) = \dfrac{\varphi\cdot\lambda + w}{\beta_f^{(A)}}\cdot\left[\operatorname{erf}\left(\dfrac{\lambda-\mu_{\lambda_c}(0)\left\{1-w\Big/\left[\varepsilon_{r/f}\left(\kappa_A^{(\mathrm{C})}\right)\phi_{\max}\right]\right\}}{\sqrt{2}\sigma_{\lambda_c}(0)\left\{1-w\Big/\left[\varepsilon_{r/f}\left(\kappa_A^{(\mathrm{C})}\right)\phi_{\max}\right]\right\}}\right)+1\right], \\ J_r^{(\mathrm{N})}(\lambda, w) = \dfrac{\varphi\cdot\lambda + w}{\beta_r^{(A)}}\cdot\left[1-\operatorname{erf}\left(\dfrac{\lambda-\mu_{\lambda_c}(0)\left\{1-w\Big/\left[\varepsilon_{r/f}\left(\kappa_A^{(\mathrm{C})}\right)\phi_{\max}\right]\right\}}{\sqrt{2}\sigma_{\lambda_c}(0)\left\{1-w\Big/\left[\varepsilon_{r/f}\left(\kappa_A^{(\mathrm{C})}\right)\phi_{\max}\right]\right\}}\right)\right]. \end{cases} \tag{S70}$$

The comparison between model predictions (Eq. S70) and experimental results (Basan et al., 2015) is shown in **Fig. 3B**, which shows quantitative agreement. Meanwhile, the growth rate can also be perturbed by changing κ_A and w simultaneously. The relations among the energy fluxes, growth rate and w follow Eq. **S70** (here w is a variable). In a 3D representation, these relations form a surface. As shown in **Fig. 3A**, the model predictions (Eq. **S70**) agree quantitatively with the experimental results (Basan et al., 2015).

Appendix 3.3 Translation inhibition

In *E. coli*, the translation rate can be modified by adding different concentrations of translation inhibitors, e.g., chloramphenicol (Cm). The net effect of this perturbation is represented as:

$$\kappa_t \xrightarrow{\text{Translation inhibition}} \kappa_t\Big/(\iota+1), \tag{S71}$$

where i stands for the inhibition coefficient with $\iota > 0$, and $(1+\iota)^{-1}$ represents the translation efficiency. Thus, Eq. S32 changes to:

$$\psi(\kappa_A,\iota) = \frac{\iota+1}{\kappa_t} + \frac{1+\eta_{a1}+\eta_c}{2\kappa_A} + \frac{\eta_{a2}+\eta_b+2\eta_e+\eta_d}{2\kappa_1} + \frac{\eta_b+\eta_c}{\kappa_2} + \frac{\eta_c}{\kappa_3} + \frac{\eta_c+\eta_d}{\kappa_5} + \sum_i^{a1,a2,b,c,d}\frac{\eta_i}{\kappa_i}. \tag{S72}$$

First, we consider the case where maintenance energy is neglected, i.e., $w_0 = 0$. In this case, the growth rate takes the following form:

$$\lambda(\kappa_A,\iota) = \begin{cases} \dfrac{\phi_{\max}}{\varphi/\varepsilon_r(\kappa_A)+\psi(\kappa_A,\iota)} & \varepsilon_r(\kappa_A) > \varepsilon_f(\kappa_A), \\ \dfrac{\phi_{\max}}{\varphi/\varepsilon_f(\kappa_A)+\psi(\kappa_A,\iota)} & \varepsilon_r(\kappa_A) < \varepsilon_f(\kappa_A), \end{cases} \tag{S73}$$

where $\lambda(\kappa_A, 0)$ and $\psi(\kappa_A, 0)$ represent the terms unaffected by translation inhibition. Thus, $\lambda_C(\iota) \equiv \lambda(\kappa_A^{(C)}, \iota)$ and $\lambda_{max}(\iota) \equiv \lambda(\kappa_A^{max}, \iota)$ become functions of ι:

$$\begin{cases} \lambda_C(\iota) = \lambda_C(0)\dfrac{\varphi/\varepsilon_{r/f}\left(\kappa_A^{(C)}\right)+\psi\left(\kappa_A^{(C)},0\right)}{\varphi/\varepsilon_{r/f}\left(\kappa_A^{(C)}\right)+\psi\left(\kappa_A^{(C)},\iota\right)}, \\ \lambda_{max}(\iota) = \lambda_{max}(0)\dfrac{\varphi/\varepsilon_{f}\left(\kappa_A^{max}\right)+\psi\left(\kappa_A^{max},0\right)}{\varphi/\varepsilon_{f}\left(\kappa_A^{max}\right)+\psi\left(\kappa_A^{max},\iota\right)}. \end{cases} \tag{S74}$$

In the homogeneous case, $J_f^{(E)}$ and $J_r^{(E)}$ follow:

$$\begin{cases} J_f^{(E)}(\kappa_A,\iota) = \varphi\cdot\lambda(\kappa_A,\iota)\cdot\theta\left(\lambda(\kappa_A,\iota)-\lambda_C(\iota)\right), \\ J_r^{(E)}(\kappa_A,\iota) = \varphi\cdot\lambda(\kappa_A,\iota)\cdot\left[1-\theta\left(\lambda(\kappa_A,\iota)-\lambda_C(\iota)\right)\right]. \end{cases} \tag{S75}$$

To compare with experiments, we assume that extrinsic noise exists in k_i^{ext} and κ_i as specified in Appendix 2.3. Combining Eqs. S45 and S74, $\lambda_C(\iota)$ can be approximated by a Gaussian distribution:

$$\lambda_C(\iota) \sim \mathcal{N}\left(\mu_{\lambda_C}(\iota), \sigma_{\lambda_C}(\iota)^2\right), \tag{S76}$$

where $\mu_{\lambda C}(\iota)$ and $\sigma_{\lambda C}(\iota)$ represent the mean and standard deviation of $\lambda_C(\iota)$, with

$$\begin{cases} \mu_{\lambda_C}(\iota) = \mu_{\lambda_C}(0)\dfrac{\varphi/\varepsilon_{r/f}\left(\kappa_A^{(C)}\right)+\psi\left(\kappa_A^{(C)},0\right)}{\varphi/\varepsilon_{r/f}\left(\kappa_A^{(C)}\right)+\psi\left(\kappa_A^{(C)},\iota\right)}, \\ \sigma_{\lambda_C}(\iota) \approx \sigma_{\lambda_C}(0)\dfrac{\varphi/\varepsilon_{r/f}\left(\kappa_A^{(C)}\right)+\psi\left(\kappa_A^{(C)},0\right)}{\varphi/\varepsilon_{r/f}\left(\kappa_A^{(C)}\right)+\psi\left(\kappa_A^{(C)},\iota\right)}. \end{cases} \tag{S77}$$

Here, $\mu_{\lambda C}(0)$, $\sigma_{\lambda C}(0)$, $\psi(\kappa_A^{(C)}, 0)$, $\lambda_C(0)$ and $\lambda_{max}(0)$ stand for the terms unaffected by translation inhibition. Essentially, there are distributions of values for $\varepsilon_{r/f}(\kappa_A^{(C)})$, $\psi(\kappa_A^{(C)}, 0)$ and $\psi(\kappa_A^{(C)}, \iota)$. For approximation, we use the deterministic values of these terms in Eq. S77, and then the CV of $\lambda_C(\iota)$ can be approximated by $\lambda_C(0)$. Combining Eqs. S46, S75 and S76, we have:

$$\begin{cases} J_f^{(E)}\left(\lambda(\kappa_A,\iota),\iota\right) = \dfrac{1}{2}\varphi\cdot\lambda(\kappa_A,\iota)\cdot\left[\operatorname{erf}\left(\dfrac{\lambda(\kappa_A,\iota)-\mu_{\lambda_C}(\iota)}{\sqrt{2}\sigma_{\lambda_C}(\iota)}\right)+1\right], \\ J_r^{(E)}\left(\lambda(\kappa_A,\iota),\iota\right) = \dfrac{1}{2}\varphi\cdot\lambda(\kappa_A,\iota)\cdot\left[1-\operatorname{erf}\left(\dfrac{\lambda(\kappa_A,\iota)-\mu_{\lambda_C}(\iota)}{\sqrt{2}\sigma_{\lambda_C}(\iota)}\right)\right]. \end{cases} \tag{S78}$$

In the experiments, the inhibition coefficient ι is controllable by adjusting the concentration of the translation inhibitor. For a given value of ι, $\lambda(\kappa_A, \iota)$ changes monotonically with κ_A. Combining Eqs. S30 and S78, we have (here i is a parameter):

$$\begin{cases} J_f^{(\mathrm{N})}(\lambda,\iota)=\dfrac{\varphi\cdot\lambda}{\beta_f^{(A)}}\cdot\left[\operatorname{erf}\left(\dfrac{\lambda-\mu_{\lambda_\mathrm{C}}(\iota)}{\sqrt{2}\sigma_{\lambda_\mathrm{C}}(\iota)}\right)+1\right], \\ J_r^{(\mathrm{N})}(\lambda,\iota)=\dfrac{\varphi\cdot\lambda}{\beta_r^{(A)}}\cdot\left[1-\operatorname{erf}\left(\dfrac{\lambda-\mu_{\lambda_\mathrm{C}}(\iota)}{\sqrt{2}\sigma_{\lambda_\mathrm{C}}(\iota)}\right)\right], \end{cases} \tag{S79}$$

where $\mu_{\lambda\mathrm{C}}(\iota)$ and $\sigma_{\lambda\mathrm{C}}(\iota)$ follow Eq. S77. The growth rate can also be perturbed by altering both κ_A and ι simultaneously. In this case, the relations among the energy fluxes, growth rate and ι still follow Eq. S79 (here ι is a variable). The comparison between Eq. S79 and experimental data (Basan et al., 2015) is shown in **Appendix-fig. 2D (3-D) and 2E (2-D)**. Overall, there is good consistency; however, there remains a noticeable discrepancy when ι is large (i.e., at high concentration of the translation inhibitor). This led us to consider the maintenance energy through the coefficient w_0, which is small but may account for this discrepancy. Then, $\lambda(\kappa_A, \iota)$ changes into:

$$\lambda(\kappa_A,\iota)=\begin{cases} \dfrac{\phi_{\max}-w_0/\varepsilon_r(\kappa_A)}{\varphi/\varepsilon_r(\kappa_A)+\psi(\kappa_A,\iota)} & \varepsilon_r(\kappa_A)>\varepsilon_f(\kappa_A), \\ \dfrac{\phi_{\max}-w_0/\varepsilon_f(\kappa_A)}{\varphi/\varepsilon_f(\kappa_A)+\psi(\kappa_A,\iota)} & \varepsilon_r(\kappa_A)<\varepsilon_f(\kappa_A), \end{cases} \tag{S80}$$

while $\lambda_\mathrm{C}(\iota) \equiv \lambda(\kappa_A^{(\mathrm{C})}, \iota)$ and $\lambda_{\max}(\iota) \equiv \lambda(\kappa_A^{\max}, \iota)$ still follow Eq. **S74**, though the forms of $\lambda_\mathrm{C}(0)$ and $\lambda_{\max}(0)$ change to:

$$\begin{cases} \lambda_\mathrm{C}(0)=\dfrac{\phi_{\max}-w_0/\varepsilon_{r/f}\left(\kappa_A^{(\mathrm{C})}\right)}{\varphi/\varepsilon_{r/f}\left(\kappa_A^{(\mathrm{C})}\right)+\psi\left(\kappa_A^{(\mathrm{C})},0\right)}, \\ \lambda_{\max}(0)=\dfrac{\phi_{\max}-w_0/\varepsilon_f\left(\kappa_A^{\max}\right)}{\varphi/\varepsilon_f\left(\kappa_A^{\max}\right)+\psi\left(\kappa_A^{\max},0\right)}. \end{cases} \tag{S81}$$

In the homogeneous case, $J_f^{(\mathrm{E})}$ and $J_r^{(\mathrm{E})}$ follow:

$$\begin{cases} J_f^{(\mathrm{E})}(\kappa_A,\iota)=\left[\varphi\cdot\lambda(\kappa_A,\iota)+w_0\right]\cdot\theta\left(\lambda(\kappa_A,\iota)-\lambda_\mathrm{C}(\iota)\right), \\ J_r^{(\mathrm{E})}(\kappa_A,\iota)=\left[\varphi\cdot\lambda(\kappa_A,\iota)+w_0\right]\cdot\left[1-\theta\left(\lambda(\kappa_A,\iota)-\lambda_\mathrm{C}(\iota)\right)\right]. \end{cases} \tag{S82}$$

To compare with experiments, we assume that the extrinsic noise follows the specification in **Appendix 2.3**. Combining Eqs. **S45**, **S74** and **S81**, $\lambda_\mathrm{C}(\iota)$ approximately follows a Gaussian distribution:

$$\lambda_\mathrm{C}(\iota)\sim\mathcal{N}\left(\mu_{\lambda_\mathrm{C}}(\iota),\sigma_{\lambda_\mathrm{C}}(\iota)^2\right). \tag{S83}$$

Here $\mu_{\lambda C}(\iota)$ and $\sigma_{\lambda C}(\iota)$ still follow Eq. **S77**, while $\mu_{\lambda C}(0)$ and $\sigma_{\lambda C}(0)$ change accordingly with $\lambda_C(0)$ (see Eq. **S81**). For approximation, we use the deterministic values of the relevant terms in Eq. **S77**, and then the CV of $\lambda_C(\iota)$ is roughly the same as $\lambda_C(0)$. Combining Eqs. **S46**, **S82** and **S83**, we have:

$$\begin{cases} J_f^{(E)}\left(\lambda\left(\kappa_A,\iota\right),\iota\right)=\frac{1}{2}\left(\varphi\cdot\lambda\left(\kappa_A,\iota\right)+w_0\right)\cdot\left[\operatorname{erf}\left(\frac{\lambda\left(\kappa_A,\iota\right)-\mu_{\lambda_C}\left(\iota\right)}{\sqrt{2}\sigma_{\lambda_C}\left(\iota\right)}\right)+1\right], \\ J_r^{(E)}\left(\lambda\left(\kappa_A,\iota\right),\iota\right)=\frac{1}{2}\left(\varphi\cdot\lambda\left(\kappa_A,\iota\right)+w_0\right)\cdot\left[1-\operatorname{erf}\left(\frac{\lambda\left(\kappa_A,\iota\right)-\mu_{\lambda_C}\left(\iota\right)}{\sqrt{2}\sigma_{\lambda_C}\left(\iota\right)}\right)\right]. \end{cases} \tag{S84}$$

Thus, for a given ι, $\lambda(\kappa_A, \iota)$ changes monotonically with κ_A. Combining Eqs. **S30** and **S84**, we have (here ι is a parameter):

$$\begin{cases} J_f^{(N)}\left(\lambda,\iota\right)=\frac{\varphi\cdot\lambda+w_0}{\beta_f^{(A)}}\cdot\left[\operatorname{erf}\left(\frac{\lambda-\mu_{\lambda_C}\left(\iota\right)}{\sqrt{2}\sigma_{\lambda_C}\left(\iota\right)}\right)+1\right]. \\ J_r^{(N)}\left(\lambda,\iota\right)=\frac{\varphi\cdot\lambda+w_0}{\beta_r^{(A)}}\cdot\left[1-\operatorname{erf}\left(\frac{\lambda-\mu_{\lambda_C}\left(\iota\right)}{\sqrt{2}\sigma_{\lambda_C}\left(\iota\right)}\right)\right]. \end{cases} \tag{S85}$$

The growth rate and fluxes can also be perturbed by altering both κ_A and ι simultaneously. The relations among the energy fluxes, growth rate and ι would still follow Eq. **S85**, except that ι is now regarded as a variable. Assuming a small amount of maintenance energy by assigning w_0 = 2.5 (h^{-1}), we find that the experimental results (Basan et al., 2015) agree quantitatively well with the model predictions (**Fig. 3C-D**).

Appendix 4 Overflow metabolism in substrates other than Group A carbon sources

Due to the topology of the metabolic network, for cells using Group A carbon sources, the behavior of overflow metabolism follows Eq. **5** (or Eq. **S47**) upon $\kappa_A$perturbation (i.e., varying the type or concentration of a Group A carbon source). This has been demonstrated clearly in the above analysis and agrees quantitatively with experiments. However, further analysis is required for cells using substrates other than Group A sources due to the topological differences in carbon utilization (Wang et al., 2019). In principle, substrates entering from glycolysis or the points before acetyl-CoA are potentially involved in overflow metabolism, while those joining from the TCA cycle are not relevant to this behavior. Still, mixed carbon sources are likely to induce a different profile of overflow metabolism, as long as there is a carbon source derived from glycolysis.

Appendix 4.1 Pyruvate

The coarse-grained model for pyruvate utilization is shown in **Fig. 3E**. Here, nodes M_1, M_2, M_3, M_4, M_5 follow the descriptions in **Appendix 2.1**. Each biochemical reaction follows Eq. **S5** with $b_i = 1$ except that $2M_2 \to M_1$ and $M_3 + M_5 \to M_4$. By applying flux balance to the stoichiometric fluxes, combining with Eq. **S8**, we have:

$$\begin{cases} \Phi_{\mathrm{py}} \cdot \xi_{\mathrm{py}} = \Phi_7 \cdot \xi_7 + \Phi_8 \cdot \xi_8, \\ \Phi_7 \cdot \xi_7 = 2\Phi_9 \cdot \xi_9 + \Phi_5 \cdot \xi_5 + \Phi_{a2} \cdot \xi_{a2}, \\ \Phi_9 \cdot \xi_9 = \Phi_{a1} \cdot \xi_{a1}, \\ \Phi_8 \cdot \xi_8 = \Phi_3 \cdot \xi_3 + \Phi_6 \cdot \xi_6 + \Phi_b \cdot \xi_b, \\ \Phi_5 \cdot \xi_5 + \Phi_4 \cdot \xi_4 = \Phi_3 \cdot \xi_3 + \Phi_d \cdot \xi_d, \\ \Phi_3 \cdot \xi_3 = \Phi_4 \cdot \xi_4 + \Phi_c \cdot \xi_c. \end{cases} \tag{S86}$$

For energy biogenesis, we convert all the energy currencies into ATPs, and then,

$$\beta_8 \cdot \Phi_8 \cdot \xi_8 + \beta_3 \cdot \Phi_3 \cdot \xi_3 + \beta_4 \cdot \Phi_4 \cdot \xi_4 + \beta_6 \cdot \Phi_6 \cdot \xi_6 + \beta_{a1} \cdot \Phi_{a1} \cdot \xi_{a1} - \beta_7 \cdot \Phi_7 \cdot \xi_7 - \beta_9 \cdot \Phi_9 \cdot \xi_9 = J_{\mathrm{E}}, \tag{S87}$$

where $\beta_7 = 1$, $\beta_8 = 2$, $\beta_3 = 2$, $\beta_4 = 6$, $\beta_6 = 1$, $\beta_9 = 6$, $\beta_1 = 4$ for *E. coli* (Neidhardt et al., 1990; Sauer et al., 2004), and J_{E} follows Eq. S25. By applying the substitutions specified in Eqs. S9, S12, S14–S18, combined with Eqs. S4, S10, S22, S23, S25, S86–S87, and the constraint of proteome resource allocation, we have:

$$\begin{cases} \phi_{\mathrm{py}} \cdot \kappa_{\mathrm{py}} = \phi_7 \cdot \kappa_7 + \phi_8 \cdot \kappa_8, \\ \phi_7 \cdot \kappa_7 = 2\phi_9 \cdot \kappa_9 + \phi_5 \cdot \kappa_5 + \phi_{a2} \cdot \kappa_{a2}, \\ \phi_9 \cdot \kappa_9 = \phi_{a1} \cdot \kappa_{a1} \\ \phi_8 \cdot \kappa_8 = \phi_3 \cdot \kappa_3 + \phi_6 \cdot \kappa_6 + \phi_b \cdot \kappa_b \\ \phi_3 \cdot \kappa_3 = \phi_4 \cdot \kappa_4 + \phi_c \cdot \kappa_c \\ \phi_5 \cdot \kappa_5 + \phi_4 \cdot \kappa_4 = \phi_3 \cdot \kappa_3 + \phi_d \cdot \kappa_d \\ \phi_{a1} \cdot \kappa_{a1} = \eta_{a1} \cdot \lambda, \phi_{a2} \cdot \kappa_{a2} = \eta_{a2} \cdot \lambda, \phi_b \cdot \kappa_b = \eta_b \cdot \lambda, \phi_c \cdot \kappa_c = \eta_c \cdot \lambda, \phi_d \cdot \kappa_d = \eta_d \cdot \lambda, \\ \beta_8 \cdot \phi_8 \cdot \kappa_8 + \beta_3 \cdot \phi_3 \cdot \kappa_3 + \beta_4 \cdot \phi_4 \cdot \kappa_4 + \beta_6 \cdot \phi_6 \cdot \kappa_6 + \beta_{a1} \cdot \phi_{a1} \cdot \kappa_{a1} - \beta_7 \cdot \phi_7 \cdot \kappa_7 - \beta_9 \cdot \phi_9 \cdot \kappa_9 = J_{\mathrm{E}}^{(\mathrm{N})}, \\ J_{\mathrm{E}}^{(\mathrm{N})} = \eta_{\mathrm{E}} \cdot \lambda, \lambda = \phi_R \cdot \kappa_t, J_r^{(\mathrm{N})} = \phi_4 \cdot \kappa_4, J_f^{(\mathrm{N})} = \phi_6 \cdot \kappa_6, \\ \phi_{\mathrm{R}} + \phi_{\mathrm{py}} + \phi_3 + \phi_4 + \phi_5 + \phi_6 + \phi_7 + \phi_8 + \phi_9 + \phi_{a1} + \phi_{a2} + \phi_b + \phi_c + \phi_d = \phi_{\max}, \end{cases} \tag{S88}$$

where $\eta_{\mathrm{E}}=r_{\mathrm{E}}\cdot\left[\sum_i r_i/N_{\mathrm{EP}_i}^{\mathrm{carbon}}\right]^{-1}$. κ_i is approximately a constant which follows Eq. S20 for each of the intermediate node. The substrate quality of κ_{py} varies with the external concentration of pyruvate ([py]),

$$\kappa_{\mathrm{py}}\equiv\frac{r_{\mathrm{protein}}}{r_{\mathrm{carbon}}}\cdot\frac{k_{\mathrm{py}}^{\mathrm{cat}}}{m_{E_{\mathrm{py}}}}\cdot\frac{[\mathrm{py}]}{[\mathrm{py}]+K_{\mathrm{py}}}\cdot m_0\,. \tag{S89}$$

From Eq. S88, all φ_i can be expressed by $J_r^{(\mathrm{N})}$, $J_f^{(\mathrm{N})}$, and *2*:

$$\begin{cases}\phi_{\mathrm{py}}=\left[\left(2\eta_{a1}+\eta_{a2}+\eta_b+2\eta_c+\eta_d\right)\lambda+J_r^{(\mathrm{N})}+J_f^{(\mathrm{N})}\right]\Big/\kappa_{\mathrm{py}}\,,\\ \phi_7=\left(2\eta_{a1}+\eta_{a2}+\eta_c+\eta_d\right)\lambda/\kappa_7\,,\phi_9=\eta_{a1}\cdot\lambda/\kappa_9\\ \phi_8=\left[J_r^{(\mathrm{N})}+J_f^{(\mathrm{N})}+\left(\eta_b+\eta_c\right)\lambda\right]\Big/\kappa_8\\ \phi_3=\left(J_r^{(\mathrm{N})}+\eta_c\cdot\lambda\right)\Big/\kappa_3\,,\phi_4=J_r^{(\mathrm{N})}/\kappa_4\,,\\ \phi_5=\left(\eta_c+\eta_d\right)\lambda/\kappa_5\,,\phi_6=J_f^{(\mathrm{N})}/\kappa_6\,,\\ \phi_i=\eta_i\cdot\lambda/\kappa_i\ \ \left(i=a1,\ a2,\ b,\ c,\ d\right).\end{cases} \tag{S90}$$

By substituting Eq. S90 into Eq. S88, we have:

$$\begin{cases}J_r^{(\mathrm{E,py})}+J_f^{(\mathrm{E,py})}=\varphi_{\mathrm{py}}\cdot\lambda,\\ \dfrac{J_r^{(\mathrm{E,py})}}{\varepsilon_r^{(\mathrm{py})}}+\dfrac{J_f^{(\mathrm{E,py})}}{\varepsilon_f^{(\mathrm{py})}}=\phi_{\max}-\psi_{\mathrm{py}}\cdot\lambda.\end{cases} \tag{S91}$$

Here, $J_r^{(\mathrm{E,py})}$ and $J_f^{(\mathrm{E,py})}$ stand for the normalized energy fluxes of respiration and fermentation, respectively, with

$$\begin{cases}J_r^{(\mathrm{E,py})}=\beta_r^{(\mathrm{py})}\cdot J_r^{(\mathrm{N})},\\ J_f^{(\mathrm{E,py})}=\beta_f^{(\mathrm{py})}\cdot J_f^{(\mathrm{N})}.\end{cases} \tag{S92}$$

where $\beta_r^{(\mathrm{py})}=\beta_3+\beta_4+\beta_8$ and $\beta_f^{(\mathrm{py})}=\beta_6+\beta_8$, with $\beta_r^{(\mathrm{py})}=10$ and $\beta_f^{(\mathrm{py})}=3$ for *E. coli*. The coefficients $\varepsilon_r^{(\mathrm{py})}$ and $\varepsilon_f^{(\mathrm{py})}$ represent the proteome efficiencies for energy biogenesis using pyruvate in respiration and fermentation pathways, respectively, with

$$\begin{cases}\varepsilon_r^{(\mathrm{py})}=\dfrac{\beta_r^{(\mathrm{py})}}{1/\kappa_{\mathrm{py}}+1/\kappa_8+1/\kappa_3+1/\kappa_4},\\ \varepsilon_f^{(\mathrm{py})}=\dfrac{\beta_f^{(\mathrm{py})}}{1/\kappa_{\mathrm{py}}+1/\kappa_8+1/\kappa_6}.\end{cases} \tag{S93}$$

ψ_{py}^{-1} is the proteome efficiency for biomass generation using pyruvate in the biomass synthesis pathway, with

$$\psi_{\mathrm{py}}=\frac{1}{\kappa_t}+\frac{1+\eta_{a1}+\eta_c}{\kappa_{\mathrm{py}}}+\frac{1-\eta_b+\eta_{a1}}{\kappa_7}+\frac{\eta_b+\eta_c}{\kappa_8}+\frac{\eta_{a1}}{\kappa_9}+\frac{\eta_c}{\kappa_3}+\frac{\eta_c+\eta_d}{\kappa_5}+\sum_i^{a1,a2,b,c,d}\frac{\eta_i}{\kappa_i}. \tag{S94}$$

ϕ_{py} is an energy demand coefficient (a constant), with

$$\varphi_{\mathrm{py}}\equiv\eta_{\mathrm{E}}+\beta_7\cdot\left(1-\eta_b+\eta_{a1}\right)+\beta_9\cdot\eta_{a1}-\beta_8\cdot\left(\eta_c+\eta_b\right)-\beta_3\cdot\eta_c-\beta_{a1}\cdot\eta_{a1}, \tag{S95}$$

Evidently, Eq. S91 is identical in form with Eq. S29. The growth rate changes into κ_{py} dependent:

$$\lambda\left(\kappa_{\mathrm{py}}\right)=\begin{cases}\dfrac{\phi_{\max}}{\varphi_{\mathrm{py}}/\varepsilon_r^{(\mathrm{py})}\left(\kappa_{\mathrm{py}}\right)+\psi_{\mathrm{py}}\left(\kappa_{\mathrm{py}}\right)} & \varepsilon_r^{(\mathrm{py})}\left(\kappa_{\mathrm{py}}\right)>\varepsilon_f^{(\mathrm{py})}\left(\kappa_{\mathrm{py}}\right),\\ \dfrac{\phi_{\max}}{\varphi_{\mathrm{py}}/\varepsilon_f^{(\mathrm{py})}\left(\kappa_{\mathrm{py}}\right)+\psi_{\mathrm{py}}\left(\kappa_{\mathrm{py}}\right)} & \varepsilon_r^{(\mathrm{py})}\left(\kappa_{\mathrm{py}}\right)<\varepsilon_f^{(\mathrm{py})}\left(\kappa_{\mathrm{py}}\right).\end{cases} \tag{S96}$$

When κ_{py} is very small, combined with Eq. S93, then,

$$\begin{cases}\varepsilon_r^{(\mathrm{py})}\left(\kappa_{\mathrm{py}}\to 0\right)\approx\beta_r^{(\mathrm{py})}\cdot\kappa_{\mathrm{py}},\\ \varepsilon_f^{(\mathrm{py})}\left(\kappa_{\mathrm{py}}\to 0\right)\approx\beta_f^{(\mathrm{py})}\cdot\kappa_{\mathrm{py}}.\end{cases} \tag{S97}$$

Obviously, $\beta_r^{(py)}\gg\beta_f^{(py)}$, and hence

$$\varepsilon_r^{(\mathrm{py})}\left(\kappa_{\mathrm{py}}\to 0\right)>\varepsilon_f^{(\mathrm{py})}\left(\kappa_{\mathrm{py}}\to 0\right). \tag{S98}$$

As long as

$$\frac{\beta_r^{(\mathrm{py})}-\beta_f^{(\mathrm{py})}}{\kappa_{\mathrm{py}}^{(\mathrm{ST})}}<\beta_f^{(\mathrm{py})}\left(\frac{1}{\kappa_8}+\frac{1}{\kappa_3}+\frac{1}{\kappa_4}\right)-\beta_r^{(\mathrm{py})}\cdot\left(\frac{1}{\kappa_8}+\frac{1}{\kappa_6}\right), \tag{S99}$$

where the superscript "(ST)" stands for the saturated concentration, then,

$$\varepsilon_r^{(\mathrm{py})}\left(\kappa_{\mathrm{py}}^{(\mathrm{ST})}\right)<\varepsilon_f^{(\mathrm{py})}\left(\kappa_{\mathrm{py}}^{(\mathrm{ST})}\right), \tag{S100}$$

and there exists a critical value of φ_{py}, denoted as $\kappa_{py}^{(C)}$, with

$$\begin{cases}\varepsilon_r^{(\mathrm{py})}\left(\kappa_{\mathrm{py}}^{(\mathrm{C})}\right)=\varepsilon_f^{(\mathrm{py})}\left(\kappa_{\mathrm{py}}^{(\mathrm{C})}\right)=\dfrac{\beta_r^{(\mathrm{py})}-\beta_f^{(\mathrm{py})}}{1/\kappa_3+1/\kappa_4-1/\kappa_6}=\dfrac{\beta_3+\beta_4-\beta_6}{1/\kappa_3+1/\kappa_4-1/\kappa_6},\\ \lambda_{\mathrm{C}}^{(\mathrm{py})}\equiv\lambda\left(\kappa_{\mathrm{py}}^{(\mathrm{C})}\right)=\dfrac{\phi_{\max}}{\varphi_{\mathrm{py}}/\varepsilon_{r/f}^{(\mathrm{py})}\left(\kappa_{\mathrm{py}}^{(\mathrm{C})}\right)+\psi_{\mathrm{py}}\left(\kappa_{\mathrm{py}}^{(\mathrm{C})}\right)}.\end{cases} \tag{S101}$$

Here, $\lambda_C^{(py)}$ is the growth rate at the transition point, and $\varepsilon_{r,f}^{(py)}$ stands for either $\varepsilon_r^{(py)}$ or $\varepsilon_f^{(py)}$. In **Appendix-fig. 2H**, we show the dependencies of $\varepsilon_r^{(py)}(\kappa_{py})$, $\varepsilon_f^{(py)}(\kappa_{py})$ and $\lambda(\kappa_{py})$ on κ_{py} in a 3dimensional form. In the homogeneous case, $J_f^{(E,py)}$ and $J_r^{(E,py)}$ follow:

$$\begin{cases} J_f^{(\mathrm{E,py})} = \varphi_{\mathrm{py}} \cdot \lambda \cdot \theta\left(\lambda - \lambda_{\mathrm{C}}^{(\mathrm{py})}\right), \\ J_r^{(\mathrm{E,py})} = \varphi_{\mathrm{py}} \cdot \lambda \cdot \left[1 - \theta\left(\lambda - \lambda_{\mathrm{C}}^{(\mathrm{py})}\right)\right]. \end{cases} \tag{S102}$$

Defining $\lambda_{\max}^{(py)} = \lambda\left(\kappa_{py}^{(ST)}\right)$, and then, [0, $\lambda_{\max}^{(py)}$] is the relevant range of the *x* axis. To compare with experiments, we assume the same extent of extrinsic noise in k_i^{on} as specified in **Appendix 2.3**. Then, $\lambda_C^{(py)}$ approximately follows a Gaussian distribution:

$$\lambda_{\mathrm{C}}^{(\mathrm{py})} \sim \mathcal{N}\left(\mu_{\lambda_{\mathrm{C}}^{(\mathrm{py})}}, \sigma^2_{\lambda_{\mathrm{C}}^{(\mathrm{py})}}\right), \tag{S103}$$

where $\mu_{\lambda_C^{(py)}}$ and $\sigma_{\lambda_C^{(py)}}$ stand for the mean and standard deviation of $\lambda_C^{(py)}$. Then, the relations between the normalized energy fluxes and growth rate are:

$$\begin{cases} J_f^{(\mathrm{E,py})}(\lambda) = \dfrac{1}{2}\varphi_{\mathrm{py}} \cdot \lambda \cdot \left[\mathrm{erf}\left(\dfrac{\lambda - \mu_{\lambda_{\mathrm{C}}^{(\mathrm{py})}}}{\sqrt{2}\sigma_{\lambda_{\mathrm{C}}^{(\mathrm{py})}}}\right) + 1\right], \\ J_r^{(\mathrm{E,py})}(\lambda) = \dfrac{1}{2}\varphi_{\mathrm{py}} \cdot \lambda \cdot \left[1 - \mathrm{erf}\left(\dfrac{\lambda - \mu_{\lambda_{\mathrm{C}}^{(\mathrm{py})}}}{\sqrt{2}\sigma_{\lambda_{\mathrm{C}}^{(\mathrm{py})}}}\right)\right]. \end{cases} \tag{S104}$$

Combined with Eq. **S92**, we have:

$$\begin{cases} J_f^{(\mathrm{N})}(\lambda) = \dfrac{\varphi_{\mathrm{py}}}{2\beta_f^{(\mathrm{py})}} \cdot \lambda \cdot \left[\mathrm{erf}\left(\dfrac{\lambda - \mu_{\lambda_{\mathrm{C}}^{(\mathrm{py})}}}{\sqrt{2}\sigma_{\lambda_{\mathrm{C}}^{(\mathrm{py})}}}\right) + 1\right], \\ J_r^{(\mathrm{N})}(\lambda) = \dfrac{\varphi_{\mathrm{py}}}{2\beta_r^{(\mathrm{py})}} \cdot \lambda \cdot \left[1 - \mathrm{erf}\left(\dfrac{\lambda - \mu_{\lambda_{\mathrm{C}}^{(\mathrm{py})}}}{\sqrt{2}\sigma_{\lambda_{\mathrm{C}}^{(\mathrm{py})}}}\right)\right]. \end{cases} \tag{S105}$$

In **Fig. 3F**, we show that the model predictions (Eq. **S105**) align quantitatively with the experimental results (Holms, 1996).

Appendix 4.2 Mixture of a Group A carbon source with extracellular amino acids

In the case of a Group A carbon source mixed with amino acids, the coarse-grained model is shown in **Appendix-fig. 2A**. This model can be used to analyze mixtures with one or multiple types of extracellular amino acids. Here, Eqs. **S21**, **S22**, **S24** and **S25** still apply, but Eq. **S23** changes to (the case of i= $a1$ remains the same as Eq. **S23**):

$$\Phi_i \cdot \xi_i \cdot N_{\mathrm{EP}_i}^{\mathrm{carbon}} + \Phi_i' \cdot \xi_i' \cdot N_{\mathrm{P}_i}^{\mathrm{carbon}} = r_i \cdot J_{\mathrm{BM}} \left(i = a2,\ b,\ c,\ d\right). \tag{S106}$$

Here, $N_{\mathrm{P}_i}^{\mathrm{carbon}}$ represents the number of carbon atoms in a molecule of Pool i. For simplicity, we assume:

$$N_{\mathrm{P}_i}^{\mathrm{carbon}} \approx N_{\mathrm{EP}_i}^{\mathrm{carbon}}. \tag{S107}$$

In the case where all 21 types of amino acids are present and each is at saturated concentration (denoted as “21AA”), we have:

$$\begin{cases} \phi_A \cdot \kappa_A = \phi_1 \cdot \kappa_1 + \phi_{a1} \cdot \kappa_{a1}, \\ 2\phi_1 \cdot \kappa_1 = \phi_2 \cdot \kappa_2 + \phi_5 \cdot \kappa_5 + \phi_{a2} \cdot \kappa_{a2}, \\ \phi_2 \cdot \kappa_2 = \phi_3 \cdot \kappa_3 + \phi_6 \cdot \kappa_6 + \phi_b \cdot \kappa_b, \\ \phi_5 \cdot \kappa_5 + \phi_4 \cdot \kappa_4 = \phi_3 \cdot \kappa_3 + \phi_d \cdot \kappa_d, \\ \phi_3 \cdot \kappa_3 = \phi_4 \cdot \kappa_4 + \phi_c \cdot \kappa_c, \\ \phi_{a1} \cdot \kappa_{a1} = \eta_{a1} \cdot \lambda, \phi_{a2} \cdot \kappa_{a2} + \phi_{a2}^{(21\mathrm{AA})} \cdot \kappa_{a2}^{(21\mathrm{AA})} = \eta_{a2} \cdot \lambda, \phi_b \cdot \kappa_b + \phi_b^{(21\mathrm{AA})} \cdot \kappa_b^{(21\mathrm{AA})} = \eta_b \cdot \lambda, \\ \phi_c \cdot \kappa_c + \phi_c^{(21\mathrm{AA})} \cdot \kappa_c^{(21\mathrm{AA})} = \eta_c \cdot \lambda, \phi_d \cdot \kappa_d + \phi_d^{(21\mathrm{AA})} \cdot \kappa_d^{(21\mathrm{AA})} = \eta_d \cdot \lambda, \\ \beta_1 \cdot \phi_1 \cdot \kappa_1 + \beta_2 \cdot \phi_2 \cdot \kappa_2 + \beta_3 \cdot \phi_3 \cdot \kappa_3 + \beta_4 \cdot \phi_4 \cdot \kappa_4 + \beta_6 \cdot \phi_6 \cdot \kappa_6 + \beta_{a1} \cdot \phi_{a1} \cdot \kappa_{a1} = J_{\mathrm{E}}^{(\mathrm{N})}, \\ J_{\mathrm{E}}^{(\mathrm{N})} = \eta_{\mathrm{E}} \cdot \lambda, \lambda = \phi_R \cdot \kappa_t, J_r^{(\mathrm{N})} = \phi_4 \cdot \kappa_4, J_f^{(\mathrm{N})} = \phi_6 \cdot \kappa_6, \\ \phi_{\mathrm{R}} + \phi_A + \sum_i^6 \phi_i + \sum_j^{a1,a2,b,c,d} \phi_j + \phi_{a2}^{(21\mathrm{AA})} + \phi_b^{(21\mathrm{AA})} + \phi_c^{(21\mathrm{AA})} + \phi_d^{(21\mathrm{AA})} = \phi_{\max}, \end{cases} \tag{S108}$$

where φ_i and κ_i are defined following Eqs. **S9** and **S12**. Since the cell growth rate significantly increases with the mixture of amino acids, we deduce that Pools a2-d are supplied by amino acids in growth optimization, with

$$\phi_i = 0 \left(i = a2,\ b,\ c,\ d\right). \tag{S109}$$

Amino acids should be more efficient in the supply of biomass synthesis than the Group A carbon source for Pools a2-d, i.e.,

$$\begin{cases} 1/\kappa_{a2}^{(21\mathrm{AA})} < 1/\kappa_{a2} + 1/\left(2\kappa_1\right) + 1/\left(2\kappa_A\right), \\ 1/\kappa_b^{(21\mathrm{AA})} < 1/\kappa_b + 1/\kappa_2 + 1/\left(2\kappa_1\right) + 1/\left(2\kappa_A\right), \\ 1/\kappa_c^{(21\mathrm{AA})} < 1/\kappa_c + 1/\kappa_5 + 1/\kappa_3 + 1/\kappa_2 + 1/\kappa_1 + 1/\kappa_A, \\ 1/\kappa_d^{(21\mathrm{AA})} < 1/\kappa_d + 1/\kappa_5 + 1/\left(2\kappa_1\right) + 1/\left(2\kappa_A\right). \end{cases} \tag{S110}$$

In practice, the requirement for proteome efficiency when using amino acids is even higher, since the biomass synthesis pathway is accompanied by energy biogenesis for Group A carbon sources, but not for amino acids. Combining Eqs. **S108** and **S109**, we have:

$$\begin{cases} J_r^{(\mathrm{E})} + J_f^{(\mathrm{E})} = \varphi_{21\mathrm{AA}} \cdot \lambda, \\ \dfrac{J_r^{(\mathrm{E})}}{\varepsilon_r} + \dfrac{J_f^{(\mathrm{E})}}{\varepsilon_f} = \phi_{\max} - \psi_{21\mathrm{AA}} \cdot \lambda, \end{cases} \tag{S111}$$

where $J_r^{(\mathrm{E})}$, $J_f^{(\mathrm{E})}$ follow Eq. **S30**, while ε_r and ε_f follow Eq. **S31**. ${\psi_{21\mathrm{AA}}}^{-1}$ is the proteome efficiency for biomass generation in the biomass synthesis pathway under this nutrient condition, with

$$\psi_{21\mathrm{AA}} = \frac{1}{\kappa_t} + \frac{\eta_{a1}}{\kappa_A} + \frac{\eta_{a1}}{\kappa_{a1}} + \frac{\eta_{a2}}{\kappa_{a2}^{(21\mathrm{AA})}} + \frac{\eta_b}{\kappa_b^{(21\mathrm{AA})}} + \frac{\eta_c}{\kappa_c^{(21\mathrm{AA})}} + \frac{\eta_d}{\kappa_d^{(21\mathrm{AA})}}. \tag{S112}$$

$\phi_{21\mathrm{AA}}$ is an energy demand coefficient, with

$$\varphi_{21\mathrm{AA}} \equiv \eta_{\mathrm{E}} - \beta_{a1} \cdot \eta_{a1}. \tag{S113}$$

Combining Eqs. **S111** and **S31**, the formula for the growth rate is:

$$\lambda(\kappa_A) = \begin{cases} \lambda_r^{(21\mathrm{AA})} \equiv \dfrac{\phi_{\max}}{\varphi_{21\mathrm{AA}} / \varepsilon_r(\kappa_A) + \psi_{21\mathrm{AA}}(\kappa_A)} & \varepsilon_r(\kappa_A) > \varepsilon_f(\kappa_A), \\ \lambda_f^{(21\mathrm{AA})} \equiv \dfrac{\phi_{\max}}{\varphi_{21\mathrm{AA}} / \varepsilon_f(\kappa_A) + \psi_{21\mathrm{AA}}(\kappa_A)} & \varepsilon_r(\kappa_A) < \varepsilon_f(\kappa_A). \end{cases} \tag{S114}$$

In fact, Eqs. **S37**–**S42** still apply. $\varepsilon_{r/f}(\kappa_A^{(\mathrm{C})})$ satisfies Eq. **S43**, while $\lambda_{\mathrm{C}}^{(21\mathrm{AA})} = \lambda(\kappa_A^{(\mathrm{C})})$ and $\lambda_{\max}^{(21\mathrm{AA})} = \lambda(\kappa_A^{\max})$ are:

$$\begin{cases} \lambda_{\mathrm{C}}^{(21\mathrm{AA})} = \dfrac{\phi_{\max}}{\varphi_{21\mathrm{AA}} / \varepsilon_{r/f}\left(\kappa_A^{(\mathrm{C})}\right) + \psi_{21\mathrm{AA}}\left(\kappa_A^{(\mathrm{C})}\right)}, \\ \lambda_{\max}^{(21\mathrm{AA})} = \dfrac{\phi_{\max}}{\varphi_{21\mathrm{AA}} / \varepsilon_f\left(\kappa_A^{\max}\right) + \psi_{21\mathrm{AA}}\left(\kappa_A^{\max}\right)}. \end{cases} \tag{S115}$$

When extrinsic noise is taken into account, $\lambda_{\mathrm{C}}^{(21\mathrm{AA})}$ approximately follows a Gaussian distribution:

$$\lambda_{\mathrm{C}}^{(21\mathrm{AA})} \sim \mathcal{N}\left(\mu_{\lambda_{\mathrm{C}}^{(21\mathrm{AA})}}, \sigma^2_{\lambda_{\mathrm{C}}^{(21\mathrm{AA})}}\right), \tag{S116}$$

and the normalized fluxes $J_r^{(N)}$, $J_f^{(N)}$ change to:

$$\begin{cases} J_f^{(\mathrm{N})}(\lambda) = \dfrac{\varphi_{21\mathrm{AA}}}{\beta_f^{(A)}} \cdot \lambda \cdot \left[\mathrm{erf}\left(\dfrac{\lambda - \mu_{\lambda_\mathrm{C}^{(21\mathrm{AA})}}}{\sqrt{2}\sigma_{\lambda_\mathrm{C}^{(21\mathrm{AA})}}} \right) + 1 \right], \\ J_r^{(\mathrm{N})}(\lambda) = \dfrac{\varphi_{21\mathrm{AA}}}{\beta_r^{(A)}} \cdot \lambda \cdot \left[1 - \mathrm{erf}\left(\dfrac{\lambda - \mu_{\lambda_\mathrm{C}^{(21\mathrm{AA})}}}{\sqrt{2}\sigma_{\lambda_\mathrm{C}^{(21\mathrm{AA})}}} \right) \right]. \end{cases} \tag{S117}$$

The above analysis can be extended to cases where a Group A carbon source is mixed with arbitrary combinations of amino acids. Eqs. **S111**, **S114**–**S117** would remain in a similar form, while Eqs. **S112**–**S113** would change depending on the combinations of amino acid. In **Appendix-fig. 2B-C**, we compare model predictions (see also **Appendix 7.2** and Eq. **S157**) with experimental data (Basan et al., 2015; Wallden et al., 2016) from mixtures of 21 or 7 types of amino acids along with a Group A carbon source, demonstrating quantitative agreement. Additionally, the increase in the critical threshold of growth rate for the growth rate-dependent fermentation flux in mixtures with extracellular amino acids (i.e., $\lambda_\mathrm{C}^{(21\mathrm{AA})}$, $\lambda_\mathrm{C}^{(7\mathrm{AA})} > \lambda_\mathrm{C}$, see **Appendix-fig. 2C**) has also been observed in other experimental findings (Peebo et al., 2015).

Appendix 5 Enzyme allocation upon perturbations

Appendix 5.1 Carbon limitation within Group A carbon sources

In Eq. S28, we present the model predictions for the dependencies of enzyme proteomic mass fractions on growth rate and energy fluxes. To compare with experiments, we assume the same extent of extrinsic noise in $\lambda_\mathrm{C}^{(\mathrm{pr})}$ as specified in Appendix 2.3. Relative protein expression data for enzymes within glycolysis and the TCA cycle are available from existing studies and are comparable to the φ_1–φ_4 enzymes of our model (**Fig. 1B**). Upon κ_A perturbation, κ_A is a variable while w_0 is fixed (see **Appendix 1.5**). Combining Eqs. **S28** and **S47** (with $w_0 = 0$), we obtain:

$$\begin{cases} \phi_1 = \dfrac{\lambda}{\kappa_1}\left\{ \dfrac{\varphi \cdot \left(\beta_r^{(A)} - \beta_f^{(A)}\right)}{2\beta_r^{(A)} \cdot \beta_f^{(A)}} \cdot \left[\mathrm{erf}\left(\dfrac{\lambda - \mu_{\lambda_\mathrm{C}}}{\sqrt{2}\sigma_{\lambda_\mathrm{C}}} \right) + 1 \right] + \dfrac{\varphi}{\beta_r^{(A)}} + \dfrac{\eta_{a2} + \eta_b + 2\eta_c + \eta_d}{2} \right\}, \\ \phi_2 = \dfrac{\lambda}{\kappa_2}\left\{ \dfrac{\varphi \cdot \left(\beta_r^{(A)} - \beta_f^{(A)}\right)}{\beta_r^{(A)} \cdot \beta_f^{(A)}} \cdot \left[\mathrm{erf}\left(\dfrac{\lambda - \mu_{\lambda_\mathrm{C}}}{\sqrt{2}\sigma_{\lambda_\mathrm{C}}} \right) + 1 \right] + \dfrac{2\varphi}{\beta_r^{(A)}} + \eta_b + \eta_c \right\}, \\ \phi_3 = \dfrac{\lambda}{\kappa_3}\left\{ \dfrac{\varphi}{\beta_r^{(A)}} \cdot \left[1 - \mathrm{erf}\left(\dfrac{\lambda - \mu_{\lambda_\mathrm{C}}}{\sqrt{2}\sigma_{\lambda_\mathrm{C}}} \right) \right] + \eta_c \right\}, \\ \phi_4 = \dfrac{\lambda}{\kappa_4} \cdot \dfrac{\varphi}{\beta_r^{(A)}} \cdot \left[1 - \mathrm{erf}\left(\dfrac{\lambda - \mu_{\lambda_\mathrm{C}}}{\sqrt{2}\sigma_{\lambda_\mathrm{C}}} \right) \right]. \end{cases} \tag{S118}$$

In **Appendix-fig. 3C-D**, we show the comparisons between model predictions (Eq. **S118**, $w_0 = 0$) and experimental data (Hui et al., 2015), which are consistent overall. We then consider the influence of maintenance energy as specified in Appendix 3.2. Here, we continue to choose $w_0 =$

2.5 (h^{-1} A as previously adopted in Appendix 3.3. Thus, Eq. S28 still holds. Combined with Eq. S85 under the condition that $\iota = 0$, we have:

$$\begin{cases} \phi_1 = \dfrac{1}{2\cdot\kappa_1}\left\{\dfrac{\varphi\cdot\lambda+w_0}{\beta_f^{(A)}}\cdot\left[\mathrm{erf}\left(\dfrac{\lambda-\mu_{\lambda_c}}{\sqrt{2}\sigma_{\lambda_c}}\right)+1\right]+\dfrac{\varphi\cdot\lambda+w_0}{\beta_r^{(A)}}\cdot\left[1-\mathrm{erf}\left(\dfrac{\lambda-\mu_{\lambda_c}}{\sqrt{2}\sigma_{\lambda_c}}\right)\right]+\left(\eta_{a2}+\eta_b+2\eta_c+\eta_d\right)\lambda\right\}, \\ \phi_2 = \dfrac{1}{\kappa_2}\left\{\dfrac{\varphi\cdot\lambda+w_0}{\beta_f^{(A)}}\cdot\left[\mathrm{erf}\left(\dfrac{\lambda-\mu_{\lambda_c}}{\sqrt{2}\sigma_{\lambda_c}}\right)+1\right]+\dfrac{\varphi\cdot\lambda+w_0}{\beta_r^{(A)}}\cdot\left[1-\mathrm{erf}\left(\dfrac{\lambda-\mu_{\lambda_c}}{\sqrt{2}\sigma_{\lambda_c}}\right)\right]+\left(\eta_b+\eta_c\right)\lambda\right\}, \\ \phi_3 = \dfrac{1}{\kappa_3}\left\{\dfrac{\varphi\cdot\lambda+w_0}{\beta_r^{(A)}}\cdot\left[1-\mathrm{erf}\left(\dfrac{\lambda-\mu_{\lambda_c}}{\sqrt{2}\sigma_{\lambda_c}}\right)\right]+\eta_c\cdot\lambda\right\}, \\ \phi_4 = \dfrac{1}{\kappa_4}\cdot\dfrac{\varphi\cdot\lambda+w_0}{\beta_r^{(A)}}\cdot\left[1-\mathrm{erf}\left(\dfrac{\lambda-\mu_{\lambda_c}}{\sqrt{2}\sigma_{\lambda_c}}\right)\right]. \end{cases} \tag{S119}$$

In **Fig. 4A-B**, we show that the model predictions (Eq. **S119**, $w_0 = 2.5$ (h^{-1}) generally agree with the experiments (Hui et al., 2015). However, there are different basal expressions of these enzymes, likely due to living demands other than cell proliferation, such as preparation for starvation (Mori et al., 2017) or changes in the type of the nutrient (Basan et al., 2020; Kussell and Leibler, 2005).

Appendix 5.2 Overexpression of useless proteins

In the case of φ_Z perturbation under each nutrient condition with fixed κ_A (see Appendix 3.1), we consider the same extent of extrinsic noise in k_i^{ext} as specified in Appendix 2.3. The relation between enzyme allocation and growth rate can be obtained by combining Eqs. S28 and S58 (with $w_0 = 0$):

$$\begin{cases} \phi_1 = \dfrac{\lambda}{2\cdot\kappa_1}\left\{\dfrac{\varphi}{\beta_r^{(A)}}\cdot\left[1-\mathrm{erf}\left(\dfrac{\lambda(\kappa_A,0)-\mu_{\lambda_c}(0)}{\sqrt{2}\sigma_{\lambda_c}(0)}\right)\right]+\dfrac{\varphi}{\beta_f^{(A)}}\cdot\left[\mathrm{erf}\left(\dfrac{\lambda(\kappa_A,0)-\mu_{\lambda_c}(0)}{\sqrt{2}\sigma_{\lambda_c}(0)}\right)+1\right]+\left(\eta_{a2}+\eta_b+2\eta_c+\eta_d\right)\right\}, \\ \phi_2 = \dfrac{\lambda}{\kappa_2}\left\{\dfrac{\varphi}{\beta_r^{(A)}}\cdot\left[1-\mathrm{erf}\left(\dfrac{\lambda(\kappa_A,0)-\mu_{\lambda_c}(0)}{\sqrt{2}\sigma_{\lambda_c}(0)}\right)\right]+\dfrac{\varphi}{\beta_f^{(A)}}\cdot\left[\mathrm{erf}\left(\dfrac{\lambda(\kappa_A,0)-\mu_{\lambda_c}(0)}{\sqrt{2}\sigma_{\lambda_c}(0)}\right)+1\right]+\left(\eta_b+\eta_c\right)\right\}, \\ \phi_3 = \dfrac{\lambda}{\kappa_3}\left\{\dfrac{\varphi}{\beta_r^{(A)}}\cdot\left[1-\mathrm{erf}\left(\dfrac{\lambda(\kappa_A,0)-\mu_{\lambda_c}(0)}{\sqrt{2}\sigma_{\lambda_c}(0)}\right)\right]+\eta_c\right\}, \\ \phi_4 = \dfrac{\lambda}{\kappa_4}\left\{\dfrac{\varphi}{\beta_r^{(A)}}\cdot\left[1-\mathrm{erf}\left(\dfrac{\lambda(\kappa_A,0)-\mu_{\lambda_c}(0)}{\sqrt{2}\sigma_{\lambda_c}(0)}\right)\right]\right\}. \end{cases} \tag{S120}$$

Here $\lambda(\kappa_A, 0)$ is the growth rate for $\varphi_Z = 0$, and thus it is a parameter rather than a variable. The growth rate is defined as $\lambda(\kappa_A, \varphi_Z)$, which follows Eq. S50. Thus, φ_i is proportional to the growth rate λ. In **Appendix-fig. 3E-F**, we observe that the model predictions (Eq. **S120**) generally agree with the experiments (Basan et al., 2015). Next, we consider the influence of maintenance energy with $w_0 = 2.5$ (h^{-1}). Combining Eqs. S28, S58 and S85 (with $\iota = 0$), we get:

$$\begin{cases}
\phi_1 = \dfrac{w_0}{2\kappa_1}\left\{\dfrac{1}{\beta_f^{(A)}}\cdot\left[\operatorname{erf}\left(\dfrac{\lambda(\kappa_A,0)-\mu_{\lambda_c}(0)}{\sqrt{2}\sigma_{\lambda_c}(0)}\right)+1\right]+\dfrac{1}{\beta_r^{(A)}}\cdot\left[1-\operatorname{erf}\left(\dfrac{\lambda(\kappa_A,0)-\mu_{\lambda_c}(0)}{\sqrt{2}\sigma_{\lambda_c}(0)}\right)\right]\right\} \\
+\dfrac{\lambda}{2\kappa_1}\left\{\dfrac{\varphi}{\beta_f^{(A)}}\cdot\left[\operatorname{erf}\left(\dfrac{\lambda(\kappa_A,0)-\mu_{\lambda_c}(0)}{\sqrt{2}\sigma_{\lambda_c}(0)}\right)+1\right]+\dfrac{\varphi}{\beta_r^{(A)}}\cdot\left[1-\operatorname{erf}\left(\dfrac{\lambda(\kappa_A,0)-\mu_{\lambda_c}(0)}{\sqrt{2}\sigma_{\lambda_c}(0)}\right)\right]+(\eta_{a2}+\eta_b+2\eta_c+\eta_d)\right\}, \\
\phi_2 = \dfrac{w_0}{\kappa_2}\left\{\dfrac{1}{\beta_f^{(A)}}\cdot\left[\operatorname{erf}\left(\dfrac{\lambda(\kappa_A,0)-\mu_{\lambda_c}(0)}{\sqrt{2}\sigma_{\lambda_c}(0)}\right)+1\right]+\dfrac{1}{\beta_r^{(A)}}\cdot\left[1-\operatorname{erf}\left(\dfrac{\lambda(\kappa_A,0)-\mu_{\lambda_c}(0)}{\sqrt{2}\sigma_{\lambda_c}(0)}\right)\right]\right\} \\
+\dfrac{\lambda}{\kappa_2}\left\{\dfrac{\varphi}{\beta_f^{(A)}}\cdot\left[\operatorname{erf}\left(\dfrac{\lambda(\kappa_A,0)-\mu_{\lambda_c}(0)}{\sqrt{2}\sigma_{\lambda_c}(0)}\right)+1\right]+\dfrac{\varphi}{\beta_r^{(A)}}\cdot\left[1-\operatorname{erf}\left(\dfrac{\lambda(\kappa_A,0)-\mu_{\lambda_c}(0)}{\sqrt{2}\sigma_{\lambda_c}(0)}\right)\right]+(\eta_b+\eta_c)\right\}, \\
\phi_3 = \dfrac{\lambda}{\kappa_3}\left\{\dfrac{\varphi}{\beta_r^{(A)}}\cdot\left[1-\operatorname{erf}\left(\dfrac{\lambda(\kappa_A,0)-\mu_{\lambda_c}(0)}{\sqrt{2}\sigma_{\lambda_c}(0)}\right)\right]+\eta_c\right\}+\dfrac{w_0}{\kappa_3}\cdot\dfrac{1}{\beta_r^{(A)}}\cdot\left[1-\operatorname{erf}\left(\dfrac{\lambda(\kappa_A,0)-\mu_{\lambda_c}(0)}{\sqrt{2}\sigma_{\lambda_c}(0)}\right)\right], \\
\phi_4 = \dfrac{\lambda}{\kappa_4}\cdot\dfrac{\varphi}{\beta_r^{(A)}}\cdot\left[1-\operatorname{erf}\left(\dfrac{\lambda(\kappa_A,0)-\mu_{\lambda_c}(0)}{\sqrt{2}\sigma_{\lambda_c}(0)}\right)\right]+\dfrac{w_0}{\kappa_4}\cdot\dfrac{1}{\beta_r^{(A)}}\cdot\left[1-\operatorname{erf}\left(\dfrac{\lambda(\kappa_A,0)-\mu_{\lambda_c}(0)}{\sqrt{2}\sigma_{\lambda_c}(0)}\right)\right].
\end{cases} \tag{S121}$$

Here, the growth rate is defined as $\lambda(\kappa_A, \varphi_Z)$, and $\lambda(\kappa_A, 0)$ is a parameter rather than a variable.

Thus, φ_i is a linear function of the growth rate λ, with a positive slope and a positive y-intercept. In **Fig. 4C-D** and **Appendix-fig. 3I-J**, we show that the model predictions (Eq. **S121**) agree quantitively with the experimental data (Basan et al., 2015).

Appendix 5.3 Energy dissipation

In the case of energy dissipation under each nutrient condition, w is perturbed while κ_A is fixed. The relation between protein allocation and growth rate can be obtained by combining Eqs. S28 and S70. However, since w is explicitly present in Eq. S70, it is necessary to reduce this variable to obtain the growth rate dependence of enzyme allocation. From Eq. S64, we have:

$$\lambda(\kappa_A, w) = \lambda(\kappa_A, 0)\left\{1-\frac{w}{\phi_{\max}}\cdot\left[\frac{1}{\varepsilon_r(\kappa_A)}-\theta\left(\varepsilon_f(\kappa_A)-\varepsilon_r(\kappa_A)\right)\cdot\left(\frac{1}{\varepsilon_r(\kappa_A)}-\frac{1}{\varepsilon_f(\kappa_A)}\right)\right]\right\}. \tag{S122}$$

Here, $\lambda(\kappa_A, 0) \equiv \lambda(\kappa_A, w = 0)$ (satisfying Eq. S64) is a parameter rather than a variable. "θ" stands for the Heaviside step function. Thus, we have:

$$w(\lambda) = \frac{\phi_{\max}\cdot\left[1-\lambda/\lambda(\kappa_A,0)\right]}{\left[1/\varepsilon_r(\kappa_A)-\theta\left(\varepsilon_f(\kappa_A)-\varepsilon_r(\kappa_A)\right)\cdot\left(1/\varepsilon_r(\kappa_A)-1/\varepsilon_f(\kappa_A)\right)\right]}, \tag{S123}$$

where the energy dissipation coefficient w is regarded as a function of the growth rate.

Combining Eqs. S28, S70 and S123, we get:

$$\begin{cases} \phi_1 = \dfrac{1}{2\kappa_1}\left\{\left[\dfrac{\varphi\cdot\lambda+w(\lambda)}{\beta_f^{(A)}}-\dfrac{\varphi\cdot\lambda+w(\lambda)}{\beta_r^{(A)}}\right]\cdot\left[\operatorname{erf}\left(\dfrac{\lambda-\mu_{\lambda_c}(0)\left\{1-w/\left[\varepsilon_{r/f}\left(\kappa_A^{(C)}\right)\phi_{\max}\right]\right\}}{\sqrt{2}\sigma_{\lambda_c}(0)\left\{1-w/\left[\varepsilon_{r/f}\left(\kappa_A^{(C)}\right)\phi_{\max}\right]\right\}}\right)+1\right]+\dfrac{2\left[\varphi\cdot\lambda+w(\lambda)\right]}{\beta_r^{(A)}}+\left(\eta_{a2}+\eta_b+2\eta_c+\eta_d\right)\cdot\lambda\right\}, \\ \phi_2 = \dfrac{1}{\kappa_2}\left[\left[\dfrac{\varphi\cdot\lambda+w(\lambda)}{\beta_f^{(A)}}-\dfrac{\varphi\cdot\lambda+w(\lambda)}{\beta_r^{(A)}}\right]\cdot\left[\operatorname{erf}\left(\dfrac{\lambda-\mu_{\lambda_c}(0)\left\{1-w/\left[\varepsilon_{r/f}\left(\kappa_A^{(C)}\right)\phi_{\max}\right]\right\}}{\sqrt{2}\sigma_{\lambda_c}(0)\left\{1-w/\left[\varepsilon_{r/f}\left(\kappa_A^{(C)}\right)\phi_{\max}\right]\right\}}\right)+1\right]+\dfrac{2\left[\varphi\cdot\lambda+w(\lambda)\right]}{\beta_r^{(A)}}+\left(\eta_b+\eta_c\right)\cdot\lambda\right], \\ \phi_3 = \dfrac{1}{\kappa_3}\left(\dfrac{\varphi\cdot\lambda+w(\lambda)}{\beta_r^{(A)}}\cdot\left[1-\operatorname{erf}\left(\dfrac{\lambda-\mu_{\lambda_c}(0)\left\{1-w(\lambda)/\left[\varepsilon_{r/f}\left(\kappa_A^{(C)}\right)\phi_{\max}\right]\right\}}{\sqrt{2}\sigma_{\lambda_c}(0)\left\{1-w(\lambda)/\left[\varepsilon_{r/f}\left(\kappa_A^{(C)}\right)\phi_{\max}\right]\right\}}\right)\right]+\eta_c\cdot\lambda\right), \\ \phi_4 = \dfrac{1}{\kappa_4}\cdot\dfrac{\varphi\cdot\lambda+w(\lambda)}{\beta_r^{(A)}}\cdot\left[1-\operatorname{erf}\left(\dfrac{\lambda-\mu_{\lambda_c}(0)\left\{1-w(\lambda)/\left[\varepsilon_{r/f}\left(\kappa_A^{(C)}\right)\phi_{\max}\right]\right\}}{\sqrt{2}\sigma_{\lambda_c}(0)\left\{1-w(\lambda)/\left[\varepsilon_{r/f}\left(\kappa_A^{(C)}\right)\phi_{\max}\right]\right\}}\right)\right], \end{cases} \tag{S124}$$

where $w(\lambda)$ follows Eq. S123. When κ_A lies in the vicinity of $\kappa_A^{(C)}$ or w is small so that

$$\left(1-\frac{w}{\varepsilon_{r/f}\left(\kappa_A\right)\cdot\phi_{\max}}\right)\Big/\left(1-\frac{w}{\varepsilon_{r/f}\left(\kappa_A^{(C)}\right)\cdot\phi_{\max}}\right)\approx 1, \tag{S125}$$

then we have:

$$\begin{cases} J_f^{(N)}(\lambda,w) = \dfrac{\varphi\cdot\lambda+w}{\beta_f^{(A)}}\cdot\left[\operatorname{erf}\left(\dfrac{\lambda\left(\kappa_A,0\right)-\mu_{\lambda_c}(0)}{\sqrt{2}\sigma_{\lambda_c}(0)}\right)+1\right], \\ J_r^{(N)}(\lambda,w) = \dfrac{\varphi\cdot\lambda+w}{\beta_r^{(A)}}\cdot\left[1-\operatorname{erf}\left(\dfrac{\lambda\left(\kappa_A,0\right)-\mu_{\lambda_c}(0)}{\sqrt{2}\sigma_{\lambda_c}(0)}\right)\right], \end{cases} \tag{S126}$$

and thus:

$$\begin{cases} \phi_1 = \dfrac{1}{2\kappa_1}\left\{\left[\dfrac{\varphi\cdot\lambda+w(\lambda)}{\beta_f^{(A)}}-\dfrac{\varphi\cdot\lambda+w(\lambda)}{\beta_r^{(A)}}\right]\cdot\left[\operatorname{erf}\left(\dfrac{\lambda\left(\kappa_A,0\right)-\mu_{\lambda_c}(0)}{\sqrt{2}\sigma_{\lambda_c}(0)}\right)+1\right]+\dfrac{2\left[\varphi\cdot\lambda+w(\lambda)\right]}{\beta_r^{(A)}}+\left(\eta_{a2}+\eta_b+2\eta_c+\eta_d\right)\cdot\lambda\right\}, \\ \phi_2 = \dfrac{1}{\kappa_2}\left[\left[\dfrac{\varphi\cdot\lambda+w(\lambda)}{\beta_f^{(A)}}-\dfrac{\varphi\cdot\lambda+w(\lambda)}{\beta_r^{(A)}}\right]\cdot\left[\operatorname{erf}\left(\dfrac{\lambda\left(\kappa_A,0\right)-\mu_{\lambda_c}(0)}{\sqrt{2}\sigma_{\lambda_c}(0)}\right)+1\right]+\dfrac{2\left[\varphi\cdot\lambda+w(\lambda)\right]}{\beta_r^{(A)}}+\left(\eta_b+\eta_c\right)\cdot\lambda\right], \\ \phi_3 = \dfrac{1}{\kappa_3}\left(\dfrac{\varphi\cdot\lambda+w(\lambda)}{\beta_r^{(A)}}\cdot\left[1-\operatorname{erf}\left(\dfrac{\lambda\left(\kappa_A,0\right)-\mu_{\lambda_c}(0)}{\sqrt{2}\sigma_{\lambda_c}(0)}\right)\right]+\eta_c\cdot\lambda\right), \\ \phi_4 = \dfrac{1}{\kappa_4}\cdot\dfrac{\varphi\cdot\lambda+w(\lambda)}{\beta_r^{(A)}}\cdot\left[1-\operatorname{erf}\left(\dfrac{\lambda\left(\kappa_A,0\right)-\mu_{\lambda_c}(0)}{\sqrt{2}\sigma_{\lambda_c}(0)}\right)\right], \end{cases} \tag{S127}$$

Note that in Eq. S123, w is a linear function of λ with a negative slope. Thus φ_i exhibits a linear relation with λ when Eq. S125 is satisfied (see Eq. S127). In fact, the slope of φ_4 is certainly negative (combining Eqs. S64, S123 and S127), while the sign of the slope for other φ_i depends on parameters. For a given nutrient, the enzymes corresponding to the same φ_i should exhibit the same slope sign. Another restriction is that if the slope sign of φ_1 is negative, then the slope sign of φ_2 is surely negative. In **Appendix-fig. 3K-N**, we show that our model results agree well with the experimental data (Basan et al., 2015) (Eq. S127).

Appendix 6 Other aspects of the model

Appendix 6.1 A coarse-grained model with more details

To compare with experiments, we consider a coarse-grained model with more details, as shown in **Appendix-fig. 2F**. Here, nodes M_6, M_7 represent GA3P and DHAP, respectively. Other nodes follow the descriptions specified in **Appendix 2.1**. Each biochemical reaction follows Eq. **S5** with $b_i = 1$ except that $M_1 \to M_6 + M_7$ and $M_3 + M_5 \to M_4$. By applying flux balance to the stoichiometric fluxes, combined with Eq. **S8**, we obtain:

$$\begin{cases} \Phi_A \cdot \xi_A = \Phi_1 \cdot \xi_1 + \Phi_{a1} \cdot \xi_{a1}, \\ \Phi_{11} \cdot \xi_{11} = \Phi_{10} \cdot \xi_{10} + \Phi_1 \cdot \xi_1, \Phi_{10} \cdot \xi_{10} = \Phi_1 \cdot \xi_1, \\ \Phi_{11} \cdot \xi_{11} = \Phi_2 \cdot \xi_2 + \Phi_5 \cdot \xi_5 + \Phi_{a2} \cdot \xi_{a2}, \\ \Phi_2 \cdot \xi_2 = \Phi_3 \cdot \xi_3 + \Phi_6 \cdot \xi_6 + \Phi_b \cdot \xi_b, \\ \Phi_5 \cdot \xi_5 + \Phi_4 \cdot \xi_4 = \Phi_3 \cdot \xi_3 + \Phi_d \cdot \xi_d, \\ \Phi_3 \cdot \xi_3 = \Phi_4 \cdot \xi_4 + \Phi_c \cdot \xi_c. \end{cases} \tag{S128}$$

While Eqs. **S22**–**S25** still hold. By applying the substitutions specified in Eqs. **S9**, **S12**, **S14**–**S18**, combined with Eqs. **S4**, **S10**, **S22**–**S25**, **S128**, and the constraint of proteome resource allocation, we get:

$$\begin{cases} \phi_A \cdot \kappa_A = \phi_1 \cdot \kappa_1 + \phi_{a1} \cdot \kappa_{a1}, \\ \phi_{11} \cdot \kappa_{11} = \phi_{10} \cdot \kappa_{10} + \phi_1 \cdot \kappa_1, \phi_{10} \cdot \kappa_{10} = \phi_1 \cdot \kappa_1, \\ \phi_{11} \cdot \kappa_{11} = \phi_2 \cdot \kappa_2 + \phi_5 \cdot \kappa_5 + \phi_{a2} \cdot \kappa_{a2}, \\ \phi_2 \cdot \kappa_2 = \phi_3 \cdot \kappa_3 + \phi_6 \cdot \kappa_6 + \phi_b \cdot \kappa_b, \\ \phi_5 \cdot \kappa_5 + \phi_4 \cdot \kappa_4 = \phi_3 \cdot \kappa_3 + \phi_d \cdot \kappa_d, \\ \phi_3 \cdot \kappa_3 = \phi_4 \cdot \kappa_4 + \phi_c \cdot \kappa_c, \\ \phi_{a1} \cdot \kappa_{a1} = \eta_{a1} \cdot \lambda, \phi_{a2} \cdot \kappa_{a2} = \eta_{a2} \cdot \lambda, \phi_b \cdot \kappa_b = \eta_b \cdot \lambda, \phi_c \cdot \kappa_c = \eta_c \cdot \lambda, \phi_d \cdot \kappa_d = \eta_d \cdot \lambda, \\ \beta_1 \cdot \phi_1 \cdot \kappa_1 + \beta_2 \cdot \phi_2 \cdot \kappa_2 + \beta_3 \cdot \phi_3 \cdot \kappa_3 + \beta_4 \cdot \phi_4 \cdot \kappa_4 + \beta_6 \cdot \phi_6 \cdot \kappa_6 + \beta_{a1} \cdot \phi_{a1} \cdot \kappa_{a1} = J_{\mathrm{E}}^{(\mathrm{N})}, \\ J_{\mathrm{E}}^{(\mathrm{N})} = \eta_{\mathrm{E}} \cdot \lambda, \lambda = \phi_R \cdot \kappa_t, J_r^{(\mathrm{N})} = \phi_4 \cdot \kappa_4, J_f^{(\mathrm{N})} = \phi_6 \cdot \kappa_6, \\ \phi_{\mathrm{R}} + \phi_A + \phi_1 + \phi_2 + \phi_3 + \phi_4 + \phi_5 + \phi_6 + \phi_7 + \phi_8 + \phi_{a1} + \phi_{a2} + \phi_b + \phi_c + \phi_d = \phi_{\max}. \end{cases} \tag{S129}$$

Then, Eq. **S28** still holds, while φ_{10} and φ_{11} are:

$$\begin{cases} \phi_{10} = \left[J_r^{(\mathrm{N})} + J_f^{(\mathrm{N})} + \left(\eta_{a2} + \eta_b + 2\eta_c + \eta_d \right) \lambda \right] \Big/ \left(2 \cdot \kappa_{10} \right), \\ \phi_{11} = \left[J_r^{(\mathrm{N})} + J_f^{(\mathrm{N})} + \left(\eta_{a2} + \eta_b + 2\eta_c + \eta_d \right) \lambda \right] \Big/ \kappa_{11}. \end{cases} \tag{S130}$$

By substituting Eqs. **S28** and **S130** into Eq. **S129**, we get:

$$\begin{cases} J_r^{(\mathrm{E})} + J_f^{(\mathrm{E})} = \varphi \cdot \lambda, \\ \dfrac{J_r^{(\mathrm{E})}}{\varepsilon_r^{(\mathrm{dt})}} + \dfrac{J_f^{(\mathrm{E})}}{\varepsilon_f^{(\mathrm{dt})}} = \phi_{\max} - \psi_{\mathrm{dt}} \cdot \lambda, \end{cases} \tag{S131}$$

where “dt” stands for details. Eqs. **S30** and **S33** still hold. $\varepsilon_r^{(\mathrm{dt})}$ and $\varepsilon_f^{(\mathrm{dt})}$ represent the proteome efficiencies for energy biogenesis in the respiration and fermentation pathways, respectively, with

$$\begin{cases} \varepsilon_r^{(\mathrm{dt})} = \dfrac{\beta_r^{(A)}}{1/\kappa_A + 1/\kappa_1 + 1/\kappa_{10} + 2/\kappa_{11} + 2/\kappa_2 + 2/\kappa_3 + 2/\kappa_4}, \\ \varepsilon_f^{(\mathrm{dt})} = \dfrac{\beta_f^{(A)}}{1/\kappa_A + 1/\kappa_1 + 1/\kappa_{10} + 2/\kappa_{11} + 2/\kappa_2 + 2/\kappa_6}. \end{cases} \tag{S132}$$

ψ_{dt}^{-1} is the proteome efficiency for biomass generation in the biomass synthesis pathway, with

$$\psi_{\mathrm{dt}} = \frac{1}{\kappa_t} + \frac{1+\eta_{a1}+\eta_c}{2\kappa_A} + \left(\eta_{a2}+\eta_b+2\eta_c+\eta_d\right)\left(\frac{1}{2\kappa_1} + \frac{1}{2\kappa_{10}} + \frac{1}{\kappa_{11}}\right) + \frac{\eta_b+\eta_c}{\kappa_2} + \frac{\eta_c}{\kappa_3} + \frac{\eta_c+\eta_d}{\kappa_5} + \sum_i^{a1,a2,b,c,d} \frac{\eta_i}{\kappa_i}. \tag{S133}$$

Appendix 6.2 Estimation of the in vivo enzyme catalytic rates

We use the method introduced by Davidi *et al.* (Davidi et al., 2016), combined with proteome experimental data (Basan et al., 2015) (**Appendix-table 2**), to estimate the in vivo enzyme catalytic rates. Combining Eqs. **S28** and **S130**, we have:

$$\begin{cases} \kappa_1 = \left[J_r^{(\mathrm{N})} + J_f^{(\mathrm{N})} + \left(\eta_{a2}+\eta_b+2\eta_c+\eta_d\right)\lambda\right] \Big/ \left(2\cdot\phi_1\right), \\ \kappa_2 = \left[J_r^{(\mathrm{N})} + J_f^{(\mathrm{N})} + \left(\eta_b+\eta_c\right)\lambda\right] \Big/ \phi_2, \\ \kappa_3 = \left(J_r^{(\mathrm{N})} + \eta_c\cdot\lambda\right) \Big/ \phi_3, \kappa_4 = J_r^{(\mathrm{N})} \Big/ \phi_4, \\ \kappa_5 = \left(\eta_c+\eta_d\right)\lambda \Big/ \phi_5, \kappa_6 = J_f^{(\mathrm{N})} \Big/ \phi_6, \\ \kappa_{10} = \left[J_r^{(\mathrm{N})} + J_f^{(\mathrm{N})} + \left(\eta_{a2}+\eta_b+2\eta_c+\eta_d\right)\lambda\right] \Big/ \left(2\cdot\phi_{10}\right), \\ \kappa_{11} = \left[J_r^{(\mathrm{N})} + J_f^{(\mathrm{N})} + \left(\eta_{a2}+\eta_b+2\eta_c+\eta_d\right)\lambda\right] \Big/ \phi_{11}. \end{cases} \tag{S134}$$

Here, $J_r^{(\mathrm{N})}$, $J_f^{(\mathrm{N})}$, λ and φ_i (i = 1-6,10-11) are measurable from experiments (see **Appendix 8.1** and **Appendix-table 2**). Thus, we can obtain the in vivo values of κ_i from Eq. **S134**. Combined with Eqs. **S17** and **S20**, we have

$$k_i^{\mathrm{cat}} = \frac{r_{\mathrm{carbon}}}{r_{\mathrm{protein}}} \cdot \frac{m_{E_i}}{m_{\mathrm{carbon}}} \cdot \kappa_i \cdot \left[\sum_i r_i \Big/ N_{\mathrm{EP}_i}^{\mathrm{carbon}} \right]. \tag{S135}$$

Eq. **S135** is the in vivo result for the enzyme catalytic rate. In **Appendix-fig. 2G**, we show a comparison between in vivo and in vitro results for k_{cat} values of enzymes within glycolysis and the TCA cycle, which are roughly consistent. In the applications, we prioritized the use of in vivo results for enzyme catalytic rates, and use in vitro data as a substitute when there were gaps.

Appendix 6.3 Comparison with existing models that illustrate experimental results

For the coarse-grained model described in **Appendix 2**, the normalized stoichiometric influx of a Group A carbon source is given by:

$$J_{in}^{(\mathrm{N})} \equiv J_A^{(\mathrm{N})} = \phi_A \cdot \kappa_A . \tag{S136}$$

Combined with the first equation in **Eq. S28** and **Eq. S30**, we obtain:

$$J_{in}^{(\mathrm{N})} - \vartheta \cdot \lambda = \frac{J_r^{(\mathrm{E})}}{\beta_r^{(A)}} + \frac{J_f^{(\mathrm{E})}}{\beta_f^{(A)}}, \tag{S137}$$

where $\vartheta = \eta_{a1} + \eta_c + (\eta_{a2} + \eta_b + \eta_d)/2$. Evidently, $\beta_r^{(A)}$, $\beta_f^{(A)}$ and ϑ are constant parameters. In this subsection, we highlight the major differences between our model presented in **Appendix 2** and existing models that illustrate the growth rate dependence of fermentation flux in the standard picture of overflow metabolism (Basan et al., 2015; Holms, 1996; Meyer et al., 1984; Nanchen et al., 2006).

Based on the modeling principles rather than the detailed mechanisms, there are two major classes of existing models that can illustrate experimental results. Both classes of models regard the proteome efficiencies ε_r and ε_f as constants, with $\varepsilon_f > \varepsilon_r$ if used, or follow functionally equivalent propositions. However, in our model, ε_r and ε_f are both functions of κ_A, which vary significantly upon nutrient perturbation, with $\varepsilon_r(\kappa_A \to 0) > \varepsilon_f(\kappa_A \to 0)$ and $\varepsilon_r\left(\kappa_A^{\max}\right) < \varepsilon_f\left(\kappa_A^{\max}\right)$ (see Eqs. S38, S40–S41). Furthermore, there are significant differences in the modeling and optimization principles, as listed below.

The first class of models (Chen and Nielsen, 2019; Majewski and Domach, 1990; Niebel et al., 2019; Shlomi et al., 2011; Varma and Palsson, 1994; Vazquez et al., 2010; Vazquez and Oltvai, 2016; Zhuang et al., 2011) optimize the ratio of biomass outflow to carbon influx $\lambda / J_{in}^{(\mathrm{N})}$, either to optimize the growth rate for a given carbon influx or to minimize the carbon influx for a given growth rate. Since respiration is far more efficient than fermentation in terms of

energy biogenesis per unit carbon, to optimize the ratio $\lambda/J_{in}^{(\mathrm{N})}$, cells would preferentially use respiration when the carbon influx is small. As carbon influx increases above a certain threshold, factors such as proteome allocation direct cells toward fermentation in a threshold-linear response, since they consider $\varepsilon_f > \varepsilon_r$. Our model is significantly different from this class of models in the optimization principle, as we purely optimize the cell growth rate for a given nutrient condition, without imposing a special constraint on the carbon influx.

The second class of models, represented by Basan *et al.* (Basan et al., 2015), also adopt the optimization of $\lambda/J_{in}^{(\mathrm{N})}$ in the interpretation of their model results. However, the growth rate dependence of fermentation flux was derived prior to the application of growth rate optimization (although it can be derived by optimizing $\lambda/J_{in}^{(\mathrm{N})}$). In fact, Eqs. S29 and S137 in our model are very similar in form to those in Basan *et al.* (Basan et al., 2015), yet there are critical differences, which we list below. In Eq. S29, by regarding $J_r^{(\mathrm{E})}$ and $J_f^{(\mathrm{E})}$ as the two variables in a system of linear equations, we obtain the following expressions:

$$\begin{cases} J_r^{(\mathrm{E})} = \dfrac{\phi_{\max} - \left(\psi + \varphi/\varepsilon_f\right)\cdot\lambda}{1/\varepsilon_r - 1/\varepsilon_f}, \\ J_f^{(\mathrm{E})} = \dfrac{\left(\psi + \varphi/\varepsilon_r\right)\cdot\lambda - \phi_{\max}}{1/\varepsilon_r - 1/\varepsilon_f}. \end{cases} \tag{S138}$$

In Basan *et al.* (Basan et al., 2015), Eq. S138 is considered to be the relation between $J_{r/f}^{(\mathrm{E})}$ and λ upon nutrient (and thus $J_{in}^{(\mathrm{N})}$) perturbation, while ε_r and ε_f are regarded as constants throughout the perturbation. By contrast, in our model, Eq. S138 serves as a constraint under a given nutrient condition with fixed κ_A, and is not relevant to nutrient perturbation. For wild-type strains, if $\varepsilon_r(\kappa_A) > \varepsilon_f(\kappa_A)$ (or vice versa), then the solution for optimal growth is $J_r^{(\mathrm{E})}(\kappa_A) = \varphi\cdot\lambda(\kappa_A)$ and $\sigma_{k_i^{\mathrm{cat}}}/\mu_{k_i^{\mathrm{cat}}}$, with $\mathcal{N}'\left(x;\mu_{k_i^{\mathrm{cat}}},\sigma^2_{k_i^{\mathrm{cat}}}\right)$. This solution, which satisfies Eq. S138, corresponds to a point rather than a line in the relation between growth rate λ and normalized energy flux $\mathcal{N}\left(\mu_{k_i^{\mathrm{cat}}},\sigma^2_{k_i^{\mathrm{cat}}}\right)$ upon κ_A perturbation.

Appendix 7 Probability density functions of variables and parameters

Appendix 7.1 Probability density function of κ_i

Enzyme catalysis is crucial for the survival of living organisms, as it significantly accelerates biochemical reactions by reducing the energy barrier between the substrate and product (Nelson et al., 2008). However, the maximal turnover rate of enzymes, k_{cat}, varies notably between in vivo and in vitro measurements (Davidi et al., 2016). Recent studies suggest that differences in the aquatic medium are the primary cause of this variation (Davidi et al., 2016; García-Contreras

et al., 2012). In particular, potassium and phosphate concentrations have a significant influence on k_{cat} (García-Contreras et al., 2012), and these concentrations exhibit some degree of variation among cell populations under intracellular conditions (García-Contreras et al., 2012). For simplicity, we assume that the turnover rate of each enzyme E_i, $1/k_i^{cat}$, follows a Gaussian distribution $J_f^{(E)}(\kappa_A)=0$ with $\lambda(\kappa_A)=\frac{\varepsilon_r(\kappa_A)\cdot\phi_{max}}{\varphi+\varepsilon_r(\kappa_A)\cdot\psi(\kappa_A)}$ among cells (representing extrinsic noise (Elowitz et al., 2002), denoted as χ_{ext}). The probability density function of $J_{r/f}^{(E)}$ is then given by:

$$k_i^{cat}\sim\mathcal{N}'\left(x,\mu_{k_i^{cat}},\sigma^2_{k_i^{cat}}\right)=\begin{cases}\frac{1}{\sigma_{k_i^{cat}}\sqrt{2\pi}}e^{-\frac{1}{2}\left(\frac{x-\mu_{k_i^{cat}}}{\sigma_{k_i^{cat}}}\right)^2}, & x\geq 0.\\ 0, & x<0.\end{cases} \tag{S139}$$

When the CV of the k_i^{cat} distribution (i.e., $\mathcal{N}\left(\mu_{k_i^{cat}},\sigma^2_{k_i^{cat}}\right)$) is less than 1/3, $k_i^{cat}>0$ is almost identical to k_i^{cat}. In this case, k_i^{cat} follows the positive inverse of Gaussian (IOG) distribution, and the probability density function is:

$$\mathrm{IOG}\left(x,\mu_{1/k_i^{cat}},\zeta_{1/k_i^{cat}}\right)=\begin{cases}\sqrt{\frac{\zeta_{1/k_i^{cat}}}{2\pi x^4}}\exp\left(-\frac{1}{2}\frac{\zeta_{1/k_i^{cat}}\left(x-\mu_{1/k_i^{cat}}\right)^2}{x^2\mu^2_{1/k_i^{cat}}}\right), & x\geq 0,\\ 0, & x<0,\end{cases} \tag{S140}$$

where $\zeta_{1/k_i^{cat}}=1/\sigma^2_{k_i^{cat}}$ is the shape parameter, and $\mu_{1/k_i^{cat}}=1/\mu_{k_i^{cat}}$ is the mean.

Meanwhile, due to the stochastic nature of biochemical reactions, we apply Gillespie's chemical Langevin equation (Gillespie, 2000) to account for intrinsic noise (Elowitz et al., 2002) (denoted as χ_{int}). For cell size regulation of *E. coli* within a cell cycle, the cell mass at the initiation of DNA replication per chromosome origin remains constant (Donachie, 1968). Thus, the time required for enzyme E_i to complete a catalytic job (with a timescale of $1/k_i^{cat}$) can be approximated as the first passage time of a stochastic process, with

$$\begin{cases}X_i(t=0)=0,\\ dX_i/dt=\alpha_i+\sqrt{\alpha_i}\Gamma_i(t),\\ T_\Theta=\inf\left\{t>0\mid X_i(t)=\Theta\right\}.\end{cases} \tag{S141}$$

Here $\alpha_i \equiv k_i^{\text{cat}} \cdot \Theta$, where Θ is proportional to the cell volume, and $\Gamma_i(t)$ represents independent, temporally uncorrelated Gaussian white noise. Then, for a given value of k_i^{cat}, the first passage time T_Γ follows an Inverse Gaussian (IG) distribution (Folks and Chhikara, 1978):

$$\mathrm{IG}\left(x,\mu'_{1/k_i^{\text{cat}}},\zeta'_{1/k_i^{\text{cat}}}\right)=\begin{cases}\sqrt{\dfrac{\zeta'_{1/k_i^{\text{cat}}}}{2\pi x^3}}\exp\left(-\dfrac{1}{2}\dfrac{\zeta'_{1/k_i^{\text{cat}}}\left(x-\mu'_{1/k_i^{\text{cat}}}\right)^2}{x\mu'^2_{1/k_i^{\text{cat}}}}\right), & x\geq 0,\\ 0, & x<0,\end{cases} \tag{S142}$$

where $\zeta'_{1/k_i^{\text{cat}}}=\Theta/k_i^{\text{cat}}$ is the shape parameter, and $\mu'_{1/k_i^{\text{cat}}}=1/k_i^{\text{cat}}$ represents the mean. The variance of this distribution is $\sigma'^2_{1/k_{cat}^i}\equiv\mu'^3_{1/k_i^{\text{cat}}}/\zeta'_{1/k_i^{\text{cat}}}=1/\left[\Theta\cdot\left(k_i^{\text{cat}}\right)^2\right]$. Thus, we can obtain the CV:

$$\sigma'_{1/k_i^{\text{cat}}}/\mu'_{1/k_i^{\text{cat}}}=\Theta^{-\frac{1}{2}}, \tag{S143}$$

which is inversely proportional to the square root of cell volume. Evidently, the intrinsic and extrinsic noise make orthogonal contributions to the total noise (Elowitz et al., 2002) (denoted as χ_{tot}):

$$\eta_{\text{tot}}^2=\eta_{\text{int}}^2+\eta_{\text{ext}}^2. \tag{S144}$$

In fact, when the CV is small (i.e., CV≪1), both the IOG and IG distributions converge into Gaussian distributions (**Appendix-fig. 4**). In the back-of-the-envelope calculations, we approximate x in all denominator terms of IOG (x, μ, ζ) and IG (x, μ, ζ) as μ (since CV≪1). Then, both the IOG and IG distributions can be approximated as follows:

$$\mathrm{IOG}\left(x;\mu_{1/k_i^{\text{cat}}},\zeta_{1/k_i^{\text{cat}}}\right)\xrightarrow{\text{CV}\ll 1}\mathcal{N}\left(\mu_{1/k_i^{\text{cat}}},\sigma^2_{1/k_i^{\text{cat}}}\right), \tag{S145}$$

with a variance of $\sigma^2_{1/k_i^{\text{cat}}}=\mu^4_{1/k_i^{\text{cat}}}/\zeta_{1/k_i^{\text{cat}}}$, and

$$\mathrm{IG}\left(x;\mu'_{1/k_i^{\text{cat}}},\zeta'_{1/k_i^{\text{cat}}}\right)\xrightarrow{\text{CV}\ll 1}\mathcal{N}\left(\mu'_{1/k_i^{\text{cat}}},\sigma'^2_{1/k_i^{\text{cat}}}\right), \tag{S146}$$

with a variance of $\sigma'^2_{1/k_i^{\text{cat}}}=\mu'^3_{1/k_i^{\text{cat}}}/\zeta'_{1/k_i^{\text{cat}}}$. Rigorously, we show below that IG (x, μ, ζ) shrinks to be $N(\mu, \mu/\zeta)$ when the CV is small. For the IG distribution, the characteristic function of the variable x is given by (Folks and Chhikara, 1978; Van Kampen, 1992):

$$G(k)=\int_{-\infty}^{\infty}e^{ikx}\cdot\mathrm{IG}\left(x;\mu,\zeta\right)dx=\exp\left\{\frac{\zeta}{\mu}\left[1-\sqrt{1-\frac{2i\mu^2k}{\zeta}}\right]\right\}, \tag{S147}$$

and therefore,

$$\mathrm{IG}\left(x;\mu,\zeta\right)=\frac{1}{2\pi}\int_{-\infty}^{\infty}e^{-\mathrm{i}kx}\cdot G\left(k\right)dk\,. \tag{S148}$$

When the variance $\sigma^2=\mu^3/\zeta$ is very small, we essentially require $2\mu^2k/\zeta=2\sigma^2k/\mu\ll 1$, and then $\sqrt{1-\frac{2\mathrm{i}\mu^2k}{\zeta}}\approx 1-\frac{\mu^2}{\zeta}k\mathrm{i}+\frac{\mu^4}{2\zeta^2}k^2$. Thus,

$$\begin{cases} G\left(k\right)\approx\exp\left(\mu k\mathrm{i}-\frac{\mu^3}{2\zeta}k^2\right), \\ \mathrm{IG}\left(x;\mu,\zeta\right)\approx\sqrt{\frac{\zeta}{2\pi\mu^3}}e^{-\frac{\zeta\left(x-\mu\right)^2}{2\mu^3}}=\mathcal{N}\left(\mu,\mu^3/\zeta\right). \end{cases} \tag{S149}$$

This leads to:

$$\lim_{\sigma\to 0}\mathrm{IG}\left(x;\mu,\zeta\right)=\mathcal{N}\left(\mu,\mu^3/\zeta\right). \tag{S150}$$

In fact, intrinsic noise does affect the short-term measurement of enzyme catalytic rate and growth rate at the single-cell level. However, its contribution in the long term is averaged out and thus becomes negligible. For simplicity, we approximate $\chi_{\mathrm{tot}}\approx\chi_{\mathrm{ext}}$. Combined with Eqs. S145–S146, it is straightforward to verify that $1/k_i^{\mathrm{cat}}$ shares roughly the same CV as k_i^{cat}:

$$\sigma_{1/k_i^{\mathrm{cat}}}/\mu_{1/k_i^{\mathrm{cat}}}=\sigma_{k_i^{\mathrm{cat}}}/\mu_{k_i^{\mathrm{cat}}}\,. \tag{S151}$$

For convenience, in the model analysis, we approximate both IOG and IG distributions as Gaussian distributions. Then, all $1/k_i^{\mathrm{cat}}$ are independent, normally distributed random variables following Gaussian distributions:

$$1/k_i^{\mathrm{cat}}\sim\mathcal{N}\left(\mu_{1/k_i^{\mathrm{cat}}},\sigma^2_{1/k_i^{\mathrm{cat}}}\right). \tag{S152}$$

Using the properties of Gaussian distributions, for a series of constant real numbers γ_i, the summation of σ_{κ_i}, which we define as σ_{1/κ_i}, follows a Gaussian distribution (Van Kampen, 1992):

$$\Xi\sim\mathcal{N}\left(\mu_\Xi,\sigma_\Xi^2\right), \tag{S153}$$

with $\kappa_A^{(C)}$ and $\mu_{\lambda_{r/f}}$. The relation between κ_i and $\sigma_{\lambda_{r/f}}$ is shown in Eq. S12. To optimize cell growth rate, each κ_i of the intermediate nodes satisfies Eq. S20, while κ_A satisfies Eq. S27. Thus, for a given nutrient condition ([A] is fixed), all the ratios $\gamma_i / k_i^{\text{cat}}$ are constants. Combined with Eqs. S139, S145–S146, and S152, the distributions of all κ_i and $1/\kappa_i$ can be approximated as Gaussian distributions:

$$\begin{cases} \kappa_i \sim \mathcal{N}\left(\mu_{\kappa_i}, \sigma_{\kappa_i}^2\right), \\ 1/\kappa_i \sim \mathcal{N}\left(\mu_{1/\kappa_i}, \sigma_{1/\kappa_i}^2\right), \end{cases} \tag{S154}$$

where $\Xi \equiv \sum_{i=1}^{n} \gamma_i / k_{cat}^i$ and $\mu_\Xi = \sum_{i=1}^{n} \gamma_i \mu_{1/k_i^{\text{cat}}}$ are the means of κ_i and $1/\kappa_i$, and $\sigma_\Xi^2 = \sum_{i=1}^{n} \left(\gamma_i \sigma_{1/k_i^{\text{cat}}}\right)^2$ and k_i^{cat} are their standard deviations. Using the properties of Gaussian distributions, combined with Eq. S31, S32, S36, S42–S43, S145–S146 and S153, ε_r, ε_f, ψ, λ_r, λ_f, $k_i^{\text{cat}} / \kappa_i$ and λ_C also roughly follow Gaussian distributions.

Appendix 7.2 Probability density function of the growth rate λ

From Appendix 7.1, we note that λ_r and λ_f (see Eq. S36) roughly follow Gaussian distributions, with

$$\begin{cases} \lambda_r \sim \mathcal{N}\left(\mu_{\lambda_r}, \sigma_{\lambda_r}^2\right), \\ \lambda_f \sim \mathcal{N}\left(\mu_{\lambda_f}, \sigma_{\lambda_f}^2\right), \end{cases} \tag{S155}$$

where μ_{κ_i} and μ_{1/κ_i} represent the mean and standard deviation, respectively. We further assume that the correlation between λ_r and λ_f is ρ_{rf}. From Eq. S36, we see that the growth rate λ takes the maximum of λ_r and λ_f, i.e.,

$$\lambda = \max\left(\lambda_r, \lambda_f\right). \tag{S156}$$

Then, the cumulative distribution function of λ is $P(\lambda \le x) = \int_{-\infty}^{x} \int_{-\infty}^{x} f(x_1, x_2)\, dx_1 dx_2$, where

$$f(x_1, x_2) = \frac{\left(1-\rho_{rf}^2\right)^{-\frac{1}{2}}}{2\pi \sigma_{\lambda_r} \sigma_{\lambda_f}} \exp\left(-\frac{1}{2\left(1-\rho_{rf}^2\right)} \left[\left(\frac{x_1 - \mu_{\lambda_r}}{\sigma_{\lambda_r}}\right)^2 - 2\rho_{rf} \left(\frac{x_1 - \mu_{\lambda_r}}{\sigma_{\lambda_r}}\right)\left(\frac{x_2 - \mu_{\lambda_f}}{\sigma_{\lambda_f}}\right) + \left(\frac{x_2 - \mu_{\lambda_f}}{\sigma_{\lambda_f}}\right)^2 \right] \right).$$

Thus, the probability density function of the growth rate A is given by:

$$f_{\lambda}(x)=\frac{1}{2\sqrt{2\pi}\sigma_{\lambda_r}}e^{-\frac{1}{2}\left(\frac{x-\mu_{\lambda_r}}{\sigma_{\lambda_r}}\right)^2}\left[\operatorname{erf}\left(\frac{\left(x-\mu_{\lambda_f}\right)\sigma_{\lambda_r}-\rho_{rf}\sigma_{\lambda_f}\left(x-\mu_{\lambda_r}\right)}{\sigma_{\lambda_r}\sigma_{\lambda_f}\sqrt{2\left(1-\rho_{rf}{}^2\right)}}\right)+1\right]+\frac{1}{2\sqrt{2\pi}\sigma_{\lambda_f}}e^{-\frac{1}{2}\left(\frac{x-\mu_{\lambda_f}}{\sigma_{\lambda_f}}\right)^2}\left[\operatorname{erf}\left(\frac{\left(x-\mu_{\lambda_r}\right)\sigma_{\lambda_f}-\rho_{rf}\sigma_{\lambda_r}\left(x-\mu_{\lambda_f}\right)}{\sigma_{\lambda_r}\sigma_{\lambda_f}\sqrt{2\left(1-\rho_{rf}{}^2\right)}}\right)+1\right]. \tag{S157}$$

In **Appendix-fig. 2B**, we show that Eq. **S157** quantitatively matches the experimental data for *E. coli* under the relevant conditions.

Appendix 8 Model comparison with experiments on *E. coli*

Appendix 8.1 Flux comparison with experiments on *E. coli*

In **Appendix 6.2**, we see that the values of $J_f^{(\mathrm{N})}$ and $J_r^{(\mathrm{N})}$ are required to calculate the in vivo enzyme catalytic rates of the intermediate nodes. Here, we use J_{acetate} and $J_{\mathrm{CO}_2,r}$ to represent the stoichiometric fluxes of acetate from the fermentation pathway and CO2 from the respiration pathway, respectively. Combined with the stoichiometric coefficients of both pathways, we have:

$$\begin{cases} J_{\mathrm{acetate}}=J_f, \\ J_{\mathrm{CO}_2,r}=3\cdot J_r. \end{cases} \tag{S158}$$

By further combining with Eqs. **S16**–**S17**, we get:

$$\begin{cases} J_f^{(\mathrm{N})}=J_{\mathrm{acetate}}\cdot\dfrac{m_{\mathrm{carbon}}}{M_{\mathrm{carbon}}}\cdot\left[\sum_i r_i/N_{\mathrm{EP}_i}^{\mathrm{carbon}}\right]^{-1}, \\ J_r^{(\mathrm{N})}=\dfrac{1}{3}\cdot J_{\mathrm{CO}_2,r}\cdot\dfrac{m_{\mathrm{carbon}}}{M_{\mathrm{carbon}}}\cdot\left[\sum_i r_i/N_{\mathrm{EP}_i}^{\mathrm{carbon}}\right]^{-1}. \end{cases} \tag{S159}$$

In fact, the values of J_{acetate} and $J_{\mathrm{CO}_2,r}$ scale with the mass of the "big cell", which increases over time. In experiments, the measurable fluxes are typically expressed in the unit of mM/OD_{600}/h (Basan et al., 2015). Thus, we define $J_{\mathrm{acetate}}^{(\mathrm{M})}$ and $J_{\mathrm{CO}_2,r}^{(\mathrm{M})}$ as the fluxes of J_{acetate} and $J_{\mathrm{CO}_2,r}$ (per biomass) in the unit of mM/OD_{600}/h, respectively. The superscript "(M)" represents the measurable flux in this unit. For *E. coli*, we use the following biochemical data collected from published literature: 1 OD_{600} roughly corresponds to 6×10^8 cells/mL (Stevenson et al., 2016), the average mass of a cell is 1pg (Milo and Phillips, 2015), the biomass percentage of the cell weight is 30% (Neidhardt et al., 1990), the molar mass of carbon is 12g (Nelson et al.,

2008), r_{carbon} = 0.48 (Neidhardt et al., 1990) and $r_{protein}$ = 0.55 (Neidhardt et al., 1990). Combined with the values of r_i (see Appendix 1.2) and $N_{EP_i}^{carbon}$, where $\xi_3^{(i)}$, $\phi_3^{(i)}$, $\kappa_3^{(i)}$, $J_3^{(i)} = J_3$ and $\kappa_3^{(i)}$ (Nelson et al., 2008), we have:

$$\begin{cases} J_f^{(N)} \approx J_{acetate}^{(M)}/2, \\ J_r^{(N)} \approx J_{CO_2,r}^{(M)}/6. \end{cases} \tag{S160}$$

From Eq. S18, we obtain the values of η_i for each precursor pool: η_{a1} = 0.15, η_{a2} = 0.30, η_b = 0.35, η_c = 0.09, and η_d = 0.11. Still, the value of η_E is required to compare the growth rate dependence of fermentation/respiration fluxes between model results and experiments, which we will specify in Appendix 8.2.

Appendix 8.2 Model parameter settings using experimental data of *E. coli*

We have collected biochemical data for *E. coli*, as shown in **Appendix-tables 1**–**2**, to set the model parameters. This includes the molecular weight (MW) and in vitro k_{cat} values of the catalytic enzymes, as well as the proteome and flux data used to calculate the in vivo turnover numbers. To reduce measurement noise, we take the average rather than the maximum value of in vivo k_{cat} from calculations using data from four cultures (see **Appendix-table 2**). Here, we prioritize the use of in vivo k_{cat} wherever applicable unless there is a gap in the in vivo data (see **Appendix-table 1**).

Note that our models are coarse grained. For example, the flux J_3 shown in **Fig. 1B** actually corresponds to three different reactions in the metabolic network (see **Fig. 1A** and **Appendix-table 1**), which we label as $\varepsilon_{r/f}\left(\kappa_A^{(C)}\right) = 122\ \left(h^{-1}\right)$ (i = 1, 2, 3). For each $\varepsilon_r\left(\kappa_{glucose}^{(ST)}\right) < \varepsilon_f\left(\kappa_{glucose}^{(ST)}\right)$, there are corresponding variables/parameters of $\varepsilon_r\left(\kappa_{lactose}^{(ST)}\right) < \varepsilon_f\left(\kappa_{lactose}^{(ST)}\right)$, $N_{EP_{a1}}^{carbon} = 6$, $N_{EP_{a2}}^{carbon} = 3$, $N_{EP_b}^{carbon} = 3$ satisfying Eqs. **S8**, **S9** and **S12**, Evidently, $N_{EP_c}^{carbon} = 5$ (i = 1, 2, 3), and it is straightforward to derive the following relation between $N_{EP_d}^{carbon} = 4$ and κ_3:

$$1/\kappa_3 = \sum_{i=1}^{3} 1/\kappa_3^{(i)}. \tag{S161}$$

In fact, Eq. **S161** can be generalized to determine the values of other κ_i in the coarse-grained models combined with the biochemical data. For the coarse-grained model of Group A carbon source utilization shown in **Fig. 1B**, we have the values for parameters κ_i (i = 1, ..., 6), and then

$J_3^{(i)}$. Evidently, $J_3^{(i)}$, $\Phi_3^{(i)}$, and thus $\varepsilon_r\left(\kappa_A^{\max}\right) < \varepsilon_f\left(\kappa_A^{\max}\right)$. For pyruvate, we have $\mu_{\lambda_C^{(\mathrm{py})}} = 0.67$ (see Eqs. **S43** and **S101**), and it is easy to check that $\sigma_{\lambda_C^{(\mathrm{py})}} = 0.10\mu_{\lambda_C^{(\mathrm{py})}}$.

For the remaining model parameters, note that we have classified the inactive ribosomal-affiliated proteins into the Q-class, and then $\varphi_{\max}$ = 48% (Scott et al., 2010). The value of κ_t is obtainable from experiments: the translation speed is 20.1aa/s (Scott et al., 2010), with 7336 amino acids per ribosome (Neidhardt, 1996) and $\varsigma \approx 1.67$ (Neidhardt, 1996; Scott et al., 2010) (see Appendix 1.1), hence κ_t = 1/610 (s^{-1}). However, there are insufficient data to determine the values of κ_i (i = a1, a2, b, c, d) for the metabolites between the entry point metabolites shown in **Fig. 1A** to the precursor pools. These processes involves many steps, so these values are expected to be quite large. Here, we combine the contributions of κ_t and κ_i (i = a1, a2, b, c, d) by defining a composite parameter:

$$\Omega \equiv 1/\kappa_t + \sum_i^{a1,a2,b,c,d} \eta_i/\kappa_i \,. \tag{S162}$$

We proceed to estimate the values of Ω and ϕ using experimental data (Basan et al., 2015) for wild-type strains on the $\varepsilon_{r/f}^{(\mathrm{py})}\left(\kappa_{\mathrm{py}}^{(\mathrm{C})}\right) = \varepsilon_{r/f}\left(\kappa_A^{(\mathrm{C})}\right) = 122\ \left(\mathrm{h}^{-1}\right)$ relation (**Fig. 1C**), and then all the remaining model parameters are set accordingly.

For the case of w_0 = 0, where all k_{cat} values follow a Gaussian distribution with an extrinsic noise of 25% CV (which is the general setting we use unless otherwise specified), we have ϕ = 10.8 and Ω = 1345 (s). Accordingly, we obtain η_{E} = 14.78, $\varepsilon_r\left(\kappa_{\mathrm{py}}^{(\mathrm{ST})}\right) < \varepsilon_f\left(\kappa_{\mathrm{py}}^{(\mathrm{ST})}\right)$ (h^{-1}), and $J_{\mathrm{acetate}}^{(\mathrm{M})}$-$\lambda$, where the CV of the extrinsic noise for Ω is estimated using the averaged CV of other κ_i. For the translation inhibition effect of Cm, we estimate the values for ι as $\mu_{\lambda_C} = 0.92$, $\sigma_{\lambda_C} = 0.12\mu_{\lambda_C}$, and $\iota_{w_0=0}^{(2\,\mu\mathrm{m\ Cm})} = 1.15$, where the superscript stands for the concentration of Cm, and the subscript represents the choice of w_0.

For pyruvate, with the value of η_{E}, we get ϕ_{py} = 14.82. However, there is still a lack of proteome data to determine the value of κ_9, which involves many steps in the metabolic network and thus can be considerably large. Here we define another composite parameter, $\Omega'_{\mathrm{Gg}} \equiv (\eta_b + \eta_c)/\kappa_8 + \eta_{a1}/\kappa_9$, and estimate its value as Ω'_{Gg} = 690 (s) from growth rate data for *E. coli* measured under the relevant nutrient conditions (Basan et al., 2015), where the subscript "Gg" stands for glucogenesis. Then, $\iota_{w_0=0}^{(4\,\mu\mathrm{m\ Cm})} = 2.33$ (h^{-1}), and $\iota_{w_0=0}^{(8\,\mu\mathrm{m\ Cm})} = 6.25$, where the same CV of extrinsic noise for Ω applies to Ω'_{Gg}.

For the case of a Group A carbon source mixed with 21 amino acids (21AA, with saturated concentrations), we have $\phi_{21\mathrm{AA}}$ = 14.2. Comparing Eq. S32 with Eq. S112, the parameter Ω should change to $\Omega_{21\mathrm{AA}} \equiv 1/\kappa_t + \eta_{a1}/\kappa_{a1} + \sum_i^{a2,b,c,d} \eta_i/\kappa_i^{(21\mathrm{AA})}$. Obviously, $1/\kappa_t < \Omega_{21\mathrm{AA}} < \Omega$, and

we estimate Ω_{21AA} = 1000 (s) from the growth rate data for *E. coli* measured under the relevant nutrient conditions (Wallden et al., 2016). Then, we have $\iota_{w_0=2.5}^{(8\mu m\ Cm)} = 5.40$ (h^{-1}), and $\lambda_r^{(21AA)}$.

For the case of a Group A carbon source mixed with 7 amino acids (7AA: His, Iso, Leu, Lys, Met, Phe, and Val), similar to the roles of ϕ_{21AA} and Ω_{21AA}, we define ϕ_{7AA} and Ω_{7AA}. Using the mass fraction of the 7AA combined with Eq. S18, we have ϕ_{7AA} = 11.6. For the value of Ω_{7AA}, evidently, $\Omega_{21AA} < \Omega_{7AA} < \Omega$, and we estimate Ω_{7AA} = 1215 (s) from growth rate data for *E. coli* measured under the relevant culture media (Basan et al., 2015). Then, $\lambda_f^{(21AA)}$ (h^{-1}), and $\mu_{\lambda_r^{(21AA)}}$.

For the case of w_0 = 2.5 (h^{-1}), we have ϕ = 8.3, and thus η_E = 12.28, while other parameters such as Ω, $\mu_{\lambda_f^{(21AA)}}$ and $\sigma_{\lambda_r^{(21AA)}}$ remain the same as for w_0 = 0. Nevertheless, the values for ι under translation inhibition by Cm are influenced by the choice of w_0, where the values of ι change to $\sigma_{\lambda_f^{(21AA)}}$, $\lambda_{\text{glucose}}^{(21AA)}$, and $\mu_{\lambda_{\text{glucose},r}^{(21AA)}} = 1.34\ \left(h^{-1}\right)$.

From Appendix 7.1–7.2, combined with Eq. S114, the distributions of $\mu_{\lambda_{\text{glucose},f}^{(21AA)}} = 1.46\left(h^{-1}\right)$ and $\mu_{\lambda_C^{(21AA)}} = 1.13$ can be approximated by Gaussian distributions:

$$\begin{cases} \lambda_r^{(21AA)} \sim \mathcal{N}\left(\mu_{\lambda_r^{(21AA)}}, \sigma^2_{\lambda_r^{(21AA)}}\right), \\ \lambda_f^{(21AA)} \sim \mathcal{N}\left(\mu_{\lambda_f^{(21AA)}}, \sigma^2_{\lambda_f^{(21AA)}}\right), \end{cases} \tag{S163}$$

where $\sigma_{\lambda_C^{(21AA)}} = 0.12\mu_{\lambda_C^{(21AA)}}$ and $\mu_{\lambda_C^{(7AA)}} = 0.98$ stand for the mean values, while $\sigma_{\lambda_C^{(7AA)}} = 0.12\mu_{\lambda_C^{(7AA)}}$ and μ_{λ_C} represent the standard deviations. For the case of glucose mixed with 21AA (labeled as "Glucose+21AA"), the distribution of the growth rate σ_{λ_C} follows Eq. S157. With Ω_{21AA} = 1000 (s) , we have $\iota_{w_0=2.5}^{(2\mu m\ Cm)} = 1.05$, $\iota_{w_0=2.5}^{(4\mu m\ Cm)} = 2.00$ (both definitions follow Eq. S163), and $\rho_{rf} \approx 1.0$ (obtained from numerical results).

For the case of succinate mixed with 21AA (labeled as "Succinate+21AA"), the respiration pathway is always more efficient since succinate lies within the TCA cycle. Thus, the cell growth rate (defined as $\lambda_{\text{succinate}}^{(21AA)}$) would take the value of the respiration one and follows a Gaussian distribution:

$$\lambda_{\text{succinate}}^{(21AA)} \sim \mathcal{N}\left(\mu_{\lambda_{\text{succinate}}^{(21AA)}}, \sigma^2_{\lambda_{\text{succinate}}^{(21AA)}}\right). \tag{S164}$$

For the case where acetate is the sole carbon source, the cells exclusively use the respiration pathway, and the growth rate (defined as λ_{acetate}) follows a Gaussian distribution:

$$\lambda_{\text{acetate}} \sim \mathcal{N}\left(\mu_{\lambda_{\text{acetate}}}, \sigma^2_{\lambda_{\text{acetate}}}\right). \tag{S165}$$

Using the measured growth rate data (Wallden et al., 2016), we estimate $\mu_{\lambda^{(21AA)}_{\text{succinate}}} = 0.67\ \left(\text{h}^{-1}\right)$ and $\mu_{\lambda_{\text{acetate}}} = 0.253\ \left(\text{h}^{-1}\right)$. To illustrate the distribution of growth rates $\lambda^{(21AA)}_{\text{glucose}}$, $\lambda^{(21AA)}_{\text{succinate}}$ and shown in **Appendix-fig. 2B**, if no other source of noise existed, extrinsic noise with a CV of 40% would be required for each k_{cat} value. Then, $\sigma_{\lambda^{(21AA)}_{\text{glucose},\,r}} \approx 0.21\mu_{\lambda^{(21AA)}_{\text{glucose},\,r}}$, $\sigma_{\lambda^{(21AA)}_{\text{glucose},\,f}} \approx 0.23\mu_{\lambda^{(21AA)}_{\text{glucose},\,f}}$, $\sigma_{\lambda^{(21AA)}_{\text{succinate}}} = 0.22\mu_{\lambda^{(21AA)}_{\text{succinate}}}$, and $\sigma_{\lambda_{\text{acetate}}} = 0.22\mu_{\lambda_{\text{acetate}}}$. Allowing for the possibility that intrinsic noise may also play a non-negligible role in the observed single-cell growth rate (which is not a longterm average), we still use extrinsic noise with a CV of 25% for the model results of *E.coli*, except for those shown in **Appendix-fig. 2B**.

Appendix 9 Explanation of the Crabtree effect in yeast and the Warburg effect in tumors

Our model, along with the analysis presented in **Appendix 2**, can be extended with modifications to explain the Crabtree effect in yeast and the Warburg effect in tumors. In both cases, the optimization objective remains maximizing the cell growth rate. Consequently, yeast and tumor cells use the most efficient pathway for ATP production at the single-cell level.

For model applications in yeast or tumor cell metabolism, the fermentation flux shifts from acetate secretion to ethanol and lactate secretion, respectively (see **Appendix-fig. 5A-B**). The respiration and biomass generation pathways remain largely similar to those of *E. coli*, except that the biochemical reactions within the TCA cycle and respiratory chain occur in the mitochondria (see **Appendix-fig. 5C-D**). This leads to an increased enzyme cost for the respiration pathway due to energy currency exchanges between NADH or $FADH_2$ and ATP in the mitochondria. The coarse-grained models for Group A carbon source utilization in yeast and mammalian cells are shown in **Appendix-fig. 5E-F**, where M_3 represents pyruvate. In yeast and mammalian cells, the stoichiometric coefficients for ATP production (i.e., β_i) are identical to each other but differ from those of *E. coli* (see **Fig. 1B** and **Appendix-fig. 5C-D**), with $\beta_1 = 5$, $\beta_2 = 1$, $\beta_3 = 5$, $\beta_4 = 7.5$, $\beta_6 = -2.5$, and $\beta_{a1} = 5$ (Nelson et al., 2008). Hence, the stoichiometric coefficients of ATP production per glucose in each pathway are $\beta_r^{(A)} = 32$ and $\beta_f^{(A)} = 2$, respectively, where

$$\beta_r^{(A)} = \beta_1 + 2\left(\beta_2 + \beta_3 + \beta_4\right) \text{ and } \beta_f^{(A)} = \beta_1 + 2\left(\beta_2 + \beta_6\right).$$

The impact of maintenance energy in yeast and tumor cells is significantly higher than that in *E. coli* (Locasale and Cantley, 2010). Therefore, Eq. S25 changes to (see Eq. S59):

$$J_{\text{E}} = r_{\text{E}} \cdot J_{\text{BM}} + w_0 \cdot \frac{M_{\text{carbon}}}{m_0}, \tag{S166}$$

where w_0 is the aforementioned maintenance energy coefficient. Thus, we have (see Eq. S60):

$$J_{\mathrm{E}}^{(\mathrm{N})} = \eta_{\mathrm{E}} \cdot \lambda + w_0 . \tag{S167}$$

To account for the protein cost of energy currency exchanges in the mitochondria, we introduce φ_{MT} and κ_{MT} to represent the proteomic mass fraction of the enzymes and the effective substrate quality of related metabolites in the mitochondria, respectively. Note that the energy currency exchanges between NADH or FADH2 and ATP only occur during respiration, as there is no net NADH or FADH2 generation during fermentation (see **Appendix-fig. 5C-D**). Combined with Eq. **S167**, Eq. **S25** changes to:

$$\begin{cases}
\phi_A \cdot \kappa_A = \phi_1 \cdot \kappa_1 + \phi_{a1} \cdot \kappa_{a1}, \\
2\phi_1 \cdot \kappa_1 = \phi_2 \cdot \kappa_2 + \phi_5 \cdot \kappa_5 + \phi_{a2} \cdot \kappa_{a2}, \\
\phi_2 \cdot \kappa_2 = \phi_3 \cdot \kappa_3 + \phi_6 \cdot \kappa_6 + \phi_b \cdot \kappa_b, \\
\phi_5 \cdot \kappa_5 + \phi_4 \cdot \kappa_4 = \phi_3 \cdot \kappa_3 + \phi_d \cdot \kappa_d, \\
\phi_3 \cdot \kappa_3 = \phi_4 \cdot \kappa_4 + \phi_c \cdot \kappa_c, \\
\phi_{a1} \cdot \kappa_{a1} = \eta_{a1} \cdot \lambda, \phi_{a2} \cdot \kappa_{a2} = \eta_{a2} \cdot \lambda, \phi_b \cdot \kappa_b = \eta_b \cdot \lambda, \phi_c \cdot \kappa_c = \eta_c \cdot \lambda, \phi_d \cdot \kappa_d = \eta_d \cdot \lambda, \\
\beta_1 \cdot \phi_1 \cdot \kappa_1 + \beta_2 \cdot \phi_2 \cdot \kappa_2 + \beta_3 \cdot \phi_3 \cdot \kappa_3 + \beta_4 \cdot \phi_4 \cdot \kappa_4 + \beta_6 \cdot \phi_6 \cdot \kappa_6 + \beta_{a1} \cdot \phi_{a1} \cdot \kappa_{a1} = J_{\mathrm{E}}^{(\mathrm{N})}, \\
J_{\mathrm{E}}^{(\mathrm{N})} = \eta_{\mathrm{E}} \cdot \lambda + w_0, \lambda = \phi_R \cdot \kappa_t, J_r^{(\mathrm{N})} = \phi_4 \cdot \kappa_4 = \phi_{\mathrm{MT}} \cdot \kappa_{\mathrm{MT}}, J_f^{(\mathrm{N})} = \phi_6 \cdot \kappa_6, \\
\phi_{\mathrm{R}} + \phi_A + \phi_1 + \phi_2 + \phi_3 + \phi_4 + \phi_5 + \phi_6 + \phi_{\mathrm{MT}} + \phi_{a1} + \phi_{a2} + \phi_b + \phi_c + \phi_d = \phi_{\max}.
\end{cases} \tag{S168}$$

Here, Eq. **S28** still holds, and we have:

$$\begin{cases}
J_r^{(\mathrm{E})} + J_f^{(\mathrm{E})} = \varphi \cdot \lambda + w_0, \\
\dfrac{J_r^{(\mathrm{E})}}{\varepsilon_r} + \dfrac{J_f^{(\mathrm{E})}}{\varepsilon_f} = \phi_{\max} - \psi \cdot \lambda,
\end{cases} \tag{S169}$$

where $J_r^{(\mathrm{E})}$ and $J_f^{(\mathrm{E})}$ follow Eq. **S30**, and ψ and ϕ satisfy Eq. **S32** and S33, respectively. The expression for ε_f follows Eq. **S31**. However, the expression for ε_r differs from that in Eq. **S31**. For yeast and mammalian cells, we have:

$$\begin{cases}
\varepsilon_r = \dfrac{\beta_r^{(A)}}{1/\kappa_A + 1/\kappa_1 + 2/\kappa_2 + 2/\kappa_3 + 2/\kappa_4 + 2/\kappa_{\mathrm{MT}}}, \\
\varepsilon_f = \dfrac{\beta_f^{(A)}}{1/\kappa_A + 1/\kappa_1 + 2/\kappa_2 + 2/\kappa_6}.
\end{cases} \tag{S170}$$

At the single-cell level, from Eq. **S169**, and similar to Eq. **S61**–**S63**, if $\varepsilon_r > \varepsilon_f$, the optimal growth strategy is:

$$\begin{cases}
J_f^{(\mathrm{E})} = 0, \\
J_r^{(\mathrm{E})} = \varphi \cdot \lambda + w_0,
\end{cases} \quad \varepsilon_r > \varepsilon_f, \tag{S171}$$

while if $\varepsilon_f > \varepsilon_r$, the optimal growth strategy is:

$$\begin{cases} J_f^{(\mathrm{E})} = \varphi \cdot \lambda + w_0, \\ J_r^{(\mathrm{E})} = 0. \end{cases} \qquad \varepsilon_r < \varepsilon_f. \tag{S172}$$

In both cases, the growth rate λ reaches its maximum value for a given nutrient condition with fixed κ_A:

$$\lambda(\kappa_A) = \begin{cases} \dfrac{\phi_{\max} - w_0/\varepsilon_r(\kappa_A)}{\varphi/\varepsilon_r(\kappa_A) + \psi(\kappa_A)} & \varepsilon_r(\kappa_A) > \varepsilon_f(\kappa_A), \\ \dfrac{\phi_{\max} - w_0/\varepsilon_f(\kappa_A)}{\varphi/\varepsilon_f(\kappa_A) + \psi(\kappa_A)} & \varepsilon_r(\kappa_A) < \varepsilon_f(\kappa_A). \end{cases} \tag{S173}$$

From Eq. **S170**, when κ_A is very small such that $\kappa_A \to 0$, it is evident that for yeast and mammalian cells, we still have:

$$\begin{cases} \varepsilon_r(\kappa_A \to 0) \approx \beta_r^{(A)} \cdot \kappa_A, \\ \varepsilon_f(\kappa_A \to 0) \approx \beta_f^{(A)} \cdot \kappa_A. \end{cases} \tag{S174}$$

Thus,

$$\varepsilon_r(\kappa_A \to 0) > \varepsilon_f(\kappa_A \to 0), \tag{S175}$$

since $\beta_r^{(A)} \gg \beta_f^{(A)}$ still holds. Then, as long as $\varepsilon_r\left(\kappa_A^{\max}\right) < \varepsilon_f\left(\kappa_A^{\max}\right)$, there exists a critical switching point for κ_A (denoted as $\kappa_A^{(\mathrm{C})}$, see Eq. **S41**), below which respiration is more efficient, while above $\kappa_A^{(\mathrm{C})}$, fermentation becomes more efficient in ATP production per proteome. Combined with Eq. **S170**, we have:

$$\kappa_A^{(\mathrm{C})} = \frac{\beta_r^{(A)} - \beta_f^{(A)}}{\beta_f^{(A)}\left(1/\kappa_1 + 2/\kappa_2 + 2/\kappa_3 + 2/\kappa_4 + 2/\kappa_{\mathrm{MT}}\right) - \beta_r^{(A)}\left(1/\kappa_1 + 2/\kappa_2 + 2/\kappa_6\right)}. \tag{S176}$$

Accordingly, we obtain the expressions for $\varepsilon_r\left(\kappa_A^{(\mathrm{C})}\right)$, $\varepsilon_f\left(\kappa_A^{(\mathrm{C})}\right)$ and λ_{C} (i.e., $\lambda\left(\kappa_A^{(\mathrm{C})}\right)$):

$$\begin{cases} \varepsilon_r\left(\kappa_A^{(\mathrm{C})}\right) = \varepsilon_f\left(\kappa_A^{(\mathrm{C})}\right) = \dfrac{\beta_r^{(A)} - \beta_f^{(A)}}{2\left(1/\kappa_3 + 1/\kappa_4 + 1/\kappa_{\mathrm{MT}} - 1/\kappa_6\right)}, \\ \lambda_{\mathrm{C}} = \dfrac{\phi_{\max} - w_0/\varepsilon_{r/f}\left(\kappa_A^{(\mathrm{C})}\right)}{\varphi/\varepsilon_{r/f}\left(\kappa_A^{(\mathrm{C})}\right) + \psi\left(\kappa_A^{(\mathrm{C})}\right)}, \end{cases} \tag{S177}$$

Consequently, yeast and tumor cells would preferentially use respiration under starvation conditions (where $\varepsilon_r > \varepsilon_f$), yet switch to aerobic glycolysis when nutrients are abundant (where $\varepsilon_r < \varepsilon_f$) for optimal cell growth. This qualitatively illustrates the Crabtree effect in yeast and the

Warburg effect in tumors.

At the cell population level, cell heterogeneity resulting from intrinsic and extrinsic noise causes the turnover numbers (i.e., k_{cat}) of enzymes and the critical growth rates at the transition point (λ_C) to follow distributions, which we assume to be Gaussian (see Eq. **S45**, **Appendices 2.3** and **7.1**). Due to the higher level of heterogeneity observed in tumor cells (Duraj et al., 2021; Hanahan and Weinberg, 2011; Hensley et al., 2016) and yeast (Bagamery et al., 2020) compared to *E. coli*, the extent of noise—and thus the CVs of $k_{cat}$and λ_C—in yeast and tumor cells are expected to be larger than those in *E. coli*. The growth rate dependence of the normalized energy fluxes is as follows:

$$\begin{cases} J_f^{(\mathrm{E})}(\lambda)=\dfrac{1}{2}(\varphi\cdot\lambda+w_0)\cdot\left[\operatorname{erf}\left(\dfrac{\lambda-\mu_{\lambda_C}}{\sqrt{2}\sigma_{\lambda_C}}\right)+1\right], \\ J_r^{(\mathrm{E})}(\lambda)=\dfrac{1}{2}(\varphi\cdot\lambda+w_0)\cdot\left[1-\operatorname{erf}\left(\dfrac{\lambda-\mu_{\lambda_C}}{\sqrt{2}\sigma_{\lambda_C}}\right)\right], \end{cases} \tag{S178}$$

where μ_{λ_C} and σ_{λ_C} are the mean and standard deviation of λ_C, respectively, similar to the case of *E. coli*. Therefore, the growth rate dependence of the normalized fluxes is:

$$\begin{cases} J_f^{(\mathrm{N})}(\lambda)=\dfrac{\varphi\cdot\lambda+w_0}{\beta_f^{(A)}}\cdot\left[\operatorname{erf}\left(\dfrac{\lambda-\mu_{\lambda_C}}{\sqrt{2}\sigma_{\lambda_C}}\right)+1\right], \\ J_r^{(\mathrm{N})}(\lambda)=\dfrac{\varphi\cdot\lambda+w_0}{\beta_r^{(A)}}\cdot\left[1-\operatorname{erf}\left(\dfrac{\lambda-\mu_{\lambda_C}}{\sqrt{2}\sigma_{\lambda_C}}\right)\right]. \end{cases} \tag{S179}$$

Combined with Eq. S160, Eq. S179 can be compared to experimental results, although in practice, it is difficult to tune the growth rate of tumor cells in vivo in experiments.

Recently, Shen et al. (Shen et al., 2024) reported that in many yeast and tumor cells, the measured proteome efficiencies in respiration at the cell population level are higher than the corresponding proteome efficiencies in fermentation, even though aerobic glycolysis fermentation fluxes still occur. This finding apparently contradicts prevalent explanations (Basan et al., 2015; Chen and Nielsen, 2019), which assert that overflow metabolism originates from the proteome efficiency in fermentation always being higher than in respiration.

Our model can resolve the puzzle above based on two important features: First, our model predicts that as long as ATP generation per glucose in respiration is higher than in fermentation (i.e., $\beta_r^{(A)}>\beta_f^{(A)}$), which definitely holds true for all organisms, the proteome efficiency in respiration is higher than that in fermentation when the nutrient quality κ_A is low (see Eqs. S37-S38 and S174–S175). Second, and importantly, due to cell heterogeneity at the population level, a subset of cells exhibiting greater proteome efficiency in fermentation compared to respiration could exist, even if the proteome efficiency at the cell population level in respiration is higher than in fermentation.

To facilitate comparison between our model and the experiments of Shen et al. (Shen et al., 2024), we define Pr_f as the proportion of ATP generated from fermentation, and $\overline{\Delta}$ as the proteome efficiency difference between respiration and fermentation, with

$$\mathrm{Pr}_f \equiv \frac{J_f^{(\mathrm{E})}}{J_f^{(\mathrm{E})} + J_r^{(\mathrm{E})}}, \tag{S180}$$

and

$$\overline{\Delta} \equiv 1/\varepsilon_r - 1/\varepsilon_f . \tag{S181}$$

At the cell population level, ε_r, ε_f, $1/\varepsilon_r$ and $1/\varepsilon_f$ roughly follow Gaussian distributions (see Appendix 7.1 and Eq. S170), with

$$\begin{cases} \varepsilon_r \sim \mathcal{N}\left(\mu_{\varepsilon_r}, \sigma_{\varepsilon_r}^2\right), \varepsilon_f \sim \mathcal{N}\left(\mu_{\varepsilon_f}, \sigma_{\varepsilon_f}^2\right), \\ 1/\varepsilon_r \sim \mathcal{N}\left(\mu_{1/\varepsilon_r}, \sigma_{1/\varepsilon_r}^2\right), 1/\varepsilon_f \sim \mathcal{N}\left(\mu_{1/\varepsilon_f}, \sigma_{1/\varepsilon_f}^2\right). \end{cases} \tag{S182}$$

Here, σ_{ε_r}, $\langle \varepsilon_r \rangle$, $\langle \varepsilon_f \rangle$, χ_{ε_r}, and χ_{ε_f}, χ_{1/ε_r}, χ_{1/ε_f}, $\overline{\Delta}$ are the standard deviations and mean values of ε_r, ε_f, $1/\varepsilon_r$ and $1/\varepsilon_f$, respectively. Thus,

$$\begin{cases} \mu_{\varepsilon_r} = \langle \varepsilon_r \rangle, \\ \mu_{\varepsilon_f} = \langle \varepsilon_f \rangle, \end{cases} \tag{S183}$$

where the angle bracket "μ_{Δ}" represents the average over the cell population, and $\sigma_{\overline{\Delta}}$ and $\overline{\Delta}$ are the population-averaged values of ε_r and ε_f, respectively, which are both measurable in experiments. From the derivations shown in Appendix 7.1, we approximately have

$$\begin{cases} \mu_{1/\varepsilon_r} = 1/\mu_{\varepsilon_r} = 1/\langle \varepsilon_r \rangle, \\ \mu_{1/\varepsilon_f} = 1/\mu_{\varepsilon_f} = 1/\langle \varepsilon_f \rangle. \end{cases} \tag{S184}$$

Here, we use σ_{ε_f}, σ_{1/ε_r}, σ_{1/ε_f} and μ_{ε_r} to represent the CVs of ε_r, ε_f, $1/\varepsilon_r$ and $1/\varepsilon_f$, respectively, with

$$\begin{cases} \chi_{\varepsilon_r} = \sigma_{\varepsilon_r}/\mu_{\varepsilon_r}, \chi_{\varepsilon_f} = \sigma_{\varepsilon_f}/\mu_{\varepsilon_f}, \\ \chi_{1/\varepsilon_r} = \sigma_{1/\varepsilon_r}/\mu_{1/\varepsilon_r}, \chi_{1/\varepsilon_f} = \sigma_{1/\varepsilon_f}/\mu_{1/\varepsilon_f}. \end{cases} \tag{S185}$$

Similar to Eq. S151, the CVs of $1/\varepsilon_r$ and $1/\varepsilon_f$ are roughly equal to those of ε_r and ε_f, respectively. Thus,

$$\begin{cases} \chi_{1/\varepsilon_r} \approx \chi_{\varepsilon_r}, \\ \chi_{1/\varepsilon_f} \approx \chi_{\varepsilon_f}. \end{cases} \tag{S186}$$

Combining Eqs. S181 and S182, and using the properties of Gaussian distributions, μ_{ε_f} follows a Gaussian distribution:

$$\bar{\Delta} \sim \mathcal{N}\left(\mu_{\bar{\Delta}}, \sigma_{\bar{\Delta}}^2\right), \tag{S187}$$

where μ_{1/ε_r} and μ_{1/ε_f} are the mean and standard deviation of $\left\langle \ \right\rangle$, respectively. Evidently, we have

$$\begin{cases} \mu_{\bar{\Delta}} = \mu_{1/\varepsilon_r} - \mu_{1/\varepsilon_f}, \\ \sigma_{\bar{\Delta}}^2 = \sigma_{1/\varepsilon_r}^2 + \sigma_{1/\varepsilon_f}^2. \end{cases} \tag{S188}$$

Then, we proceed to calculate the relation between Pr_f and $\overline{\Delta}$ using Eq. S187, and hence we obtain:

$$\mathrm{Pr}_f = \int_0^{+\infty} \frac{1}{\sigma_{\bar{\Delta}}\sqrt{2\pi}} e^{-\frac{1}{2}\left(\frac{x-\mu_{\bar{\Delta}}}{\sigma_{\bar{\Delta}}}\right)^2} dx = \frac{1}{2}\left[\mathrm{erf}\left(\frac{\mu_{\bar{\Delta}}}{\sqrt{2}\sigma_{\bar{\Delta}}}\right)+1\right]. \tag{S189}$$

Combining Eqs. S180, S183–S185, and S188–S189, we have:

$$\frac{J_f^{(\mathrm{E})}}{J_f^{(\mathrm{E})}+J_r^{(\mathrm{E})}} = \frac{1}{2}\left[\mathrm{erf}\left(\frac{1-\left\langle\varepsilon_r\right\rangle/\left\langle\varepsilon_f\right\rangle}{\sqrt{2}\cdot\sqrt{\chi_{\varepsilon_r}^2+\chi_{\varepsilon_f}^2\cdot\left(\left\langle\varepsilon_r\right\rangle/\left\langle\varepsilon_f\right\rangle\right)^2}}\right)+1\right]. \tag{S190}$$

Note that the normalized energy fluxes $J_r^{(\mathrm{E})}$ and $J_f^{(\mathrm{E})}$ are proportional to the measured ATP fluxes generated in respiration and fermentation, respectively. Hence, Eq. S190 can be directly compared to experimental data. For yeast and tumor cells, due to a higher level of heterogeneity, the CVs of ε_r and ε_f, i.e., χ_{ε_r} and χ_{ε_f}, could be significantly higher than the corresponding values in *E. coli*, though their exact values are unknown. Consequently, we plot theoretical results with the values of χ_{ε_r} and χ_{ε_f} chosen as 0.25, 0.40, and 0.58 to compare with the experimental data for yeast and in vivo mouse tumors (Bartman et al., 2023; Shen et al., 2024). In **Fig. 5A-B**, we observe that the theoretical results using $\chi_{\varepsilon_r} = \chi_{\varepsilon_f} = 0.58$ agree well with the experimental data (Bartman et al., 2023; Shen et al., 2024), both on a log scale and linear scale. This demonstrates that our model has the potential to quantitatively illustrate the Crabtree effect in yeast and the Warburg effect in tumors.

Appendix 10 Notes on the application of reference data

Data calibration

Throughout our manuscript, we use experimental data from the original references, except for two calibrations. The first calibration is noted in the footnote of Appendixtable 2. With this calibration, the $J_{\text{acetate}}^{(\text{M})}$-$\lambda$ data for *E. coli* (Basan et al., 2015) in **Appendix-table 2** align with the curve shown in **Fig. 1C**, which includes experimental data for *E. coli* from other sources. The second calibration applies to the data shown in **Figs. 3F** and **1C** (chemostat data for *E. coli*). The unit in the original reference (Holms, 1996) is mmol/(dry mass)g/h. To convert this to the unit mM/OD_{600}/h, used in our text, the conversion factor should be 0.18. Here, we deduce that only 60% of the measured dry biomass in centrifuged material is effective when calibrating with other experimental results. Therefore, there is a calibration factor of 0.6, and the conversion factor changes to 0.3.

Data from the inducible strains

Some of the experimental data in the original references (Basan et al., 2015; Hui et al., 2015) were obtained using *E. coli* strains with titratable systems (e.g., titratable ptsG, LacY). The $J_{\text{acetate}}^{(\text{M})}$-$\lambda$ relation of these inducible strains generally aligns with the same curve as that of wild-type *E. coli* (**Fig. 1C**). Since evolutionary treatment was not applied to the inducible strains, we approximate titration perturbation as a technique that mimics culturing the strains in a less efficient Group A carbon source.

Experimental data sources

The batch culture data for *E. coli* shown in **Fig. 1C** (labeled as minimum/rich media or inducible strains) and **Appendix-fig. 2C** were taken from the source data of the reference's **figure 1** (Basan et al., 2015). The chemostat data for *E. coli* shown in **Fig. 1C** were taken from the reference's table 7 (Holms, 1996). The data for *E. coli* shown in **Fig. 1D** were taken from the reference's extended data **figure 3a** (Basan et al., 2015), with the calibration specified in the footnote to **Appendix-table 2**.

The data for *E. coli* shown in **Fig. 2A** were adopted from the reference's extended data **figure 4a-b** (Basan et al., 2015). The data for *E. coli* shown in **Fig. 2B** were taken from the source data of the reference's **figure 2a** (Basan et al., 2015). The data for *E. coli* shown in **Fig. 2C** were taken from the source data of the reference's **figure 3a** (Basan et al., 2015). The data for *E. coli* shown in **Fig. 3A-B** were taken from the source data of the reference's **figure 3d** (Basan et al., 2015).

The data for *E. coli* shown in **Fig. 3C-D** and **Appendix-fig. 2D-E** were taken from the source data of the reference's **figure 3c** (Basan et al., 2015). The data for *E. coli* shown in **Fig. 3F** were taken from the reference's table 7 (Holms, 1996), with a calibration factor specified in the above paragraph ("Data calibration").

The data for *E. coli* shown in **Fig. 4A-B** and **Appendix-fig. 3A-D** were taken from the reference's table S2 with the label "C-lim" (Hui et al., 2015). We excluded the reference's data with λ = 0.45205 h^{-1} as there are other unconsidered factors involved during slow growth (Dai et

al., 2016) (for $\lambda < 0.5\ h^{-1}$), and we suspect that unknown calibration factors may exist. The data for *E. coli* shown in **Fig. 4C-D** and **Appendix-fig. 3E-N** were adopted from the reference's extended data **figure 6**–**7** (Basan et al., 2015).

The batch culture data for yeast shown in **Fig. 5** were derived from the source data of the reference's extended **figure 4c-d** (Shen et al., 2024). The chemostat data for yeast shown in **Fig. 5** were derived from the source data of the reference's **figure 3d-e** (Shen et al., 2024), where glucose is the limiting nutrient. We excluded the reference's data for *I. orientalis* under condition C2, where the ATP flux was abnormally small. The mouse tumor in vivo data shown in **Fig. 5** were derived from the source data of the reference's **figure 4e-g** (Shen et al., 2024), which were originally reported by Bartman et al. (Bartman et al., 2023), the same research group as Shen et al. (Shen et al., 2024). We did not include the cancer cell line data shown in **figure 4a-c** of Shen et al. (Shen et al., 2024) since it appears that the proteomic data and flux data were obtained from two different references with inconsistent culturing conditions.

The gene names of *E. coli* depicted in **Appendix-fig. 1B** were identified using the KEGG database. The data for *E. coli* shown in **Appendix-fig. 2G** were drawn from **Appendix-table 1**, which includes the original references themselves. The flux data for *E. coli* presented in **Appendix-table 2** were obtained from the reference's extended data **figure 3a** (Basan et al., 2015), with the calibration specified in the footnote. The proteome data for *E. coli* shown in Appendixtable 2 were taken from the reference's supplementary Table N5 (Basan et al., 2015).

No.*	Reaction	Enzyme	Gene name	EC	MW (kDa)	In vitro k_{cat} (s^{-1})	References	In vivo† k_{cat} (s^{-1})	Chosen k_{cat} (s^{-1})
J_1	Glucose-6P ↔ Fructose-6P	Glucose-6-phosphate isomerase	pgi	EC:5.3.1.9	1.2×10^2	2.6×10^2	PMID: 7004378; DOI:10.1016/j.ijms.2004.09.017	8.7×10^2	8.7×10^2
	Fructose-6P → Fructose-1,6P	Phosphofructokinase	pfkA‡	EC:2.7.1.11	1.4×10^2	4.4×10^2	PMID: 6218375; 70226	1.7×10^3	1.7×10^3
	Fructose-1,6P ↔ Glyceraldehyde 3-phosphate+Dihydroxy acetone phosphate	Fructose-bisphosphate aldolase	fbaA‡	EC:4.1.2.13	7.8×10	1.4×10	PMID: 8939754; 15531627	1.6×10^2	1.6×10^2
	Dihydroxyacetone phosphate ↔ Glyceraldehyde 3-phosphate	Triosephosphate Isomerase	tpiA	EC:5.3.1.1	5.4×10	4.3×10^2	PMID: 3887397; 6092857	2.7×10^2	2.7×10^2
	Glyceraldehyde 3-phosphate ↔ 1,3-Bisphosphoglycerate	Glyceraldehyde-3-phosphate dehydrogenase	gapA	EC:1.2.1.12	1.4×10^2	9.5×10	PMID: 4932978; 2200929	1.5×10^2	1.5×10^2
	1,3-Bisphosphoglycerate ↔ 3-Phosphoglycerate	Phosphoglycerate kinase	pgk	EC:2.7.2.3	4.4×10	3.5×10^2	PMID: 367367; 166274	1.9×10^2	1.9×10^2
	3-Phosphoglycerate ↔ 2-Phosphoglycerate	Phosphoglycerate mutase	gpmA‡	EC:5.4.2.11	4.9×10	3.3×10^2	PMID: 10437801	4.5×10^2	4.5×10^2
	2-Phosphoglycerate ↔ Phosphoenolpyruvate	Enolase	eno	EC:4.2.1.11	9.0×10	2.2×10^2	PMID: 1094232; 4942326	1.7×10^2	1.7×10^2
J_2	Phosphoenolpyruvate → Pyruvate	Pyruvate kinase	pykF‡	EC:2.7.1.40	2.4×10^2	5.0×10^2	PMID: 6759852	1.6×10^3	1.6×10^3
	Pyruvate → Acetyl-CoA	Pyruvate dehydrogenase	aceE‡	EC:1.2.4.1	1.0×10^2	1.2×10^2	PMID: 23088422	3.4×10^2	3.4×10^2
J_3	Oxaloacetate +Acetyl-CoA → Citrate	Citrate synthase	gltA	EC:2.3.3.1	9.7×10	2.4×10^2	PMID: 4900996; 23954305	7.1×10	7.1×10
	Citrate ↔ Isocitrate	Aconitate hydratase	acnB‡	EC:4.2.1.3	9.4×10	7.0×10	PMID:15963579; 12473114	6.3×10	6.3×10
	Isocitrate→ α-Ketoglutarate	Isocitrate dehydrogenase	icd	EC:1.1.1.42	9.5×10	2.0×10^2	PMID: 8141; 36923; 2200929	3.3×10	3.3×10
J_4	α-Ketoglutarate → Succinyl-CoA	α-Ketoglutarate dehydrogenase complex E1 component	suc A suc B‡	EC:1.2.4.2, EC:2.3.1.61	1.9×10^2	1.5×10^2	PMID: 6380583; 4588679	1.3×10^2	1.3×10^2
	Succinyl-CoA ↔ Succinate	Succinyl-CoA synthetase	suc C suc D	EC:6.2.1.5	1.6×10^2	9.1×10	PMID: 5338130	1.0×10^2	1.0×10^2
	Succinate → Fumarate	Succinate dehydrogenase	sdh A sdh B‡	EC:1.3.5.1	1.0×10^2	1.1×10^2	PMID: 4334990; 16484232	1.1×10^2	1.1×10^2
	Fumarate ↔ Malate	Fumarase	fumA‡	EC:4.2.1.2	2.0×10^2	1.2×10^3	PMID: 3282546; 12021453	4.9×10^2	4.9×10^2
	Malate ↔ Oxaloacetate	Malate dehydrogenase	mdh	EC:1.1.1.37	6.1×10	5.5×10^2	doi:10.1016/0076-6879 (69) 13029-3	6.6×10	6.6×10
J_5	Phosphoenolpyruvate →Oxaloacetate	Phosphoenolpyruvate carboxylase	ppc	EC:4.1.1.31	4.0×10^2	1.5×10^2	PMID: 9927652; 4932977	/	1.5×10^2
J_6	Acetyl-CoA ↔ Acetyl phosphate	Phosphate acetyltransferase	pta	EC:2.3.1.8	7.7×10	3.0×10	PMID:20236319	3.7×10^2	3.7×10^2
	Acetyl phosphate↔ Acetate	Acetate kinase	ackA	EC:2.7.2.1	4.3×10	3.6×10^3	EcoCyc: EG10027; PMID: 24801996	3.3×10^2	3.3×10^2
	Acetate (intracellular) ↔ Acetate (extracellular)	Acetate transporter	actP	/	2×10	4.7×10^2	PMID: 31405984 (Estimated)	/	4.7×10^2
J_7	Pyruvate → Phosphoenolpyruvate	Pyruvate, water dikinase	ppsA	EC:2.7.9.2	2.5×10^2	3.5×10	PMID: 4319237	/	3.5×10

Appendix-table 1

Molecular weight (MW) andinvivo/in vitrok_{cat}data for*E. coli*

Appendix-table 1 (continued)

J_A	Glucose-6P (extracellular) → Glucose-6P (intracellular)	Glucose-6-phosphate transporter	UhpT	/	5×10	2×10^2	PMID: 3283129; 2197272; 20018695 (Estimated)	/	2×10^2
	Glucose (extracellular) → Glucose-6P	Glucose-specific PTS enzyme	ptsG	EC: 2.7.1.199	5×10	1×10^2	PMID: 9575173; 20018695; 12146972	/	1×10^2
	Lactose (extracellular) → Lactose (intracellular)	Lactose transporter	lacY	/	4.6×10	6×10	PMID: 6444453; 20018695	/	6×10
	Lactose →Glucose + Galactose	β-galactosidase	lacZ	EC:3.2.1.23	4.6×10^2	6.4×10^2	PMID: 8008071; 23011886 (Estimated)	/	6.4×10^2
J_{py}	Pyruvate (extracellular) → Pyruvate (intracellular)	Pyruvate transporter	btsT CstA	/	8×10	6×10	PMID:20018695; 33260635; EcoCyc: G7942; EG10167 (Estimated)	/	6×10

Appendix-table 2

Proteome and flux data (Basan et al., 2015) used to calculate the in vivo k_{cat} of *E. coli*

	Culture 1	Culture 2	Culture 3	Culture 4
Growth rate λ (h^{-1}) *	0.82	0.87	0.97	1.03
$J_{acetate}$ (mM OD_{600}^{-1} h^{-1}) †	0.39	1.18	2.68	2.84
$J_{CO2,\,r}$ (mM OD_{600}^{-1} h^{-1}) †	7.44	6.05	4.30	3.04
Gene name	**Proteomic mass fractions obtained using absolute abundance (ϕ_i)**			
pgi	0.09%	0.09%	0.10%	0.11%
pfkA	0.06%	0.06%	0.06%	0.06%
fbaA	0.32%	0.35%	0.35%	0.39%
tpiA	0.12%	0.15%	0.13%	0.18%
gapA	1.19%	1.29%	1.33%	1.47%
pgk	0.30%	0.31%	0.32%	0.36%
gpmA	0.15%	0.15%	0.15%	0.16%
eno	0.63%	0.70%	0.75%	0.83%
pykF	0.15%	0.15%	0.18%	0.21%
aceE	0.30%	0.32%	0.34%	0.41%
gltA	0.88%	0.80%	0.61%	0.48%
acnB	0.92%	0.84%	0.66%	0.57%
icd	1.55%	1.55%	1.31%	1.39%
suc A suc B	0.71%	0.75%	0.64%	0.55%
suc C suc D	0.88%	0.84%	0.66%	0.52%
sdh A sdh B	0.49%	0.45%	0.42%	0.35%
fumA	0.24%	0.21%	0.17%	0.13%
mdh	0.45%	0.45%	0.41%	0.39%
pta	0.10%	0.10%	0.10%	0.10%
ackA	0.06%	0.07%	0.06%	0.06%

Symbols	Illustrations / Definitions	Model variable / parameter settings for *E.coli*[*]
A (in the figures)	A Group A carbon source joining the metabolic network from the upper part of glycolysis.	NA[**]
M_i (in the figures)	A metabolite in the metabolic network that serve as intermediate node.	NA
J_i (in the figures)	The stoichiometric flux delivering carbon flux, an extensive variable†, see Eq. S7.	see Eqs. S7-S8.
r_i (in the figures)	The mass fraction of carbon flux drawn from a precursor pool.	r_{a1}=24%, r_{a2}=24%, r_b=28%, r_c=12%, r_d=12% (Nelson et al., 2008).
λ	Growth rate of the cell population; see Eq. S36 for the optimal model solution.	see Eqs. S4 and S36.
J_r, J_f	J_r and J_f are stoichiometric fluxes of respiration and fermentation, extensive variables.	J_r= J_4; J_f =J_6 (see Eq. S22)
m_0	The weighted average carbon mass of metabolite molecules at the entrance of precursor pools.	See Eq. S17.
M_{carbon}	The carbon mass of the cell population, an extensive variable.	NA
M_{protein}	The protein mass of the cell population; an extensive variable.	NA
$M_Q^{(P)}$, $M_R^{(P)}$, $M_C^{(P)}$	The mass of Q-class, R-class, or C-class proteome.	See Eq. S2.
f_Q, f_R, f_C	The ribosome allocation fraction for protein synthesis of Q-class, R-class, or C-class.	f_Q=ϕ_Q.
m_{AA}	The average molecular weight of amino acids.	A reducible parameter for the results.
k_T	Translation speed of ribosomes.	k_T= 20.1 aa/s (Scott et al., 2010).
ϕ_Q, ϕ_R, ϕ_C	The mass fraction of Q-class, R-class, or C-class proteome; see Appendix 1.1.	ϕ_Q=52% (Scott et al., 2010).
ϕ_{max}	The maximum proteomic mass fraction of proteome allocation for fermentation, respiration, and biomass generation, with $\phi_{max} \equiv 1 - \phi_Q$.	ϕ_{max}=48% (Scott et al., 2010).
m_R	The protein mass of a single ribosome.	m_R =7336 m_{AA} (Neidhardt et al., 1990).
V_{cell}	The cell volume of the cell population (the "big cell"); an extensive variable.	NA
N_R, $M_{rp}^{(P)}$	The number or the total protein mass of ribosomes in the big cell; extensive variables.	NA
ς	The ratio of the mass of R-class proteome to the protein mass of ribosomes: $\varsigma \equiv M_R^{(P)}/M_{rp}^{(P)}$.	ς=1.67 (Scott et al., 2010).
$[E_i]$, $[S_i]$	The concentration of enzyme E_i or substrate S_i; intensive variables.	NA
a_i, d_i, b_i, c_i	a_i and d_i are reaction parameters; bi and c_i are stoichiometric coefficients. See Appendix 1.3.	NA
K_i	The Michaelis constant, defined as K_i=$(d_i+k_i^{cat})/ a_i$.	Obtainable from Bennett et al. (Bennett et al., 2009), yet unused in practice since $[Si]> K_i$ (see Appendix 1.5).
v_i	The reaction rate per volume of a biochemical reaction catalyzed by E_i; an intensive variable.	See Eq. S6.
N_{E_i}, M_{E_i}	The copy number or the total weight enzyme E_i in the cell population; extensive variables.	$N_{E_i} = V_{cell} \cdot [E_i]$; $M_{E_i} = N_{E_i} \cdot m_{E_i}$.
m_{carbon}	The mass of a carbon atom.	m_{carbon}=$\frac{12}{N_{\text{Avogadro}}}$ g, where g represents gram and N_{Avogadro} is the Avogadro constant.
Φ_i	The enzyme cost of all E_i molecules in the cell population; an extensive variable.	$\Phi_i \equiv N_{E_i} \cdot n_{E_i}$.
ξ_i	ξ_i is defined such that $\xi_i = J_i/\Phi_i$.	$\xi_i \equiv \frac{k_i^{cat}}{n_{E_i}} \cdot \frac{[S_i]}{[S_i]+K_i}$.
$J_i^{(N)}$	The normalized flux, i.e., flux per unit of biomass; an intensive variable‡.	$J_i^{(N)} \equiv J_i \cdot m_0/M_{carbon}$ see Eqs. S15-S16.
$J_r^{(N)}$, $J_f^{(N)}$	$J_r^{(N)}$and $J_f^{(N)}$ are the normalized fluxes of respiration and fermentation, intensive variables.	$J_r^{(N)}$=$J_4^{(N)}$, $J_f^{(N)}$=$J_6^{(N)}$.
$N_{EP_i}^{carbon}$	The number of carbon atoms in the entry point metabolite molecule of Precursor Pool i.	$N_{EP_{a1}}^{carbon}$=6, $N_{EP_{a2}}^{carbon}$=3, $N_{EP_b}^{carbon}$=3, $N_{EP_c}^{carbon}$=5, $N_{EP_d}^{carbon}$=4 (Nelson et al., 2008).
k_{cat}, k_i^{cat}	The turnover number of a catalytic enzyme.	See Appendix-table 1.
m_{E_i}, n_{E_i}	m_{E_i} and n_{E_i} are the molecular weight and the enzyme cost of an E_i molecule, respectively.	See Appendix-table 1.
r_{carbon}, $r_{protein}$	r_{carbon} and $r_{protein}$ are the mass fractions of all carbon and protein within a cell, respectively.	$r_{protein}$=0.55; r_{carbon}=0.48 (Neidhardt et al., 1990).
κ_i	Substrate quality of a metabolite in a biochemical reaction; see Eq. S12 and S20.	Calculated from the values of k_i^{cat}, m_{E_i}, m_0, $r_{protein}$, r_{carbon}.
κ_A	Substrate quality of a Group A carbon source; see Eq. S27.	Calculated from the values of k_A^{cat}, m_{E_A}, m_0, $r_{protein}$, r_{carbon}, K_A and the concentration of the Group A carbon source $[A]$.
ϕ_i	The proteomic mass fraction of enzyme E_i: $\phi_i \equiv M_{E_i}/M_{protein}$; an intensive variable.	See Eq. S9.
η_i	The fraction of stoichiometric flux drawn from a precursor pool; see Eqs. S13, S14 and S18.	η_{a1}=15%, η_{a2}=30%, η_b=35%, η_c=9%, η_d=11% (calculated from the values of r_i and $N_{EP_i}^{carbon}$).
ϕ_r, ϕ_f, ϕ_{BM}	ϕ_f, ϕ_f, ϕ_{BM} are the proteomic mass fraction of enzymes dedicated to fermentation, respiration, and biomass generation, respectively.	NA

Appendix-table 3

Illustrations of symbols in this manuscript.

$\boldsymbol{\kappa_t}$	A parameter determined by the translation rate, defined as $\kappa_t \equiv k_T \cdot m_{AA}/(\varsigma \cdot m_R)$.	κ_t=1/610 (s^{-1}) (calculated from the values of k_T, ς and m_R).
$\boldsymbol{J_{BM}}$	The carbon flux of biomass production; an extensive variable.	See Eq. S10.
$\boldsymbol{J_E}$	The energy demand for cell growth, expressed as the stoichiometric energy flux in ATP; an extensive variable.	See Eq. S25.
$\boldsymbol{J_E^{(N)}}$	The normalized flux of energy demand in ATP; an intensive variable.	$J_E^{(N)} \equiv J_E \cdot m_0/M_{carbon}$.
$\boldsymbol{r_E, \eta_E}$	r_E and η_E are energy coefficients. r_E is the slope of J_E versus J_{BM}; $\eta_E = r_E \cdot \left[\sum_i r_i/N_{EP_i}^{carbon}\right]$.	See Appendix 8.2.
$\boldsymbol{\beta_i}$	The stoichiometric coefficient of ATPs in biochemical reactions shown in Figs. 1B and 3E (for *E. coli*) or Appendix-fig. 5E-F (for yeast and mammalian cells).	β_1=4; β_2=3; β_3=2; β_4=6; β_6=1; β_{a1}=4; β_7=1; β_8=2; β_9=6 (*E.coli*) β_1=5; β_2=1; β_3=5; β_4=7.5; β_6=-2.5; β_{a1}=5 (eukaryotic cells) (Neidhardt et al., 1990; Sauer et al., 2004)
$\boldsymbol{\beta_r^{(A)}, \beta_f^{(A)}}$	$\beta_r^{(A)}$and $\beta_f^{(A)}$ are the stoichiometric coefficients of ATP production per glucose in respiration and fermentation, respectively.	$\beta_r^{(A)}$=26, $\beta_f^{(A)}$=12 (*E.coli*); $\beta_r^{(A)}$=32, $\beta_f^{(A)}$=2 (eukaryotic cells) (Neidhardt et al., 1990).
$\boldsymbol{J_r^{(E)}, J_f^{(E)}}$	$J_r^{(E)}$and $J_f^{(E)}$ are normalized energy fluxes of respiration and fermentation, intensive variables.	$J_r^{(E)} \equiv \frac{\beta_r^{(A)}}{2} \cdot J_r^{(N)}$; $J_f^{(E)} \equiv \frac{\beta_f^{(A)}}{2} \cdot J_f^{(N)}$.
$\boldsymbol{\varepsilon_r, \varepsilon_f}$ $\boldsymbol{\varepsilon_r^{(dt)}, \varepsilon_f^{(dt)}}$	ε_r (or $\varepsilon_r^{(dt)}$) and ε_f (or $\varepsilon_f^{(dt)}$) are the proteome efficiencies for energy biogenesis in the respiration and fermentation pathways: $\varepsilon_r \equiv J_r^{(E)}/\phi_r$ and $\varepsilon_f \equiv J_f^{(E)}/\phi_f$.	Calculated from the values of κ_A, κ_i, $\beta_r^{(A)}$ and $\beta_f^{(A)}$ with Eq. S132 and S161.
$\boldsymbol{\varphi}$	φ is an energy demand coefficient, defined in Eq. S33 and mainly determined by η_E.	Calculated from the values of η_E, β_i, η_i with Eq. S33. See Appendix 8.2.
$\boldsymbol{\psi, \psi_{dt}}$	ψ^{-1} (or ψ_{dt}^{-1}) is the proteome efficiency for biomass generation in the biomass pathway, with $\psi^{-1} \equiv \lambda/\phi_{BM}$.	Calculated from the values of η_i, κ_A, κ_i, Ω, κ_t with Eqs. S133 and S162.
$\boldsymbol{\kappa_r^{(A)}, \kappa_f^{(A)}}$	$\kappa_r^{(A)}$and $\kappa_f^{(A)}$ are parameters defined as $\kappa_r^{(A)} \equiv \left[\frac{1}{\kappa_1} + \frac{2}{\kappa_2} + \frac{2}{\kappa_3} + \frac{2}{\kappa_4}\right]^{-1}$ and $\kappa_f^{(A)} \equiv \left[\frac{1}{\kappa_1} + \frac{2}{\kappa_2} + \frac{2}{\kappa_6}\right]^{-1}$.	Calculated from the values of κ_i.
$\boldsymbol{\Omega}$	Ω is a composite parameter defined as $\Omega \equiv 1/\kappa_t + \sum_i^{a1,a2,b,c,d} \eta_i/\kappa_i$.	See Appendix 8.2.
$\boldsymbol{\kappa_{glucose}^{(ST)}, \kappa_{lactose}^{(ST)}}$	The substrate quality of glucose or lactose at saturated concentration.	Calculated using Eq. S27 and the approximation used in Eq. S20.
$\boldsymbol{\Delta}$	Δ is a function of κ_A defined as $\Delta(\kappa_A) \equiv \varepsilon_f(\kappa_A)/\varepsilon_r(\kappa_A)$.	$\Delta \equiv \varepsilon_f/\varepsilon_r$.
$\boldsymbol{\kappa_A^{(C)}}$	The critical value of κ_A which satisfy $\Delta(\kappa_A)$=1 and thus $\varepsilon_f(\kappa_A)$=$\varepsilon_r(\kappa_A)$; See Eqs. S42 (for *E. coli*) and S176 (for yeast and mammalian cells).	Calculated from the values of β_i and κ_i with Eq. S42.
$\boldsymbol{\lambda_C}$	The critical growth rate at the transition point: $\lambda_C \equiv \lambda(\kappa_A^{(C)})$; See Eqs. S43 and S177.	Calculated from the values of ϕ_{max}, φ, β_i, κ_i, $\kappa_A^{(C)}$, Ω, η_i with Eqs. S43, S32 and S162.
$\boldsymbol{\theta}$	The Heaviside step function.	NA
$\boldsymbol{J_{acetate}, J_{CO_2,r}}$	$J_{acetate}$ and $J_{CO_2,r}$ are the stoichiometric fluxes of acetate from the fermentation pathway and CO2 from the respiration pathway; extensive variables.	$J_{acetate} = J_f$; $J_{CO_2,r}$=3· $J_{CO_2,r}$. See Appendix 8.1 and Eq. S158.
$\boldsymbol{J_{acetate}^{(M)}, J_{CO_2,r}^{(M)}}$	$J_{acetate}^{(M)}$ and $J_{CO_2,r}^{(M)}$ are the fluxes of $J_{acetate}$ and $J_{CO_2,r}$ (per biomass) in the unit of mM/OD600/h, which are measurable in experiment. Intensive variables.	$J_{acetate}^{(M)} \approx 2 \cdot J_f^{(N)}$; $J_{CO_2,r}^{(M)} \approx 6 \cdot J_r^{(N)}$. See Appendix 8.1 and Eq. S160.
$\boldsymbol{\kappa_A^{max}}$	The maximum value of κ_A available across different Group A carbon sources.	Approximated by the max κ_A across Group A carbon sources, calculated with Eq. S27 and the approximation used in Eq. S20.
$\boldsymbol{\lambda_{max}}$	The population cell growth rate for the maximum value of κ_A: $\lambda_{max} = \lambda(\kappa_A^{max})$.	Calculated from the maximum of Eq. 36 with the values of β_i, κ_i, κ_A^{max}, φ, Ω, κ_t, and Eqs. S32, S132, S161 and S162.
$\boldsymbol{\mathcal{N}(\mu, \sigma^2)}$	A Gaussian distribution with a mean of μ and a standard deviation of σ.	The probability density function is $f(x) = \frac{1}{\sigma\sqrt{2\pi}} e^{-\frac{1}{2}\left(\frac{x-\mu}{\sigma}\right)^2}$.
$\boldsymbol{\mu_{\lambda_C}, \sigma_{\lambda_C}}$	μ_{λ_C} and σ_{λ_C} are the mean and standard deviation of λ_C, respectively.	μ_{λ_C} is approximated by the deterministic value of λ_C; see Appendix 2.3 for σ_{λ_C} settings. See Appendix 8.2 for the values.
erf	The error function in mathematics.	erf $(x) = \frac{2}{\sqrt{\pi}} \int_0^x exp(-t^2) dt$
$\boldsymbol{\phi_Z}$	The proteomic mass fraction of useless proteins encoded by the LacZ gene.	See Appendix 3.1.
$\boldsymbol{w}$	An energy dissipation coefficient.	See Appendix 3.2.
$\boldsymbol{w_0}$	The maintenance energy coefficient.	w_0=0 or 2.5 (h^{-1}) as specified in Figs.3-4, S2-S3. See Appendices 3.3 and 8.2.
$\boldsymbol{\iota}$	ι is the inhibition coefficient such that $(1+\iota)^{-1}$ represents the translation efficiency.	See Appendices 3.3 and 8.2.

Appendix-table 3 (continued)

$\iota_{w_0=0}^{(2\mu m\ Cm)}$; $\iota_{w_0=0}^{(4\mu m\ Cm)}$; $\iota_{w_0=0}^{(8\mu m\ Cm)}$; $\iota_{w_0=2.5}^{(2\mu m\ Cm)}$; $\iota_{w_0=2.5}^{(4\mu m\ Cm)}$; $\iota_{w_0=2.5}^{(8\mu m\ Cm)}$	The values for ι in the cases with 2 μm , 4 μm, or 8 μm of chloramphenicol and the maintenance energy coefficient w_0 chosen as 0 or 2.5 (h^{-1}).	$\iota_{w_0=0}^{(2\mu m\ Cm)}$=1.15; $\iota_{w_0=0}^{(4\mu m\ Cm)}$=2.33; $\iota_{w_0=0}^{(8\mu m\ Cm)}$=6.25; $\iota_{w_0=2.5}^{(2\mu m\ Cm)}$=1.05; $\iota_{w_0=2.5}^{(4\mu m\ Cm)}$=2.00; $\iota_{w_0=2.5}^{(8\mu m\ Cm)}$=5.40. See Appendix 8.2.
κ_{py}	The substrate quality of pyruvate; see Eq. S89.	Calculated from the values of k_A^{cat}, m_{E_A}, m_0, $r_{protein}$, r_{carbon}, K_A and the external concentration of pyruvate [py].
$\beta_r^{(py)}$, $\beta_f^{(py)}$	$\beta_r^{(py)}$and $\beta_f^{(py)}$ are the stoichiometric coefficients of ATP production per pyruvate in respiration and fermentation, respectively.	$\beta_r^{(A)}$=10; $\beta_f^{(A)}$=3. (Neidhardt et al., 1990).
$J_r^{(E,py)}$, $J_f^{(E,py)}$	$J_r^{(E,py)}$and $J_f^{(E,py)}$ are the normalized energy fluxes of respiration and fermentation for pyruvate utilization; intensive variables.	The corresponding variables of $J_r^{(E)}$ and $J_f^{(E)}$ in the case of pyruvate utilization.
$\varepsilon_r^{(py)}$, $\varepsilon_f^{(py)}$	$\varepsilon_r^{(py)}$ and $\varepsilon_f^{(py)}$ are the proteome efficiencies for energy biogenesis using pyruvate in the respiration and fermentation pathways.	The corresponding variables of ε_r and ε_f in the case of pyruvate utilization.
Ω'_{Gg}	Ω'_{Gg} is a composite parameter defined as $\Omega'_{\mathrm{Gg}} \equiv (\eta_b + \eta_c)/\kappa_8 + \eta_{a1}/\kappa_9$.	See Appendix 8.2.
ψ_{py}, φ_{py}, $\kappa_{py}^{(ST)}$ $\kappa_{py}^{(C)}$, $\lambda_{\max}^{(py)}$	ψ_{py}, φ_{py}, $\kappa_{py}^{(ST)}$, $\kappa_{py}^{(C)}$ and $\lambda_{\max}^{(py)}$ are the corresponding variables/parameters of ψ, φ, $\kappa_A^{\max}$, $\kappa_A^{(C)}$ and $\lambda_{\max}$ in the case of pyruvate utilization.	See Appendices 4.1 and 8.2.
$\lambda_C^{(py)}$, $\mu_{\lambda_C^{(py)}}$, $\sigma_{\lambda_C^{(py)}}$	$\lambda_C^{(py)}$, $\mu_{\lambda_C^{(py)}}$ and $\sigma_{\lambda_C^{(py)}}$ are the corresponding variables/parameters of λ_C, μ_{λ_C} and σ_{λ_C} in the case of pyruvate utilization.	See Appendices 4.1 and 8.2.
$N_{P_i}^{carbon}$	The number of carbon atoms in a molecule of Pool *i*.	The value of $N_{P_i}^{carbon}$ is approximated by $N_{EP_i}^{carbon}$ (Eq. S107).
$\kappa_i^{(21AA)}$	The substrate quality of the external supplied amino acids identical to those in Pool *i*.	See Appendices 4.2 and 8.2.
$\Omega_{21\mathrm{AA}}$	$\Omega_{21\mathrm{AA}}$ is a composite parameter defined as $\Omega_{21\mathrm{AA}} \equiv 1/\kappa_t + \eta_{a1}/\kappa_{a1} + \sum_i^{a2,b,c,d} \eta_i/\kappa_i^{(21AA)}$.	See Appendices 4.2 and 8.2.
ψ_{21AA}, φ_{21AA}, $\lambda_{\max}^{(21AA)}$, $\lambda_C^{(21AA)}$, $\mu_{\lambda_C^{(21AA)}}$, $\sigma_{\lambda_C^{(21AA)}}$	ψ_{21AA}, φ_{21AA}, $\lambda_{\max}^{(21AA)}$, $\lambda_C^{(21AA)}$, $\mu_{\lambda_C^{(21AA)}}$ and $\sigma_{\lambda_C^{(21AA)}}$ are the corresponding variables/parameters of ψ, φ, $\lambda_{\max}$, λ_C, μ_{λ_C} and σ_{λ_C} in the case of a Group A carbon source is mixed with 21 types of amino acids at saturated concentrations.	See Appendices 4.2 and 8.2.
Ω_{7AA}, φ_{7AA}, $\mu_{\lambda_C^{(7AA)}}$, $\sigma_{\lambda_C^{(7AA)}}$	Ω_{7AA}, φ_{7AA}, $\mu_{\lambda_C^{(7AA)}}$ and $\sigma_{\lambda_C^{(7AA)}}$ are the corresponding parameters of Ω, φ, μ_{λ_C} and σ_{λ_C} in the case of a Group A carbon source is mixed with 7 types of amino acids.	See Appendices 4.2 and 8.2.
$J_{in}^{(N)}$, ϑ	$J_{in}^{(N)}$ is the normalized stoichiometric influx of a Group A carbon source (Eq. S136). ϑ is a parameter defined as $\vartheta = \eta_{a1} + \eta_c + (\eta_{a2} + \eta_b + \eta_d)/2$ for the model shown in Fig. 1B.	See Appendix 6.3
χ_{ext}, χ_{int}, χ_{tot}	χ_{ext}, χ_{int} and χ_{tot} are the level of extrinsic noise, intrinsic noise and total noise in a system.	See Appendix 7.1
$\mu_{k_i^{cat}}$, $\sigma_{k_i^{cat}}$, $\mu_{1/k_i^{cat}}$, $\sigma_{1/k_i^{cat}}$ $\mu'_{1/k_i^{cat}}$, σ'_{1/k_{cat}^i}	$\mu_{k_i^{cat}}$ and $\sigma_{k_i^{cat}}$ are the mean and standard deviation of k_i^{cat}; $\mu_{1/k_i^{cat}}$ (or $\mu'_{1/k_i^{cat}}$) and $\sigma_{1/k_i^{cat}}$ (or σ'_{1/k_{cat}^i})are the mean and standard deviation of $1/k_i^{cat}$. See Appendix 7.1.	$\mu_{k_i^{cat}}$ is approximated by the deterministic value of k_i^{cat}. The CV of k_i^{cat} is set to 25%. $\mu_{1/k_i^{cat}} \approx 1/\mu_{k_i^{cat}}$; $\sigma_{1/k_i^{cat}}/\mu_{1/k_i^{cat}} \approx \sigma_{k_i^{cat}}/\mu_{k_i^{cat}}$.
$\mathbf{IG}(x;\mu,\zeta)$,	The inverse Gaussian (IG) distribution: variable x>0 with parameters μ and ζ. See Eq. S142.	The probability density function is $\sqrt{\frac{\zeta}{2\pi x^3}}\exp\left(-\frac{\zeta(x-\mu)^2}{2\mu^2 x}\right)$.
$\mathbf{IOG}(x;\mu,\zeta)$	The positive inverse of Gaussian (IOG) distribution: variable x>0 with parameters μ and ζ. See Eq. S140 and Appendix 7.1.	The probability density function is $\sqrt{\frac{\zeta}{2\pi x^3}}\exp\left(-\frac{\zeta(x-\mu)^2}{2\mu^2 x}\right)$.
$\zeta_{1/k_i^{cat}}$, $\zeta'_{1/k_i^{cat}}$	Distributional parameters of $1/k_i^{cat}$ corresponding to ζ in an IG or IOG distribution.	See Appendix 7.1
$G(k)$	The characteristic function of IG distribution. See Eq. S147.	$G(k) = \int_{-\infty}^{\infty} e^{ikx} \cdot IG(x;\mu,\zeta)dx$
X_i, α_i, Θ, T_Θ, $\Gamma_i(t)$	X_i, α_i, Θ and $\Gamma_i(t)$ are variables and parameters used to calculate the first passage time T_Θ of a stochastic process that mimics the duration of an enzyme to finishing a catalytic job.	See Appendix 7.1.
γ_i, Ξ, μ_Ξ, σ_Ξ	γ_i is a real number; Ξ is a variable defined as $\Xi \equiv \sum_{i=1}^{n} \gamma_i/k_{cat}^i$; μ_Ξ and σ_Ξ are the mean and standard deviation of Ξ.	See Eq. S153 and Appendix 7.1.
μ_{κ_i}, σ_{κ_i}, μ_{1/κ_i}, σ_{1/κ_i}	μ_{κ_i} and σ_{κ_i} are the mean and standard deviation of κ_i; μ_{1/κ_i} and σ_{1/κ_i} are the mean and standard deviation of $1/\kappa_i$.	See Eq. S154 and Appendices 7.1 and 8.2.
λ_r, λ_f, μ_{λ_r}, σ_{λ_r}, μ_{λ_f}, σ_{λ_f}, ρ_{rf}	λ_r and λ_f are the growth rates when cells choose respiration or fermentation; μ_{λ_r}, $\mu_{\lambda_f}$and σ_{λ_r}, σ_{λ_f} are the means and standard deviations of λ_r and λ_f; ρ_{rf} is the correlation of λ_r and λ_f.	See Eq. S36 and Appendices 7.1 and 8.2.
$\lambda_{succinate}^{(21AA)}$, $\lambda_{acetate}$ $\mu_{\lambda_{succinate}^{(21AA)}}$, $\mu_{\lambda_{acetate}}$ $\sigma_{\lambda_{succinate}^{(21AA)}}$, $\sigma_{\lambda_{acetate}}$	$\lambda_{succinate}^{(21AA)}$ and $\lambda_{acetate}$ are the growth rates for succinate mixed with 21AA or acetate as the sole carbon source; $\mu_{\lambda_{succinate}^{(21AA)}}$, $\mu_{\lambda_{acetate}}$ and $\sigma_{\lambda_{succinate}^{(21AA)}}$, $\sigma_{\lambda_{acetate}}$ are the means and standard deviations of $\lambda_{succinate}^{(21AA)}$ and $\lambda_{acetate}$.	See Appendix 8.2.

Appendix-table 3 (continued)

$\boldsymbol{\phi_{MT}}$, $\boldsymbol{\kappa_{MT}}$	ϕ_{MT} and κ_{MT} are the proteomic mass fraction of the enzymes and the effective substrate quality of related metabolites in the mitochondria for yeast and mammalian cells, respectively.	NA
$\mathbf{Pr}_f$	The proportion of ATP generated from fermentation: $\mathrm{Pr}_f \equiv \frac{j_f^{(E)}}{j_f^{(E)}+j_r^{(E)}}$.	See Eqs. S180, S189 and Appendix 9.
$\bar{\boldsymbol{\Delta}}$	The proteome efficiency difference between respiration and fermentation: $\bar{\Delta} \equiv 1/\varepsilon_r - 1/\varepsilon_f$.	See Eqs. S181, S187 and Appendix 9.
$\boldsymbol{\mu_{\varepsilon_r}}$, $\boldsymbol{\mu_{\varepsilon_f}}$, $\boldsymbol{\mu_{1/\varepsilon_r}}$, $\boldsymbol{\mu_{1/\varepsilon_f}}$	μ_{ε_r}, μ_{ε_f}, μ_{1/ε_r} and μ_{1/ε_f} are the mean values of ε_r , ε_f, $1/\varepsilon_r$ and $1/\varepsilon_f$, respectively.	See Eqs. S182-S184 and Appendix 9.
$\boldsymbol{\sigma_{\varepsilon_r}}$, $\boldsymbol{\sigma_{\varepsilon_f}}$, $\boldsymbol{\sigma_{1/\varepsilon_r}}$, $\boldsymbol{\sigma_{1/\varepsilon_f}}$	σ_{ε_r}, σ_{ε_f}, σ_{1/ε_r} and σ_{1/ε_f} are the standard deviations of ε_r , ε_f, $1/\varepsilon_r$ and $1/\varepsilon_f$, respectively.	See Eqs. S182, S185 and Appendix 9.
$\boldsymbol{\chi_{\varepsilon_r}}$, $\boldsymbol{\chi_{\varepsilon_f}}$, $\boldsymbol{\chi_{1/\varepsilon_r}}$, $\boldsymbol{\chi_{1/\varepsilon_f}}$	χ_{ε_r}, χ_{ε_f}, χ_{1/ε_r} and χ_{1/ε_f} are the coefficients of variation of ε_r , ε_f, $1/\varepsilon_r$ and $1/\varepsilon_f$, respectively.	See Eqs. S185-S186 and Appendix 9.
$\boldsymbol{\mu_{\bar{\Delta}}}$, $\boldsymbol{\sigma_{\bar{\Delta}}}$	$\mu_{\bar{\Delta}}$ and $\sigma_{\bar{\Delta}}$ are the mean and standard deviation of $\bar{\Delta}$, respectively.	See Eqs. S187-S188 and Appendix 9.
$\boldsymbol{\langle\varepsilon_r\rangle}$, $\boldsymbol{\langle\varepsilon_f\rangle}$	$\langle\varepsilon_r\rangle$ and $\langle\varepsilon_f\rangle$ are the population-averaged values of ε_r and ε_f, respectively.	Measurable from experiments. See Eqs. S183-S184 and Appendix 9.

Appendix-table 3 (continued)

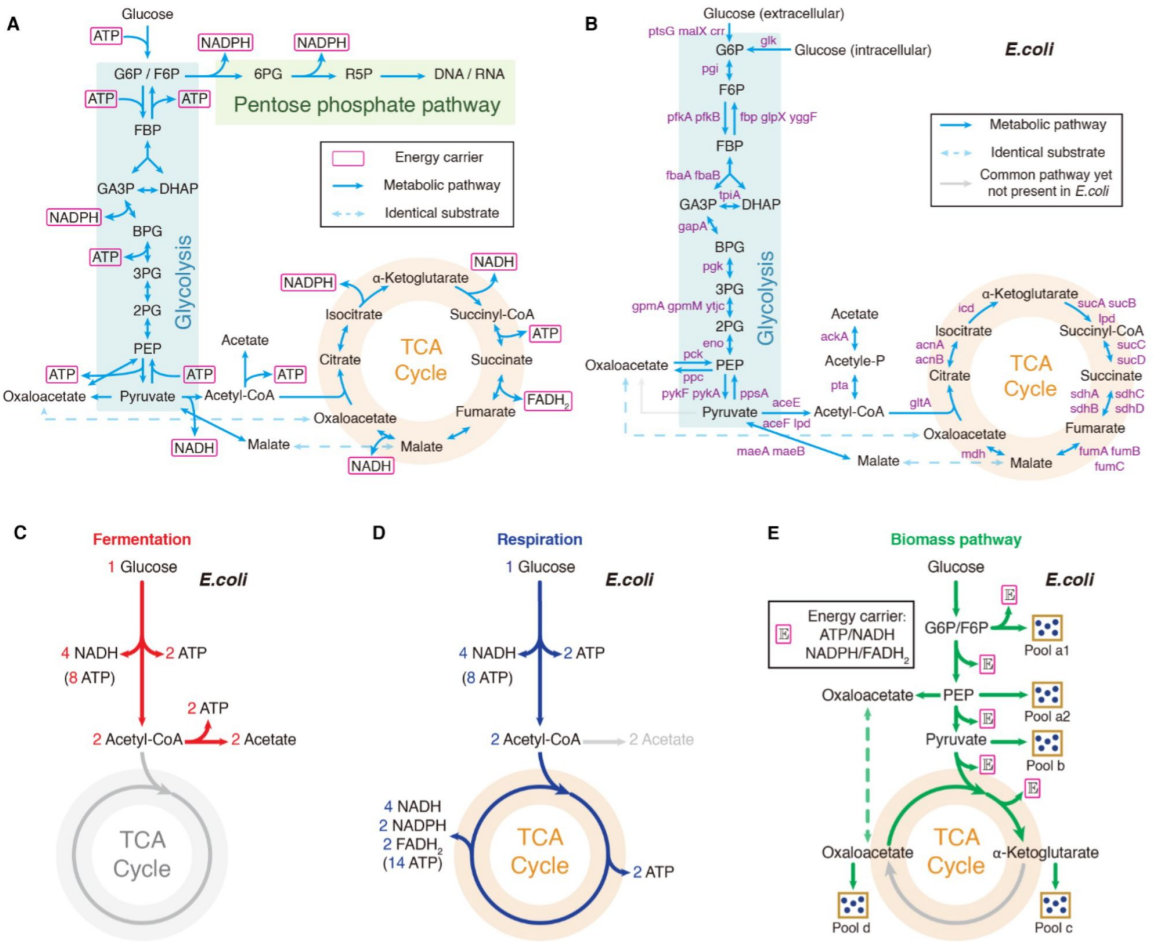

Appendix-figure 1

Central metabolic network and carbon utilization pathways of *E. coli*.

(**A**) Energy biogenesis details in the central metabolic network. In *E. coli*, NADPH and NADH are interconvertible (Sauer et al., 2004), and all energy carriers can be converted to ATP through ADP phosphorylation. The conversion factors are: NADH = 2ATP, NADPH = 2ATP, FADH2 = 1ATP (Neidhardt et al., 1990). (**B**) Relevant genes encoding enzymes in the central metabolic network of *E. coli*. (**C-E**) Three independent fates of glucose metabolism in *E. coli*. (**C**) For energy biogenesis through fermentation, a molecule of glucose generates 12 ATPs. (**D**) For energy biogenesis via respiration, a molecule of glucose generates 26 ATPs. (**E**) For biomass synthesis, glucose is converted into precursors of biomass. Note that biomass synthesis is accompanied by ATP production (see Appendix 2.1).

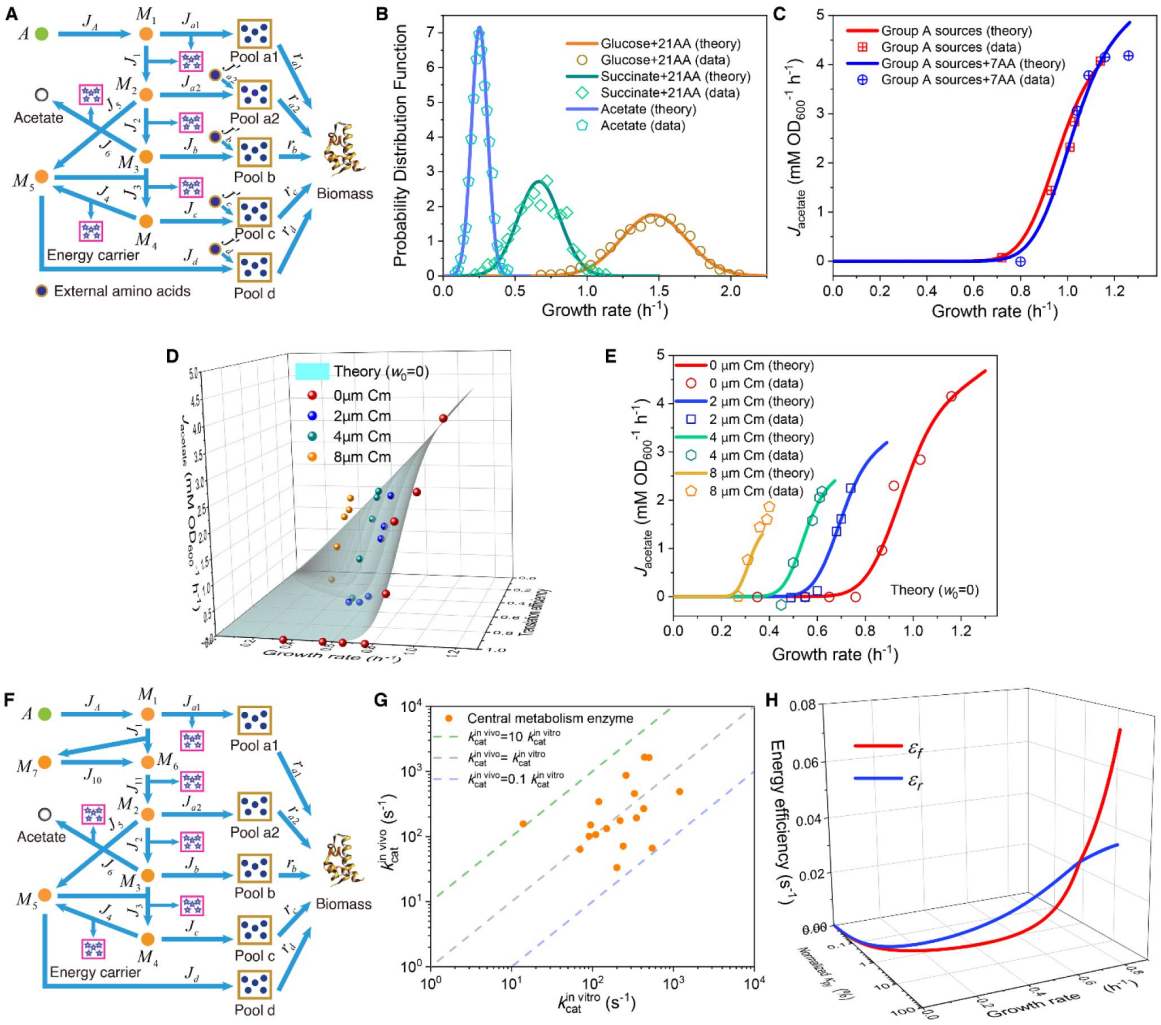

Appendix-figure 2

Model and results for experimental comparison of *E. coli*.

(**A-C**) Model analysis for carbon utilization in mixtures with amino acids. (**A**) Coarse-grained model for the case of a Group A carbon source mixed with extracellular amino acids. (**B**) Model predictions (Eqs. S157, S164–S165) and single-cell reference experimental results (Wallden et al., 2016) showing growth rate distributions for *E. coli* in three culturing conditions. (**C**) Comparison of the growth rate-fermentation flux relation for *E. coli* in Group A carbon sources between minimal media and enriched media (those with 7AA). (**D-E**) Influence of translation inhibition on overflow metabolism in *E. coli*. (**D**) A 3D plot illustrating the relations among fermentation flux, growth rate, and translation efficiency (Eqs. 79 and S160). (**E**) Growth rate dependence of acetate excretion rate as κ_A varies, with each fixed dose of Cm. Translation efficiency is tuned by the dose of Cm, and the maintenance energy coefficient is set to 0 (i.e., $w_0 = 0$). (**F**) Coarsegrained model for Group A carbon source utilization, which includes more details to compare with experiments. (**G**) Comparison of in vivo and in vitro catalytic rates for enzymes of *E. coli* within glycolysis and the TCA cycle (see **Appendix-table 1** for details). (**H**) The proteome efficiencies for energy biogenesis in the respiration and fermentation pathways vary with growth rate as functions of the substrate quality of pyruvate (Eqs. **S93** and **S96**).

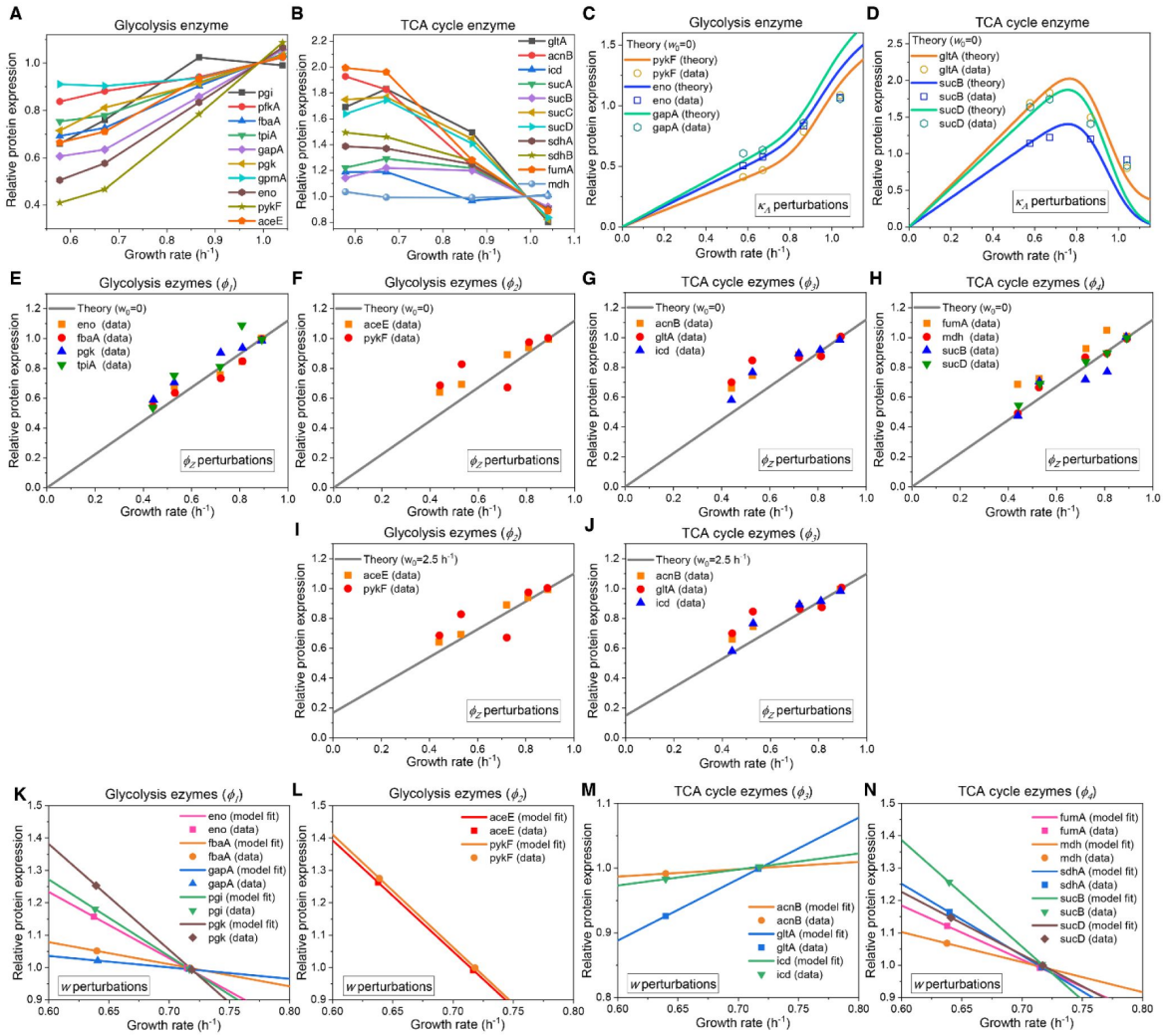

Appendix-figure 3

Relative protein expression of central metabolic enzymes in *E. coli* under various types of perturbations.

(A-D) Relative protein expression under κ_A perturbation. (**A**) Experimental data (Hui et al., 2015) for the catalytic enzymes at each step of glycolysis. (**B**) Experimental data (Hui et al., 2015) for the catalytic enzymes at each step of the TCA cycle. (**C**) Model predictions (Eq. S118, with $w_0 = 0$) and experimental data (Hui et al., 2015) for representative glycolytic genes. (**D**) Model predictions (Eq. S118, with $w_0 = 0$) and experimental data (Hui et al., 2015) for representative genes from the TCA cycle. **(E-J)** Relative protein expression under ϕ_Z perturbation. (**E**, **F**, **I**) Model predictions and experimental data (Basan et al., 2015) for representative glycolytic genes. (**G**, **H**, **J**) Model predictions and experimental data (Basan et al., 2015) for representative genes from the TCA cycle. (**E–H**) Results of ϕ_Z perturbation with $w_0 = 0$ (Eq. S120). (**I–J**) Results of ϕ_Z perturbation with $w_0 = 2.5$ (h^{-1}) (Eq. S121). **(K-N)** Relative protein expression upon energy dissipation. (**K–L**) Model fits (Eqs. S127 and S123) and experimental data (Basan et al., 2015) for representative glycolytic genes. (**M–N**) Model fits (Eqs. S127 and S123) and experimental data (Basan et al., 2015) for representative genes from the TCA cycle.

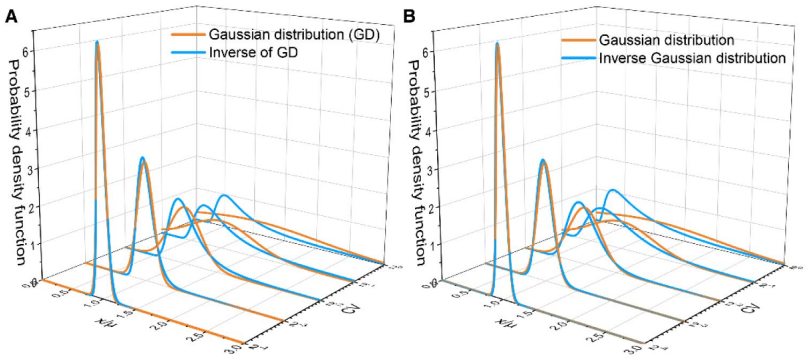

Appendix-figure 4

Asymptotic distributions of inverse Gaussian distribution and the inverse of Gaussian distribution.

(**A**) Comparison between the inverse of Gaussian distribution and the corresponding Gaussian distribution for various values of the coefficient of variation (CV) (Eqs. S140 and S145). (**B**) Comparison between the inverse Gaussian distribution and the corresponding Gaussian distribution for various values of CV (Eqs. S142 and S146). Both the inverse Gaussian distribution and the inverse of Gaussian distribution converge to Gaussian distributions when CV is small.

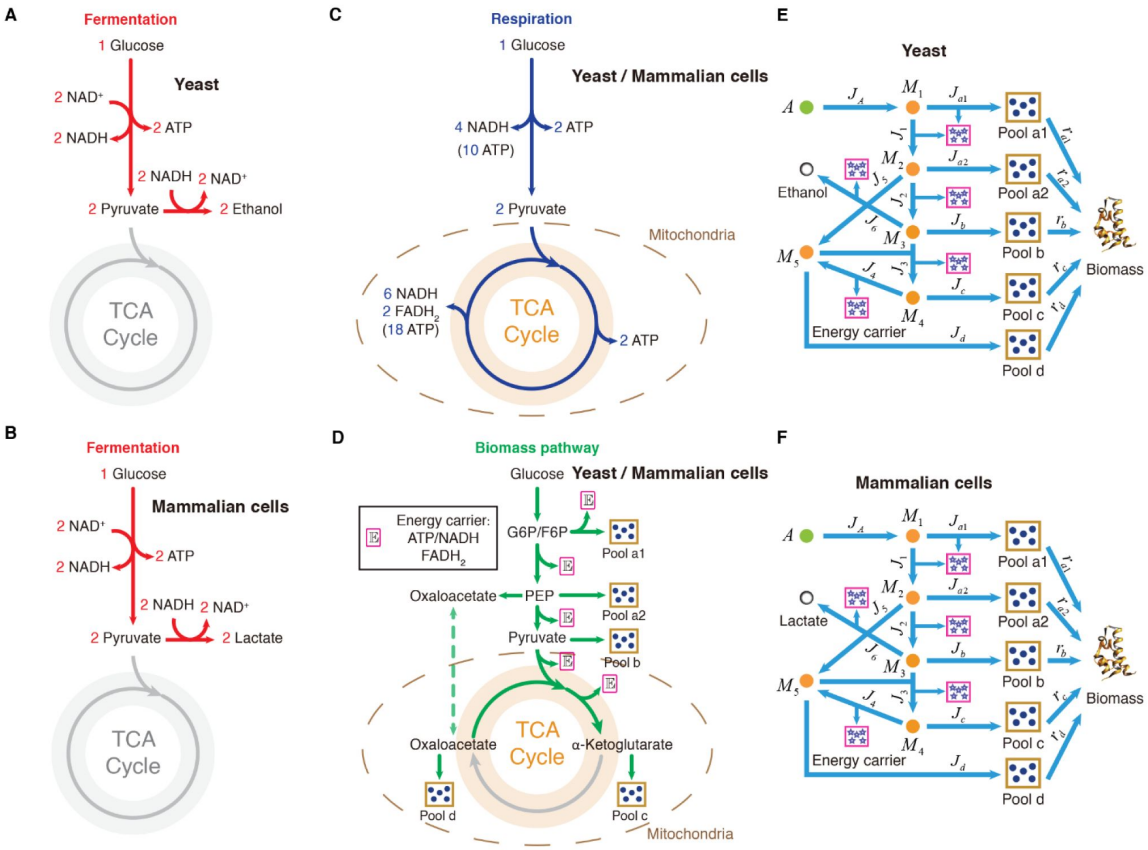

Appendix-figure 5

Carbon utilization in yeast and mammalian cells.

(**A-D**) Three independent fates of glucose metabolism in yeast and mammalian cells. (**A-B**) For energy biogenesis through fermentation, one molecule of glucose generates 2 ATPs. (**C**) For energy biogenesis through respiration, one molecule of glucose generates 32 ATPs. (**D**) For biomass synthesis, glucose is converted into biomass precursors, with ATP produced as a byproduct. In yeast and mammalian cells, the energy stored in NADH and FADH2 converts ADP into ATP in the mitochondria, with higher conversion factors than in *E. coli*: NADH = 2.5 ATP, $FADH_2$ = 1.5 ATP (Nelson et al., 2008). (**E**) Coarse-grained model for Group A carbon source utilization in yeast. (**F**) Coarse-grained model for Group A carbon source utilization in mammalian cells.

References

Ackermann M. (2015) **A functional perspective on phenotypic heterogeneity in microorganisms** *Nature Reviews Microbiology* **13**:497–508

Bagamery L.E., Justman Q.A., Garner E.C., Murray A.W. (2020) **A putative bet-hedging strategy buffers budding yeast against environmental instability** *Current Biology* **30**:4563–4578

Balaban N.Q., Merrin J., Chait R., Kowalik L., Leibler S. (2004) **Bacterial persistence as a phenotypic switch** *Science* **305**:1622–1625

Bartman C.R. *et al.* (2023) **Slow TCA flux and ATP production in primary solid tumours but not metastases** *Nature* **614**:349–357

Basan M. *et al.* (2020) **A universal trade-off between growth and lag in fluctuating environments** *Nature* **584**:470–474

Basan M., Hui S., Okano H., Zhang Z., Shen Y., Williamson J.R., Hwa T. (2015) **Overflow metabolism in Escherichia coli results from efficient proteome allocation** *Nature* **528**:99–104

Bennett B.D., Kimball E.H., Gao M., Osterhout R., Van Dien S.J., Rabinowitz J.D. (2009) **Absolute metabolite concentrations and implied enzyme active site occupancy in Escherichia coli** *Nature Chemical Biology* **5**:593–599

Chen Y., Nielsen J. (2019) **Energy metabolism controls phenotypes by protein efficiency and allocation** *Proceedings of the National Academy of Sciences* **116**:17592–17597

Dai X., Zhu M., Warren M., Balakrishnan R., Patsalo V., Okano H., Williamson J.R., Fredrick K., Wang Y.-P., Hwa T. (2016) **Reduction of translating ribosomes enables Escherichia coli to maintain elongation rates during slow growth** *Nature Microbiology* **2**:1–9

Davidi D., Noor E., Liebermeister W., Bar-Even A., Flamholz A., Tummler K., Barenholz U., Goldenfeld M., Shlomi T., Milo R. (2016) **Global characterization of in vivo enzyme catalytic rates and their correspondence to in vitro kcat measurements** *Proceedings of the National Academy of Sciences* **113**:3401–3406

De Deken R. (1966) **The Crabtree effect: a regulatory system in yeast** *Microbiology* **44**:149–156

DeBerardinis R.J., Chandel N. (2020) **We need to talk about the Warburg effect** *Nature Metabolism* **2**:127–129

Dekel E., Alon U. (2005) **Optimality and evolutionary tuning of the expression level of a protein** *Nature* **436**:588–592

Duraj T., García-Romero N., Carrión-Navarro J., Madurga R., Ortiz de Mendivil A., Prat-Acin R., Garcia-Cañamaque L., Ayuso-Sacido A. (2021) **Beyond the Warburg effect: Oxidative and glycolytic phenotypes coexist within the metabolic heterogeneity of glioblastoma** *Cells* **10**

Ebenhoh O., Ebeling J., Meyer R., Pohlkotte F., Nies T. (2024) **Microbial Pathway Thermodynamics: Stoichiometric Models Unveil Anabolic and Catabolic Processes** *Life* **14**

Edwards J.S., Ibarra R.U., Palsson B.O. (2001) **In silico predictions of Escherichia coli metabolic capabilities are consistent with experimental data** *Nature biotechnology* **19**:125–130

Elowitz M.B., Levine A.J., Siggia E.D., Swain P.S. (2002) **Stochastic gene expression in a single cell** *Science* **297**:1183–1186

Escalante-Chong R., Savir Y., Carroll S.M., Ingraham J.B., Wang J., Marx C.J., Springer M. (2015) **Galactose metabolic genes in yeast respond to a ratio of galactose and glucose** *Proceedings of the National Academy of Sciences* **112**:1636–1641

García-Contreras R., Vos P., Westerhoff H.V., Boogerd F.C. (2012) **Why in vivo may not equal in vitro-new effectors revealed by measurement of enzymatic activities under the same in vivo-like assay conditions** *The FEBS Journal* **279**:4145–4159

Hanahan D., Weinberg R.A. (2011) **Hallmarks of cancer: the next generation** *Cell* **144**:646–674

Hensley C.T. *et al.* (2016) **Metabolic heterogeneity in human lung tumors** *Cell* **164**:681–694

Holms H. (1996) **Flux analysis and control of the central metabolic pathways in Escherichia coli** *FEMS Microbiology Reviews* **19**:85–116

Hui S., Silverman J.M., Chen S.S., Erickson D.W., Basan M., Wang J., Hwa T., Williamson J.R. (2015) **Quantitative proteomic analysis reveals a simple strategy of global resource allocation in bacteria** *Molecular Systems Biology* **11**

Kostinski S., Reuveni S. (2020) **Ribosome composition maximizes cellular growth rates in E. coli** *Physical Review Letters* **125**

Kussell E., Leibler S. (2005) **Phenotypic diversity, population growth, and information in fluctuating environments** *Science* **309**:2075–2078

Li S.H.-J., Li Z., Park J.O., King C.G., Rabinowitz J.D., Wingreen N.S., Gitai Z. (2018) **Escherichia coli translation strategies differ across carbon, nitrogen and phosphorus limitation conditions** *Nature Microbiology* **3**:939–947

Liberti M.V., Locasale J.W. (2016) **The Warburg effect: how does it benefit cancer cells?** *Trends in Biochemical Sciences* **41**:211–218

Liu X., Wang X., Yang X., Liu S., Jiang L., Qu Y., Hu L., Ouyang Q., Tang C. (2015) **Reliable cell cycle commitment in budding yeast is ensured by signal integration** *eLife* **4**

Locasale J.W., Cantley L.C. (2010) **Altered metabolism in cancer** *BMC biology* **8**

Majewski R., Domach M. (1990) **Simple constrained-optimization view of acetate overflow in E. coli** *Biotechnology Bioengineering* **35**:732–738

Meyer H.-P., Leist C., Fiechter A. (1984) **Acetate formation in continuous culture of Escherichia coli K12 D1 on defined and complex media** *Journal of Biotechnology* **1**:355–358

Molenaar D., Van Berlo R., De Ridder D., Teusink B. (2009) **Shifts in growth strategies reflect tradeoffs in cellular economics** *Molecular Systems Biology* **5**

Mori M., Schink S., Erickson D.W., Gerland U., Hwa T. (2017) **Quantifying the benefit of a proteome reserve in fluctuating environments** *Nature Communications* **8**

Müller S., Regensburger G., Steuer R. (2014) **Enzyme allocation problems in kinetic metabolic networks: Optimal solutions are elementary flux modes** *Journal of Theoretical Biology* **347**:182–190

Nanchen A., Schicker A., Sauer U. (2006) **Nonlinear dependency of intracellular fluxes on growth rate in miniaturized continuous cultures of Escherichia coli** *Applied Environmental Microbiology* **72**:1164–1172

Neidhardt F.C. (1996) **Escherichia coli and Salmonella: cellular and molecular biology** Washington, DC: ASM Press

Neidhardt F.C., Ingraham J.L., Schaechter M. (1990) **Physiology of the bacterial cell** Sinauer associates

Nelson D.L., Lehninger A.L., Cox M.M. (2008) **Lehninger principles of biochemistry** Macmillan

Niebel B., Leupold S., Heinemann M. (2019) **An upper limit on Gibbs energy dissipation governs cellular metabolism** *Nature Metabolism* **1**:125–132

Nikolic N., Barner T., Ackermann M. (2013) **Analysis of fluorescent reporters indicates heterogeneity in glucose uptake and utilization in clonal bacterial populations** *BMC Microbiology* **13**:1–13

Park J.O., Rubin S.A., Xu Y.-F., Amador-Noguez D., Fan J., Shlomi T., Rabinowitz J.D. (2016) **Metabolite concentrations, fluxes and free energies imply efficient enzyme usage** *Nature Chemical Biology* **12**:482–489

Peebo K., Valgepea K., Maser A., Nahku R., Adamberg K., Vilu R. (2015) **Proteome reallocation in Escherichia coli with increasing specific growth rate** *Molecular BioSystems* **11**:1184–1193

Pfeiffer T., Schuster S., Bonhoeffer S. (2001) **Cooperation and competition in the evolution of ATP-producing pathways** *Science* **292**:504–507

Scott M., Gunderson C.W., Mateescu E.M., Zhang Z., Hwa T. (2010) **Interdependence of cell growth and gene expression: origins and consequences** *Science* **330**:1099–1102

Shen Y. *et al.* (2024) **Mitochondrial ATP generation is more proteome efficient than glycolysis** *Nature Chemical Biology* **20**:1123–1132

Shlomi T., Benyamini T., Gottlieb E., Sharan R., Ruppin E. (2011) **Genome-scale metabolic modeling elucidates the role of proliferative adaptation in causing the Warburg effect** *PLoS Computational Biology* **7**

Solopova A., Van Gestel J., Weissing F.J., Bachmann H., Teusink B., Kok J., Kuipers O.P. (2014) **Bet-hedging during bacterial diauxic shift** *Proceedings of the National Academy of Sciences* **111**:7427–7432

Towbin B.D., Korem Y., Bren A., Doron S., Sorek R., Alon U. (2017) **Optimality and sub-optimality in a bacterial growth law** *Nature Communications* **8**

van Hoek P., Flikweert M.T., van der Aart Q.J., Steensma H.Y., van Dijken J.P., Pronk J.T. (1998) **Effects of pyruvate decarboxylase overproduction on flux distribution at the pyruvate branch point in Saccharomyces cerevisiae** *Applied and environmental microbiology* **64**:2133–2140

Vander Heiden M.G., Cantley L.C., Thompson C.B. (2009) **Understanding the Warburg effect: the metabolic requirements of cell proliferation** *Science* **324**:1029–1033

Varma A., Palsson B.O. (1994) **Stoichiometric flux balance models quantitatively predict growth and metabolic by-product secretion in wild-type Escherichia coli W3110** *Applied Environmental Microbiology* **60**:3724–3731

Vazquez A., Liu J., Zhou Y., Oltvai Z.N. (2010) **Catabolic efficiency of aerobic glycolysis: the Warburg effect revisited** *BMC Systems Biology* **4**

Vazquez A., Oltvai Z.N. (2016) **Macromolecular crowding explains overflow metabolism in cells** *Scientific Reports* **6**

Wallden M., Fange D., Lundius E.G., Baltekin Ö., Elf J. (2016) **The synchronization of replication and division cycles in individual E. coli cells** *Cell* **166**:729–739

Wang X., Xia K., Yang X., Tang C. (2019) **Growth strategy of microbes on mixed carbon sources** *Nature Communications* **10**

Warburg O., Posener K., Negelein E. (1924) **Über den Stoffwechsel der Carcinomzelle** *Biochemische Zeitschrift* **152**:309–344

Wortel M.T., Peters H., Hulshof J., Teusink B., Bruggeman F.J. (2014) **Metabolic states with maximal specific rate carry flux through an elementary flux mode** *The FEBS Journal* **281**:1547–1555

Yaginuma H., Kawai S., Tabata K.V., Tomiyama K., Kakizuka A., Komatsuzaki T., Noji H., Imamura H. (2014) **Diversity in ATP concentrations in a single bacterial cell population revealed by quantitative single-cell imaging** *Scientific reports* **4**

You C., Okano H., Hui S., Zhang Z., Kim M., Gunderson C.W., Wang Y.-P., Lenz P., Yan D., Hwa T. (2013) **Coordination of bacterial proteome with metabolism by cyclic AMP signalling** *Nature* **500**:301–306

Zhang Z., Milias-Argeitis A., Heinemann M. (2018) **Dynamic single-cell NAD (P) H measurement reveals oscillatory metabolism throughout the E. coli cell division cycle** *Scientific Reports* **8**

Zhuang K., Vemuri G.N., Mahadevan R. (2011) **Economics of membrane occupancy and respiro-fermentation** *Molecular Systems Biology* **7**

Bagamery L.E., Justman Q.A., Garner E.C., Murray A.W. (2020) **A putative bet-hedging strategy buffers budding yeast against environmental instability** *Current Biology* **30**:4563–4578

Bartman C.R. *et al.* (2023) **Slow TCA flux and ATP production in primary solid tumours but not metastases** *Nature* **614**:349–357

Basan M. *et al.* (2020) **A universal trade-off between growth and lag in fluctuating environments** *Nature* **584**:470–474

Basan M., Hui S., Okano H., Zhang Z., Shen Y., Williamson J.R., Hwa T. (2015) **Overflow metabolism in Escherichia coli results from efficient proteome allocation** *Nature* **528**:99–104

Bennett B.D., Kimball E.H., Gao M., Osterhout R., Van Dien S.J., Rabinowitz J.D. (2009) **Absolute metabolite concentrations and implied enzyme active site occupancy in Escherichia coli** *Nature Chemical Biology* **5**:593–599

Chen Y., Nielsen J. (2019) **Energy metabolism controls phenotypes by protein efficiency and allocation** *Proceedings of the National Academy of Sciences* **116**:17592–17597

Dai X., Zhu M., Warren M., Balakrishnan R., Patsalo V., Okano H., Williamson J.R., Fredrick K., Wang Y.-P., Hwa T. (2016) **Reduction of translating ribosomes enables Escherichia coli to maintain elongation rates during slow growth** *Nature Microbiology* **2**:1–9

Davidi D., Noor E., Liebermeister W., Bar-Even A., Flamholz A., Tummler K., Barenholz U., Goldenfeld M., Shlomi T., Milo R. (2016) **Global characterization of in vivo enzyme catalytic rates and their correspondence to in vitro kcat measurements** *Proceedings of the National Academy of Sciences* **113**:3401–3406

Donachie W.D. (1968) **Relationship between cell size and time of initiation of DNA replication** *Nature* **219**:1077–1079

Duraj T., García-Romero N., Carrión-Navarro J., Madurga R., Ortiz de Mendivil A., Prat-Acin R., Garcia-Cañamaque L., Ayuso-Sacido A. (2021) **Beyond the Warburg effect: Oxidative and glycolytic phenotypes coexist within the metabolic heterogeneity of glioblastoma** *Cells* **10**

Elowitz M.B., Levine A.J., Siggia E.D., Swain P.S. (2002) **Stochastic gene expression in a single cell** *Science* **297**:1183–1186

Folks J.L., Chhikara R.S. (1978) **The inverse Gaussian distribution and its statistical application—a review** *Journal of the Royal Statistical Society: Series B* **40**:263–275

García-Contreras R., Vos P., Westerhoff H.V., Boogerd F.C. (2012) **Why in vivo may not equal in vitro-new effectors revealed by measurement of enzymatic activities under the same in vivo-like assay conditions** *The FEBS Journal* **279**:4145–4159

Gillespie D.T. (2000) **The chemical Langevin equation** *The Journal of Chemical Physics* **113**:297–306

Hanahan D., Weinberg R.A. (2011) **Hallmarks of cancer: the next generation** *Cell* **144**:646–674

Hensley C.T. *et al.* (2016) **Metabolic heterogeneity in human lung tumors** *Cell* **164**:681–694

Holms H. (1996) **Flux analysis and control of the central metabolic pathways in Escherichia coli** *FEMS Microbiology Reviews* **19**:85–116

Hui S., Silverman J.M., Chen S.S., Erickson D.W., Basan M., Wang J., Hwa T., Williamson J.R. (2015) **Quantitative proteomic analysis reveals a simple strategy of global resource allocation in bacteria** *Molecular Systems Biology* **11**

Kussell E., Leibler S. (2005) **Phenotypic diversity, population growth, and information in fluctuating environments** *Science* **309**:2075–2078

Locasale J.W., Cantley L.C. (2010) **Altered metabolism in cancer** *BMC biology* **8**

Majewski R., Domach M. (1990) **Simple constrained-optimization view of acetate overflow in E. coli** *Biotechnology Bioengineering* **35**:732–738

Meyer H.-P., Leist C., Fiechter A. (1984) **Acetate formation in continuous culture of Escherichia coli K12 D1 on defined and complex media** *Journal of Biotechnology* **1**:355–358

Milo R., Phillips R. (2015) **Cell biology by the numbers** Garland Science

Molenaar D., Van Berlo R., De Ridder D., Teusink B. (2009) **Shifts in growth strategies reflect tradeoffs in cellular economics** *Molecular Systems Biology* **5**

Mori M., Schink S., Erickson D.W., Gerland U., Hwa T. (2017) **Quantifying the benefit of a proteome reserve in fluctuating environments** *Nature Communications* **8**

Nanchen A., Schicker A., Sauer U. (2006) **Nonlinear dependency of intracellular fluxes on growth rate in miniaturized continuous cultures of Escherichia coli** *Applied Environmental Microbiology* **72**:1164–1172

Neidhardt F.C. (1996) **Escherichia coli and Salmonella: cellular and molecular biology** Washington, DC: ASM Press

Neidhardt F.C., Ingraham J.L., Schaechter M. (1990) **Physiology of the bacterial cell** Sinauer associates

Nelson D.L., Lehninger A.L., Cox M.M. (2008) **Lehninger principles of biochemistry** Macmillan

Niebel B., Leupold S., Heinemann M. (2019) **An upper limit on Gibbs energy dissipation governs cellular metabolism** *Nature Metabolism* **1**:125–132

Park J.O., Rubin S.A., Xu Y.-F., Amador-Noguez D., Fan J., Shlomi T., Rabinowitz J.D. (2016) **Metabolite concentrations, fluxes and free energies imply efficient enzyme usage** *Nature Chemical Biology* **12**:482–489

Peebo K., Valgepea K., Maser A., Nahku R., Adamberg K., Vilu R. (2015) **Proteome reallocation in Escherichia coli with increasing specific growth rate** *Molecular BioSystems* **11**:1184–1193

Sauer U., Canonaco F., Heri S., Perrenoud A., Fischer E. (2004) **The soluble and membrane-bound transhydrogenases UdhA and PntAB have divergent functions in NADPH metabolism of Escherichia coli** *Journal of Biological Chemistry* **279**:6613–6619

Scott M., Gunderson C.W., Mateescu E.M., Zhang Z., Hwa T. (2010) **Interdependence of cell growth and gene expression: origins and consequences** *Science* **330**:1099–1102

Shen Y. *et al.* (2024) **Mitochondrial ATP generation is more proteome efficient than glycolysis** *Nature Chemical Biology*

Shlomi T., Benyamini T., Gottlieb E., Sharan R., Ruppin E. (2011) **Genome-scale metabolic modeling elucidates the role of proliferative adaptation in causing the Warburg effect** *PLoS Computational Biology* **7**

Stevenson K., McVey A.F., Clark I.B., Swain P.S., Pilizota T. (2016) **General calibration of microbial growth in microplate readers** *Scientific Reports* **6**:1–7

Van Kampen N.G. (1992) **Stochastic processes in physics and chemistry** Elsevier

Vander Heiden M.G., Cantley L.C., Thompson C.B. (2009) **Understanding the Warburg effect: the metabolic requirements of cell proliferation** *Science* **324**:1029–1033

Varma A., Palsson B.O. (1994) **Stoichiometric flux balance models quantitatively predict growth and metabolic by-product secretion in wild-type Escherichia coli W3110** *Applied Environmental Microbiology* **60**:3724–3731

Vazquez A., Liu J., Zhou Y., Oltvai Z.N. (2010) **Catabolic efficiency of aerobic glycolysis: the Warburg effect revisited** *BMC Systems Biology* **4**

Vazquez A., Oltvai Z.N. (2016) **Macromolecular crowding explains overflow metabolism in cells** *Scientific Reports* **6**

Wallden M., Fange D., Lundius E.G., Baltekin O., Elf J. (2016) **The synchronization of replication and division cycles in individual E. coli cells** *Cell* **166**:729–739

Wang X., Xia K., Yang X., Tang C. (2019) **Growth strategy of microbes on mixed carbon sources** *Nature Communications* **10**

Zhuang K., Vemuri G.N., Mahadevan R. (2011) **Economics of membrane occupancy and respiro-fermentation** *Molecular Systems Biology* **7**

Author information

Xin Wang
School of Physics, Sun Yat-sen University, Guangzhou, China

For correspondence: wangxin36@mail.sysu.edu.cn

Editors

Reviewing Editor
Marisa Nicolás
Laboratório Nacional de Computação Científica, Rio de Janeiro, Brazil

Senior Editor
Aleksandra Walczak
École Normale Supérieure - PSL, Paris, France

Reviewer #1 (Public review):

Summary:

Cell metabolism exhibits a well-known behavior in fast-growing cells, which employ seemingly wasteful fermentation to generate energy even in the presence of sufficient environmental oxygen. This phenomenon is known as Overflow Metabolism or the Warburg effect in cancer. It is present in a wide range of organisms, from bacteria and fungi to mammalian cells.

In this work, starting with a metabolic network for Escherichia coli based on sets of carbon sources, and using a corresponding coarse-grained model, the author applies some well-based approximations from the literature and algebraic manipulations. These are used to successfully explain the origins of Overflow Metabolism, both qualitatively and quantitatively, by comparing the results with E. coli experimental data.

By modeling the proteome energy efficiencies for respiration and fermentation, the study shows that these parameters are dependent on the carbon source quality constants K_i (p.115 and 116). It is demonstrated that as the environment becomes richer, the optimal solution for proteome energy efficiency shifts from respiration to fermentation. This shift occurs at a critical parameter value K_A(C).
This counter intuitive results qualitativelly explains Overflow Metabolism.

Quantitative agreement is achieved through the analysis of the heterogeneity of the metabolic status within a cell population. By introducing heterogeneity, the critical growth rate is assumed to follow a Gaussian distribution over the cell population, resulting in accordance with experimental data for E. coli. Overflow metabolism is explained by considering optimal protein allocation and cell heterogeneity.

The obtained model is extensively tested through perturbations: 1) Introduction of overexpression of useless proteins; 2) Studying energy dissipation; 3) Analysis of the impact of translation inhibition with different sub-lethal doses of chloramphenicol on Escherichia coli; 4) Alteration of nutrient categories of carbon sources using pyruvate. All model perturbations results are corroborated by E. coli experimental results.

Strengths:

In this work, the author effectively uses modeling techniques typical of Physics to address complex problems in Biology, demonstrating the potential of interdisciplinary approaches to yield novel insights. The use of Escherichia coli as a model organism ensures that the assumptions and approximations are well-supported in existing literature. The model is convincingly constructed and aligns well with experimental data, lending credibility to the findings. In this version, the extension of results from bacteria to yeast and cancer is substantiated by a literature base, suggesting that these findings may have broad implications for understanding diverse biological systems.

Weaknesses:

The author explores the generalization of their results from bacteria to cancer cells and yeast, adapting the metabolic network and coarse-grained model accordingly. In previous version this generalization was not completedly supported by references and data from the literature. This drawback, however, has been treated in this current version, where the authors discuss in much more detail and give references supporting this generalization.

https://doi.org/10.7554/eLife.94586.2.sa2

Reviewer #2 (Public review):

In this version of manuscript, the author clarified many details and rewrote some sections. This substantially improved the readability of the paper. I also recognized that the author spent substantial efforts in the Appendix to answer the potential questions.

Unfortunately, I am not currently convinced by the theory proposed in this paper. In the next section, I will first recap the logic of the author and explain why I am not convinced. Although the theory fits many experimental results, other theories on overflow metabolism are also supported by experiments. Hence, I do not think based on experimental data we could rule in or rule out different theories.

Recap: To explain the origin of overflow metabolism, the author uses the following logic:

(1) There is a substantial variability of single-cell growth rate
(2) The flux (J_r^E) and (J_f^E) are coupled with growth rate by Eq. 3
(3) Since growth rate varies from cells to cells, flux (J_r^E) and (J_f^E) also varies
(4) The variabilities of above fluxes in above create threshold-analog relation, and hence overflow metabolism.

My opinion:

The logic step (2) and (3) have caveats. The variability of growth rate has large components of cellular noise and external noise. Therefore, variability of growth rate is far from 100% correlated with variability of flux (J_r^E) and (J_f^E) at the single-cell level. Single-cell growth rate is a complex, multivariate functional, including (Jr^E) and (J_f^E) but also many other variables. My feeling is the correlation could be too low to support the logic here.

One example: ribosomal concentration is known to be an important factor of growth rate in bulk culture. However, the "growth law" from bulk culture cannot directly translate into the growth law at single-cell level [Ref1,2]. This is likely due to other factors (such as cell aging, other muti-stability of cellular states) are involved.

Therefore, I think using Eq.3 to invert the distribution of growth rate into the distribution of (Jr^E) and (J_f^E) is inapplicable, due to the potentially low correlation at single-cell level. It may show partial correlations, but may not be strong enough to support the claim and create fermentation at macroscopic scale.

Overall, if we track the logic flow, this theory implies overflow metabolism is originated from variability of k_cat of catalytic enzymes from cells to cells. That is, the author proposed that overflow metabolism happens macroscopically as if it is some "aberrant activation of fermentation pathway" at the single-cell level, due to some unknown partially correlation from growth rate variability.

Compared with other theories, this theory does not involve any regulatory mechanism and can be regarded as a "neutral theory". I am looking forward to seeing single cell experiments in the future to provide evidences about this theory.

[Ref1] https://www.biorxiv.org/content/10.1101/2024.04.19.590370v2
[Ref2] https://www.biorxiv.org/content/10.1101/2024.10.08.617237v2

https://doi.org/10.7554/eLife.94586.2.sa1

Author response:

The following is the authors' response to the original reviews.

> ***Reviewer #1 (Public Review):***
>
> *Summary:*
>
> *Cell metabolism exhibits a well-known behavior in fast-growing cells, which employ seemingly wasteful fermentation to generate energy even in the presence of sufficient environmental oxygen. This phenomenon is known as Overflow Metabolism or the Warburg effect in cancer. It is present in a wide range of organisms, from bacteria and fungi to mammalian cells.*
>
> *In this work, starting with a metabolic network for Escherichia coli based on sets of carbon sources, and using a corresponding coarse-grained model, the author applies some well-based approximations from the literature and algebraic manipulations. These are used to successfully explain the origins of Overflow Metabolism, both qualitatively and quantitatively, by comparing the results with E. coli experimental data.*
>
> *By modeling the proteome energy efficiencies for respiration and fermentation, the study shows that these parameters are dependent on the carbon source quality constants K_i (p.115 and 116). It is demonstrated that as the environment becomes richer, the optimal solution for proteome energy efficiency shifts from respiration to fermentation. This shift occurs at a critical parameter value K_A(C).*
>
> *This counterintuitive result qualitatively explains Overflow Metabolism.*
>
> *Quantitative agreement is achieved through the analysis of the heterogeneity of the metabolic status within a cell population. By introducing heterogeneity, the critical growth rate is assumed to follow a Gaussian distribution over the cell population, resulting in accordance with experimental data for E. coli. Overflow metabolism is explained by considering optimal protein allocation and cell heterogeneity.*
>
> *The obtained model is extensively tested through perturbations: 1) Introduction of overexpression of useless proteins; 2) Studying energy dissipation; 3) Analysis of the impact of translation inhibition with different sub-lethal doses of chloramphenicol on Escherichia coli; 4) Alteration of nutrient categories of carbon sources using pyruvate. All model perturbation results are corroborated by E. coli experimental results.*

We appreciate the reviewer's highly positive comments and the accurate summary of our manuscript.

> *Strengths:*
>
> *In this work, the author employs modeling methods typical of Physics to address a problem in Biology, standing at the interface between these two scientific fields. This interdisciplinary approach proves to be highly fruitful and should be further explored in the literature. The use of Escherichia coli as an example ensures that all hypotheses and approximations in this study are well-founded in the literature. Examples include the approximation for the Michaelis-Menten equation (line 82), Eq. S1, proteome partition in Appendix 1.1 (lines 68-69), and a stable nutrient environment in Appendix 1.1 (lines 83-84). The section "Testing the model through perturbation" heavily relies on bacterial data. The construction of the model and its agreement with experimental data are convincingly presented.*

We appreciate the reviewer's highly positive comments. We have incorporated many of the reviewer's insightful suggestions and added citations in the appropriate contexts, which have significantly improved our manuscript.

> *Weaknesses:*
>
> *In Section Appendix 6.4, the author explores the generalization of results from bacteria to cancer cells, adapting the metabolic network and coarse-grained model accordingly. It is argued that as a consequence, all subsequent steps become immediately valid. However, I remain unconvinced, considering the numerous approximations used to derive the equations, which the literature demonstrates to be valid primarily for bacteria. A more detailed discussion about this generalization is recommended. Additionally, it is crucial to note that the experimental validation of model perturbations heavily relies on E. coli data.*

We appreciate the reviewer's insightful suggestions. We apologize for not clearly illustrating the generalization of results from bacteria to cancer cells in the previous version of our manuscript. Indeed, in our earlier version, there was no experimental validation of model results related to cancer cells.

Following the reviewer's suggestions, we have now added Fig. 5 and Appendix-fig. 5, fully expanded the previous Appendix 6.4 into Appendix 9 in our current version, and added a new section entitled "Explanation of the Crabtree effect in yeast and the Warburg effect in cancer cells" in our main text to provide a detailed discussion of the generalization from bacteria to yeast and cancer cells. Through the derivations shown in Appendix 9 (Eqs. S180-S189), we arrived at Eq. 6 (or Eq. S190 in Appendix 9) to facilitate the comparison of our model results with experimental data in yeast and cancer cells. This comparison is presented in Fig. 5, where we demonstrate that our model can quantitatively explain the data for the Crabtree effect in yeast and the Warburg effect in cancer cells (related experimental data references: Shen et al., Nature Chemical Biology 20, 1123–1132 (2024); Bartman et al., Nature 614, 349-357 (2023)). These additions have significantly strengthened our manuscript.

> ***Reviewer #2 (Public Review):***
>
> *Summary*
>
> *This paper has three parts. The first part applied a coarse-grained model with proteome partition to calculate cell growth under respiration and fermentation modes. The second part considered single-cell variability and performed population average to acquire an ensemble metabolic profile for acetate fermentation. The third part used model and simulation to compare experimental data in literature and obtained substantial consistency.*

We thank the reviewer for the accurate summary and positive comments on our manuscript.

> *Strengths and major contributions*
>
> *(i) The coarse-grained model considered specific metabolite groups and their interrelations and acquired an analytical solution for this scenario. The "resolution" of this model is in between the Flux Balanced Analysis/whole-cell simulation and proteome partition analysis.*
>
> *(ii) The author considered single-cell level metabolic heterogeneity and calculated the ensemble average with explicit calculation. The results are consistent with known fermentation and growth phenomena qualitatively and can be quantitatively compared to experimental results.*

We appreciate the reviewer's highly positive comments.

Weaknesses

(i) If I am reading this paper correctly, the author's model predicts binary (or "digital") outcomes of single-cell metabolism, that is, after growth rate optimization, each cell will adopt either "respiration mode" or "fermentation mode" (as illustrated in Figure Appendix - Figure 1 C, D). Due to variability enzyme activity k_i^{cat} and critical growth rate λ_C, each cell under the same nutrient condition could have either respiration or fermentation, but the choice is binary.

The binary choice at the single-cell level is inconsistent with our current understanding of metabolism. If a cell only uses fermentation mode (as shown in Appendix - Figure 1C), it could generate enough energy but not be able to have enough metabolic fluxes to feed into the TCA cycle. That is, under pure fermentation mode, the cell cannot expand the pool of TCA cycle metabolites and hence cannot grow.

*This caveat also appears in the model in Appendix (S25) that assumes J_E = r_E*J_{BM} where r_E is a constant. From my understanding, r_E can be different between respiration and fermentation modes (at least for real cells) and hence it is inappropriate to conclude that cells using fermentation, which generates enough energy, can also generate a balanced biomass.*

We thank the reviewer for raising this question. Indeed, regarding energy biogenesis between respiration and fermentation, our model predicts binary outcomes at the single-cell level. However, this outcome does not hinder cell growth, as there are three independent possible fates for the carbon source (e.g., glucose) in metabolism: fermentation, respiration for energy biogenesis, and biomass generation. Each fate is associated with a distinct fraction of the proteome, with no overlap between them (see Appendix-figs. 1 and 5). Consequently, in a purely fermentative mode, a cell can still use the proteome dedicated to the biomass generation pathway to produce biomass precursors via the TCA cycle.

The classification of the carbon source's fates into three independent pathways was initially introduced by Chen and Nielsen (Chen and Nielsen, PNAS 116, 17592-17597 (2019)). We apologize for the oversight in not citing their paper in this context in the previous version of our manuscript (although it was cited elsewhere). We have now included the citation in all appropriate places.

To illustrate this issue more clearly, we explicitly present the proteome allocation results for optimal growth in a fermentation mode below, where the proteome efficiency (i.e., the proteome energy efficiency in our previous version) in fermentation is higher than in respiration (i.e., $\varepsilon_f > \varepsilon_r$). We use the model shown in Fig. 1B as an example, with the relevant equations being Eqs. S26 and S28 in Appendix 2.1. By substituting Eq. S28 into Eq. S26, we arrive at Eq. 3 (or Eq. S29 in Appendix 2.1), which we restate here as Eq. R1:

$$\begin{cases} J_r^{(\mathrm{E})} + J_f^{(\mathrm{E})} = \varphi \cdot \lambda, \\ \dfrac{J_r^{(\mathrm{E})}}{\varepsilon_r} + \dfrac{J_f^{(\mathrm{E})}}{\varepsilon_f} = \phi_{\max} - \psi \cdot \lambda. \end{cases} \qquad \text{(R1)}$$

For a given nutrient condition, i.e., for a specific value of κ_A at the single-cell level, the values of ε_r, ε_f, ψ are determined (see Eqs. S20, S27, S31 and S32), while φ and $\phi_{\max}$ are

constants (see Eq. S33 and Appendix 1.1). Therefore, if $\varepsilon_f > \varepsilon_r$, then

$(\psi + \varphi/\varepsilon_f)\cdot\lambda = \phi_{\max} - J_r^{(\Xi)}(1/\varepsilon_r - 1/\varepsilon_f) \le \phi_{\max}$, since all coefficients are positive (i.e., $\varepsilon_r,\ \varepsilon_f,\ \psi,\ \varphi > 0$) and $J_r^{(\Xi)}$ takes non-negative values. Hence, the solution for optimal growth is (see Eqs. S35-S36 in Appendix 2.2):

$$\begin{cases} J_f^{(\Xi)} = \varphi\cdot\lambda = \dfrac{\varphi\cdot\phi_{\max}}{\varphi/\varepsilon_f + \psi}, \\ J_r^{(\Xi)} = 0, \\ \lambda = \dfrac{\phi_{\max}}{\varphi/\varepsilon_f + \psi}. \end{cases} \quad \text{(R2)}$$

Here, the result $J_r^{(\Xi)} = 0$ signifies a pure fermentation mode with no respiration flux for energy biogenesis. Then, by combining Eq. R2 with Eqs. S28 and S30 from Appendix 2.1, we obtain the optimal proteome allocation results for this case:

$$\begin{cases} \phi_A = \left[\varphi/\beta_f^{(A)} + \eta_{a1} + \eta_c + (\eta_{a2} + \eta_b + \eta_d)/2\right]\cdot\lambda/\kappa_A, \\ \phi_1 = \left[\varphi/\beta_f^{(A)} + \eta_c + (\eta_{a2} + \eta_b + \eta_d)/2\right]\cdot\lambda/\kappa_1, \\ \phi_2 = \left(2\varphi/\beta_f^{(A)} + \eta_b + \eta_c\right)\cdot\lambda/\kappa_2, \\ \phi_3 = \eta_c\cdot\lambda/\kappa_3,\ \phi_4 = 0, \\ \phi_5 = (\eta_c + \eta_d)\cdot\lambda/\kappa_5,\ \phi_6 = 2\varphi\cdot\lambda/\left(\beta_f^{(A)}\cdot\kappa_6\right), \\ \phi_i = \eta_i\cdot\lambda/\kappa_i \quad (i = a1,\ a2,\ b,\ c,\ d), \end{cases} \quad \text{(R3)}$$

where $\lambda = \dfrac{\phi_{\max}}{\varphi/\varepsilon_f + \psi}$, while κ_A and $\kappa_i\ (i = 1,..,6; a1,\ a2,\ b,\ c,\ d)$ take given values (see Eqs. S20 and S27). In Eq. R3, ϕ_3 corresponds to the fraction of the proteome devoted to carrying the carbon flux from Acetyl-CoA (the entry point of Pool b, see Fig. 1B and Appendix 1.2) to α-Ketoglutarate (the entry point of Pool c), with all of these being enzymes within the TCA cycle.

The optimal growth solution is $\phi_3 = \dfrac{\eta_c\cdot\phi_{\max}}{\varphi\cdot\kappa_3/\varepsilon_f + \psi\cdot\kappa_3} > 0$, which demonstrates that in a pure fermentation mode, the optimal growth condition includes the presence of enzymes within the TCA cycle capable of carrying the flux required for biomass generation.

Regarding Eq. S25, J_E represents the energy demand for cell proliferation, expressed as the stoichiometric energy flux in ATP. Although the influx of carbon sources (e.g., glucose) varies significantly between fermentation and respiration modes, J_{BM} and J_E are the biomass and energy fluxes used to build cells, respectively. In bacteria, whether in fermentation or respiration mode, the proportion of maintenance energy used for protein degradation is roughly negligible (see Locasale and Cantley, *BMC Biol* 8, 88 (2010)). Consequently, the energy

demand represented by _J_E scales approximately linearly with the biomass production rate J_{BM} (related experimental data reference: Ebenhöh et al., Life 14, 247 (2024)), regardless of the energy biogenesis mode. Therefore, _r_E can be regarded as roughly constant for bacteria. However, in eukaryotic cells such as yeast and mammalian cells, the proportion of maintenance energy is much more significant (see Locasale and Cantley, BMC Biol 8, 88 (2010)). Therefore, we have explicitly considered the contribution of maintenance energy in these cases and have extended the previous Appendix 6.4 into Appendix 9 in the current version.

> *(ii) The minor weakness of this model is that it assumes a priori that each cell chooses its metabolic strategy based on energy efficiency. This is an interesting assumption but there is no known biochemical pathway that directly executes this mechanism. In evolution, growth rate is more frequently considered for metabolic optimization. In Flux Balanced Analysis, one could have multiple objective functions including biomass synthesis, energy generation, entropy production, etc. Therefore, the author would need to justify this assumption and propose a reasonable biochemical mechanism for cells to sense and regulate their energy efficiency.*

We thank the reviewer for raising this question and apologize for not explaining this point clearly enough in the previous version of our manuscript. Just as the reviewer mentioned, growth rate should be considered for metabolic optimization under the selection pressure of the evolutionary process. In fact, in our model, the sole optimization objective is exactly the cell growth rate. The determination of whether to use fermentation or respiration based on proteome efficiency (i.e., the proteome energy efficiency in our previous version) is not an a priori assumption in our model; rather, it is a natural consequence of growth rate optimization, as we detail below.

For a given nutrient condition with a determined value of κ_A , as we have explained in the aforementioned responses, the constraint on the fluxes is summarized in Eq. 3 and is restated as Eq. R1. Mathematically, we can obtain the solution for the optimal growth strategy by combining Eq. R1 (i.e., Eq. 3) with the optimization on cell growth rate λ, and the solution can be obtained as follows: If the proteome efficiency in fermentation is larger than that in respiration, i.e., $\varepsilon_f > \varepsilon_r$, then from Eq. R1, we obtain $\left(\psi+\varphi/\varepsilon_f\right)\cdot\lambda=\phi_{\max}-J_r^{(\Xi)}\left(1/\varepsilon_r-1/\varepsilon_f\right)$, since the values of ε_r , ε_f, Ψ, φ and $\phi_{\max}$ are all fixed for a given κA , with ε_r , ε_f, Ψ, φ, $\phi_{\max} > 0$. Hence, $\left(\psi+\varphi/\varepsilon_f\right)>0,\ \left(1/\varepsilon_r-1/\varepsilon_f\right)>0$ (since $\varepsilon_f > \varepsilon_r$), and note that $J_r^{(\Xi)}\geq 0$. Therefore $J_r^{(\Xi)}=0$ is the solution for optimal growth, where the growth rate can take the maximum value of $\lambda=\phi_{\max}/\left(\psi+\varphi/\varepsilon_f\right)$. Similarly, for the case where the proteome efficiency in respiration is larger than that in fermentation (i.e $\varepsilon_f > \varepsilon_r$), $J_r^{(\Xi)}=0$ is the solution for optimal growth. With this analysis, we have demonstrated that the choice between fermentation and respiration based on proteome efficiency is a natural consequence of growth rate optimization.

We have now revised the related content in our manuscript to clarify this point.

> *My feeling is that the mathematical structure of this model could be correct, but the single-cell interpretation for the ensemble averaging has issues. Each cell could potentially adopt partial respiration and partial fermentation at the same time and have temporal variability in its metabolic mode as well. With the modification of the*

> *optimization scheme, the author could have a revised model that avoids the caveat mentioned above.*

We thank the reviewer for raising this question. In fact, in the above two responses, we have addressed the issues raised here, clarifying that the binary mode between respiration and fermentation does not hinder cell growth and that the sole optimization objective is the cell growth rate, as the reviewer suggested. Regarding temporal variability, due to factors such as cell cycle stages and the intrinsic noise arising from stochastic processes, temporal variability in the fermentation or respiration mode is indeed likely. However, at any given moment at the single-cell level, a binary choice between fermentation and respiration is what our model predicts for the optimal growth strategy.

> *Discussion and impact for the field*
>
> *Proteome partition models and Flux Balanced Analysis are both commonly used mathematical models that emphasize different parts of cellular physiology. This paper has ingredients for both, and I expect after revision it will bridge our understanding of the whole cell.*

We appreciate the reviewer's very positive comments. We have followed many of the good suggestions raised by the reviewer, and our revised manuscript is much improved as a result.

> ***Reviewer #3 (Public Review):***
>
> *Summary:*
>
> *In the manuscript "Overflow metabolism originates from growth optimization and cell heterogeneity" the author Xin Wang investigates the hypothesis that the transition into overflow metabolism at large growth rates actually results from an inhomogeneous cell population, in which every individual cell either performs respiration or fermentation.*

We thank the reviewer for carefully reading our manuscript and the accurate summary.

> *Weaknesses:*
>
> *The paper has several major flaws. First, and most importantly, it repeatedly and wrongly claims that the origins of overflow metabolism are not known. The paper is written as if it is the first to study overflow metabolism and provide a sound explanation for the experimental observations. This is obviously not true and the author actually cites many papers in which explanations of overflow metabolism are suggested (see e.g. Basan et al. 2015, which even has the title "Overflow metabolism in E. coli results from efficient proteome allocation"). The paper should be rewritten in a more modest and scientific style, not attempting to make claims of novelty that are not supported. In fact, all hypotheses in this paper are old. Also the possiblility that cell heterogeneity explains the observed 'smooth' transition into overflow metabolism has been extensively investigated previously (see de Groot et al. 2023, PNAS, "Effective bet-hedging through growth rate dependent stability") and the random drawing of kcat-values is an established technique (Beg et al., 2007, PNAS, "Intracellular crowding defines the mode and sequence of substrate uptake by Escherichia coli and constrains its metabolic activity"). Thus, in terms of novelty, this paper is very limited. It reinvents the wheel and it is written as if decades of literature debating overflow metabolism did not exist.*

We thank the reviewer for both the critical and constructive comments. Following the reviewer's suggestion, we have revised our manuscript to adopt a more modest style.

However, we respectfully disagree with the criticism regarding the novelty of our study, as detailed below.

First, while many explanations for overflow metabolism have been proposed, we have cited these in both the previous and current versions of our manuscript. We apologize for not emphasizing the distinctions between these previous explanations and our study in the main text of our earlier version, though we did provide details in Appendix 6.3. In fact, most of these explanations (e.g., Basan et al., *Nature* 528, 99-104 (2015); Chen and Nielsen, *PNAS* 116, 17592-17597 (2019); Majewski and Domach, Biotechnol. Bioeng. 35, 732-738 (1990); Niebel et al., Nat. Metab. 1, 125-132 (2019); Shlomi et al., PLoS Comput. Biol. 7, e1002018 (2011); Varma and Palsson, Appl. Environ. Microbiol. 60, 3724-3731 (1994); Vazquez et al., BMC Syst. Biol. 4, 58 (2010); Vazquez and Oltvai, Sci. Rep. 6, 31007 (2016); Zhuang et al., Mol. Syst. Biol. 7, 500 (2011)) heavily rely on the assumption that cells optimize their growth rate for a given rate of carbon influx under each nutrient condition (or certain equivalents) to explain the growth rate dependence of fermentation flux. However, this assumption—that cell growth rate is optimized for a given rate of carbon influx—is questionable, as the given factors in a nutrient condition are the identity and concentration of the carbon source, rather than the carbon influx itself.

Consequently, in our model, we purely optimize cell growth rate without imposing a special constraint on carbon influx. Our assumption that the given factors in a nutrient condition are the identity and concentration of the carbon source aligns with the studies by Molenaar et al. (Molenaar et al., *Mol. Syst. Biol.* 5, 323 (2009)), where they specified an identical assumption on page 5 of their Supplementary Information (SI); Scott et al. (Scott et al., *Science* 330, 1099-1102 (2010)), where the growth rate formula was derived for a culturing condition with a given nutrient quality; and Wang et al. (Wang et al., *Nat. Comm.* 10, 1279 (2019)), our previous study on microbial growth. Among these three studies, only Molenaar et al. addresses overflow metabolism. However, Molenaar et al. did not consider cell heterogeneity, resulting in their model predictions on the growth rate dependence of fermentation flux being a digital response, which is inconsistent with experimental data.

Furthermore, prevalent explanations such as those by Basan et al. (Basan et al., *Nature* 528, 99-104 (2015)) and Chen and Nielsen (Chen and Nielsen, *PNAS* 116, 17592-17597 (2019)) suggest that overflow metabolism originates from the proteome efficiency in fermentation always being higher than in respiration. However, Shen et al. (Shen et al., *Nature Chemical Biology* 20, 1123–1132 (2024)) recently discovered that the proteome efficiency measured at the cell population level in respiration is higher than in fermentation for many yeast and cancer cells, despite the presence of fermentation fluxes through aerobic glycolysis. This finding clearly contradicts the studies by Basan et al. (2015) and Chen and Nielsen (2019).

Nevertheless, our model may resolve this puzzle by incorporating two important features. First, in our model, the proteome efficiency (i.e., the proteome energy efficiency in our previous version) in respiration is larger than that in fermentation when nutrient quality is low (Eqs. S174-S175 in Appendix 9). Second, and crucially, due to the incorporation of cell heterogeneity in our model, there could be a proportion of cells with higher proteome efficiency in fermentation than in respiration, even when the overall proteome efficiency at the cell population level is higher in respiration than in fermentation. As shown in the newly added Fig. 5A-B, our model results can quantitatively illustrate the experimental data from Shen et al., Nature Chemical Biology 20, 1123–1132 (2024).

Finally, regarding the criticism of the novelty of our hypothesis: As specified in our main text, cell heterogeneity has been widely reported experimentally in both microbes (e.g., Ackermann, Nat. Rev. Microbiol. 13, 497-508 (2015); Bagamery et al., Curr. Biol. 30, 4563-4578 (2020); Balaban et al., Science 305, 1622-1625 (2004); Nikolic et al., BMC Microbiol. 13, 1-13 (2013); Solopova et al., PNAS 111, 7427-7432 (2014); Wallden et al., Cell 166, 729-739 (2016)) and tumor cells (e.g., Duraj et al., Cells 10, 202 (2021); Hanahan and Weinberg, Cell 164, 681-

694 (2011); Hensley et al., Cell 164, 681-694 (2016)). However, to the best of our knowledge, cell heterogeneity has not yet been incorporated into theoretical models for explaining overflow metabolism or the Warburg effect. The reviewer mentioned the study by de Groot et al. (de Groot et al., *PNAS* 120, e2211091120 (2023)) as studying overflow metabolism similarly to our work. We have carefully read this paper, including the main text and SI, and found that it is not directly relevant to either overflow metabolism or the Warburg effect. Instead, their model extends the work of Kussell and Leibler (Kussell and Leibler, *Science* 309, 2075-2078 (2005)), focusing on bet-hedging strategies of microbes in changing environments.

Regarding the criticism that random drawing of kcat-values is an established technique (Beg et al., PNAS 104, 12663-12668 (2007)), we need to stress that the distribution noise on kcat-values considered in our model is fundamentally different from that in Beg et al. In Beg et al., their model involved 876 reactions (see Dataset 1 in Beg et al.), of which only 109 had associated biochemical experimental data. Thus, their distribution of kcat-values pertains to different enzymes within the same cell. In contrast, we have the mean of the kcat-values from experimental data for each relevant enzymes, with the distribution of kcat-values representing the same enzyme in different cells.

> *Moreover, the manuscript is not clearly written and is hard to understand. Variables are not properly introduced (the M-pools need to be discussed, fluxes (J_E), "energy coefficients" (eta_E), etc. need to be more explicitly explained. What is "flux balance at each intermediate node"? How is the "proteome efficiency" of a pathway defined? The paper continues to speak of energy production. This should be avoided. Energy is conserved (1st law of thermodynamics) and can never be produced. A scientific paper should strive for scientific correctness, including precise choice of words.*

We thank the reviewer for the constructive comments. Following these, we have provided more explicit information and revised our manuscript to enhance readability. In our initially submitted version, the phrase "energy production" was borrowed from Nelson et al. (Nelson et al., Lehninger principles of biochemistry, 2008) and Basan et al. (Basan et al., Nature 528, 99-104 (2015)), and we chose to follow this terminology. We appreciate the reviewer's suggestion and have now revised the wording to use more appropriate expressions.

> *The statement that the "energy production rate ... is proportional to the growth rate" is, apart from being incorrect - it should be 'ATP consumption rate' or similar (see above), a non-trivial claim. Why should this be the case? Such statements must be supported by references. The observation that the catabolic power indeed appears to increase linearly with growth rate was made, based on chemostat data for E.coli and yeast, in a recent preprint (Ebenhöh et al, 2023, bioRxiv, "Microbial pathway thermodynamics: structural models unveil anabolic and catabolic processes").*

We thank the reviewer for the insightful suggestions. Following these, we have revised our manuscript and cited the suggested reference (i.e., Ebenhöh et al., Life 14, 247 (2024)).

> *All this criticism does not preclude the possibility that cell heterogeneity plays a role in overflow metabolism. However, according to Occam's razor, first the simpler explanations should be explored and refuted before coming up with a more complex solution. Here, it means that the authors first should argue why simpler explanations (e.g. the 'Membrane Real Estate Hypothesis', Szenk et al., 2017, Cell Systems; maximal Gibbs free energy dissipation, Niebel et al., 2019, Nature Metabolism; Saadat et al., 2020, Entropy) are not considered, resp. in what way they are in disagreement with observations, and then provide some evidence of the proposed cell heterogeneity (are there single-cell transcriptomic data supporting the claim?).*

We thank the reviewer for raising these questions and providing valuable insights. Regarding the shortcomings of simpler explanations, as explained above, most proposed explanations (including the references mentioned by the reviewer: Szenk et al., Cell Syst. 5, 95-104 (2017); Niebel et al., Nat. Metab. 1, 125-132 (2019); Saadat et al., Entropy 22, 277 (2020)) rely heavily on the assumption that cells optimize their growth rate for a given rate of carbon influx under each nutrient condition (or its equivalents). However, this assumption is questionable, as the given factors in a nutrient condition are the identities and concentrations of the carbon sources, rather than the carbon influx itself.

Specifically, Szenk et al. is a perspective paper, and the original "membrane real estate hypothesis" was proposed by Zhuang et al. (Zhuang et al., Mol. Syst. Biol. 7, 500 (2011)). Zhuang et al. specified in Section 7 of their SI that their model's explanation of the experimental results shown in Fig. 2C of their manuscript relies on the assumption of restrictions on carbon influx. In Niebel et al. (Niebel et al., Nat. Metab. 1, 125-132 (2019)), the Methods section specifies that the glucose uptake rate was considered a given factor for a growth condition. In Saadat et al. (Saadat et al., Entropy 22, 277 (2020)), Appendix A notes that their model results depend on minimizing carbon influx for a given growth rate, which is equivalent to the assumption mentioned above (see Appendix 6.3 in our manuscript for details).

Regarding the experimental evidence for our proposed cell heterogeneity, Bagamery et al. (Bagamery et al., Curr. Biol. 30, 4563-4578 (2020)) reported non-genetic heterogeneity in two subpopulations of Saccharomyces cerevisiae cells upon the withdrawal of glucose from exponentially growing cells. This strongly indicates the coexistence of fermentative and respiratory modes of heterogeneity in S. cerevisiae cultured in a glucose medium (refer to Fig. 1E in Bagamery et al.). Nikolic et al. (Nikolic et al., BMC Microbiol. 13, 1-13 (2013)) reported a bimodal distribution in the expression of the acs gene (the transporter for acetate) in an E. coli cell population growing on glucose as the sole carbon source within the region of overflow metabolism (see Fig. 5 in Nikolic et al.), indicating the cell heterogeneity we propose. For cancer cells, Duraj et al. (Duraj et al., Cells 10, 202 (2021)) reported a high level of intra-tumor heterogeneity in glioblastoma using optical microscopy images, where 48%~75% of the cells use fermentation and the remainder use respiration (see Fig. 1C in Duraj et al.), which aligns with the cell heterogeneity picture of aerobic glycolysis predicted by our model.

We have now added related content to the discussion section to strengthen our manuscript.

> ***Reviewer #1 (Recommendations For The Authors):***
>
> *Some minor corrections:*
>
> *(1) Adjusted the reference: (García-Contreras et al., 2012)*
>
> *(2) Corrected line 255: Removed the duplicate "the genes"*

We thank the reviewer for the suggestions and have implemented each of them to revise our manuscript. The reference in the form of García-Contreras et al., 2012, although somewhat unusual, is actually correct, so we have kept it unchanged.

> *General comment to the author:*
>
> *Considering that this work exists at the interface between Physics and Biology, where a significant portion of the audience may not be familiar with the mathematical manipulations performed, it would enhance the paper's readability to provide more explicit indications in the text. For example, in line 91, explicitly define phi_A as phi_R; or in line 115, explain the K_i parameter in the text for better readability.*

We thank the reviewer for the suggestion. Following this, we have now provided more explicit information for the definition of mathematical symbols to enhance readability.

> ***Reviewer #2 (Recommendations For The Authors):***
>
> *The current form of this manuscript is difficult to read for general readers. In addition, the model description in the Appendix can be improved for biophysics readers to keep track of the variables. Here are my suggestions:*
>
> *a) In the main text, the author should give the definition of "proteome energy efficiency" explicitly both in English and mathematical formula - since this is the central concept of the paper. The biological interpretation of formula (4) should also be stated.*

We thank the reviewer for the suggestion. Following this, we have now added definitions and biological interpretations to fix these issues.

> *b) I feel the basic model of the reaction network in the Appendix could be stated in a more concise way, by emphasizing whether a variable is extensive (exponential growing) or intensive (scale-invariant under exponential growth).*
>
> *From my understanding, this work assumes balanced exponential growth and hence there is a balanced biomass vector Y* (a constant unit vector with all components sum to 1) for each cell. The steady-state fluxes {J} are extensive and all have growth rate λ. The proteome partition and relative metabolite fractions are ratios of different components of Y* and hence are intensive.*
>
> *The normalized fluxes {J^(n)} (with respect to biomass) are a function of Y* and are all kept as constant ratios with each other. They are also intensive.*
>
> *The biomass and energy production are linear combinations of {J} and hence are extensive and follow exponential growth. The biomass and energy efficiency are ratios between flux and proteome biomass, and hence are intensive.*

We thank the reviewer for the insightful suggestion. Following this, we have now added the intensive and extensive information for all relevant variables in the newly added Appendix-table 3.

> *c) In the Appendix, the author should have a table or list of important variables, with their definition, units, and physiological values under respiration and fermentation.*

We thank the reviewer for the very useful suggestion. Following this, we have now added Appendix-table 3 (pages 54-57 in the appendices) to illustrate the symbols used throughout our manuscript, as well as the model variables and parameter settings.

> *d) Regarding the single-cell variability, the author ignored recent experimental measurements on single-cell metabolism. This includes variability on ATP, NAD(P)H in E. coli, which will be useful background for the readers, see below.*
>
> *https://pubmed.ncbi.nlm.nih.gov/25283467/*
>
> *https://pubmed.ncbi.nlm.nih.gov/29391569/*

We thank the reviewer for the very useful suggestion. We have now cited these relevant studies in our manuscript.

e) The choice between 100% respiration and 100% fermentation is based on the optimization of proteome energy efficiency, while the intermediate strategies are not favored in this model. This is similar to a concept in control theory called the bang-bang principle. This can be added to the Discussion.

We thank the reviewer for this suggestion. We have reviewed the concept and articles on the bang-bang principle. While the bang-bang principle is indeed relevant to binary choices, it is somewhat distant from the topic of metabolic strategies related to optimal growth. The elementary flux mode (see Müller et al., J. Theor. Biol. 347, 182190 (2014); Wortel et al., FEBS J. 281, 1547-1555 (2014)) is more pertinent to this topic, as it may lead to diauxic microbial growth (another binary metabolic strategy) in microbes grown on a mixture of two carbon sources from Group A (see Wang et al., Nat. Comm. 10, 1279 (2019)). Therefore, we have cited and mentioned only the elementary flux mode (Müller et al., J. Theor. Biol. 347, 182-190 (2014); Wortel et al., FEBS J. 281, 1547-1555 (2014)) in the introduction and discussion sections of our manuscript.

https://doi.org/10.7554/eLife.94586.2.sa0